

Title	Pseudogap and precursor superconductivity study of $\text{YBa}_2(\text{Cu}_{1-x}\text{Zn}_x)\text{F}_{3-y}$: c-axis optical study from underdoped to overdoped region
Author(s)	Uykur, Ece
Citation	大阪大学, 2013, 博士論文
Version Type	VoR
URL	https://doi.org/10.18910/34063
rights	
Note	

Osaka University Knowledge Archive : OUKA

<https://ir.library.osaka-u.ac.jp/>

Osaka University

**Pseudogap and precursor superconductivity
study of $\text{YBa}_2(\text{Cu}_{1-x}\text{Zn}_x)_3\text{O}_y$: *c*-axis optical
study from underdoped to overdoped region**



Ece UYKUR

Department of Physics, Graduate School of Science

Osaka University

A thesis submitted for the degree of

PhD

December 12, 2013

Acknowledgements

I would like to thank...

... Prof. Setsuko Tajima, for her guidance and support during this work. Her advices and discussions are valuable for me. I am also grateful to her for answering all my questions and for careful reading of this thesis.

... Dr. Shigeki Miyasaka, for teaching me how to use the FTIR spectrometer and for his help in resolving problems related with the experimental setup during measurements.

... Dr. Takahiko Masui, for growing crystals that were measured in the experiments for this thesis. The high quality crystals are very much appreciated.

... Dr. Kiyohisa Tanaka, for his discussions, suggestions, and guidance during the measurements and data analysis.

... all members of the Tajima group, for their help and patience related or unrelated with the laboratory work.

... Tajima group secretary Yoshiko Ishimoto, for her help with the endless paperwork.

... Mustafa Çağatay Tulun, for his help to refine the programs used for data analysis.

... Pham Tan Thi, Kwing To Lai, Nguyen Trung Hieu, Nguyen Minh Hien, for the fun times.

... to my parent for their encouragement and continuous supports.

Ece UYKUR

December, 2013

Osaka, Japan

Contents

List of Figures	v
List of Tables	ix
1 Introduction	1
2 High Temperature Cuprate Superconductors	5
2.1 General Properties of Cuprates	5
2.1.1 Crystal structure	5
2.1.2 Phase diagram	6
2.1.3 Electronic structure of cuprates	8
2.2 Pseudogap and Precursor Superconducting State	10
2.2.1 Pseudogap state	10
2.2.2 Precursor Superconducting State	16
2.3 General Optical Properties of Cuprates	20
2.3.1 In-plane and c -axis optical properties	20
2.3.2 Pseudogap and superconducting gap behavior in c -axis optical spectrum	23
2.3.3 Superfluid density in c -axis optical spectra	26
2.3.4 Transverse Josephson plasma (TJP) resonance mode	28
2.3.5 Impurity effect on c -axis optical properties	30
2.4 Aim of This Study	33
3 Experimental Procedure	35
3.1 Samples	35
3.2 Principle of the Fourier Transform Infrared (FTIR) Spectroscopy	39

CONTENTS

3.3	Experimental Details	42
3.3.1	Fourier Transform Infrared (FTIR) system	42
3.3.2	Low temperature measurements	44
3.3.3	Reflectivity measurements	46
3.4	Optical relations	46
3.5	Fitting of the Reflectivity Spectra	49
4	Results and discussion	53
4.1	$E//c$ -axis Optical Measurements	53
4.1.1	Doping dependent optical spectra of $\text{YBa}_2\text{Cu}_3\text{O}_y$	53
4.1.2	Zn-substitution effects on optical response	59
4.2	Discussion on Pseudogap	60
4.2.1	Pseudogap in the underdoped region	60
4.2.2	Pseudogap in the overdoped region	66
4.2.3	Interpretation of the pseudogap	69
4.3	Discussion on Precursor Superconductivity	71
4.3.1	Precursor superconducting state in the optical conductivity	71
4.3.2	Comparison of our phase diagram with the results of other probes	83
4.3.3	Interpretation of the precursor superconducting state	85
4.4	Remarks on Kinetic Energy Driven Superconductivity	90
5	Conclusion	95
5.1	Pseudogap in the Superconducting State	95
5.2	Pseudogap in the Overdoped Region	96
5.3	Precursor Superconducting State	97
5.4	Kinetic Energy Driven Superconductivity	98
5.5	Future Work	98
	References	101
	List of Publications	111
	List of Conferences	113

List of Figures

2.1	Crystal Structure of cuprates	6
2.2	Phase diagram of the cuprate superconductors	7
2.3	Electronic structure of the cuprate superconductors	8
2.4	Pseudogap in NMR Knight shift and spin-lattice relaxation rate	11
2.5	Temperature dependence of ARPES intensity that demonstrates the pseudogap behavior	12
2.6	Pseudogap and superconducting gap in the symmetrized ARPES spectra	13
2.7	Momentum dependence of the superconducting gap function	13
2.8	Inplane resistivity curvature mapping	14
2.9	Out-of-plane resistivity and theory of pseudogap	15
2.10	T_c and T^* obtained from out-of-plane resistivity	16
2.11	Nernst signal of cuprates	17
2.12	Enhanced Nernst signal region for $\text{La}_{2-x}\text{Sr}_x\text{CuO}_4$	17
2.13	Indication of the precursor superconducting state in ARPES measurement	18
2.14	Doping dependence of the precursor state obtained by ARPES measurement	18
2.15	Superfluid density along in-plane of the cuprates revealed by THz-time domain spectroscopy	20
2.16	Precursor superconductivity state revealed by THz-time domain measurements	21
2.17	Doping dependent resistivity - inplane and c -axis	22
2.18	Inplane vs. c -axis optical conductivity	23
2.19	Comparison of the c -axis optical conductivity for several cuprate family	24
2.20	Pseudogap behavior in the c -axis optical conductivity	25

LIST OF FIGURES

2.21 Pseudogap and superconducting gap in the c -axis optical conductivity - spectral weight calculation	26
2.22 Doping dependent Josephson plasma edge	27
2.23 Penetration depth vs. dc conductivity curve of cuprates	28
2.24 Schematic of intra-bilayer and inter-bilayer formation in the crystal structure	29
2.25 Transverse Josephson plasma resonance in the c -axis optical spectrum	30
2.26 Impurity effect on Josephson plasma frequency	31
2.27 Impurity effect on Transverse Josephson plasma mode	32
2.28 Impurity effect on c -axis properties in the overdoped region	32
3.1 Zn- and doping dependence of dc magnetic susceptibility	36
3.2 Doping level vs T_c curve of $\text{YBa}_2\text{Cu}_3\text{O}_y$	39
3.3 Zn content vs. maximum T_c curve	39
3.4 Schematic of a Michelson interferometer	40
3.5 Schematic of an interferometer of monochromatic light	40
3.6 Schematic of an interferogram of polychromatic light	41
3.7 Schematic view of Bruker 80V FTIR system	42
3.8 Schematic view of sample space	43
3.9 Power spectra of the different energy regions used in measurements	44
3.10 Schematic view of the cryostat	45
3.11 Determination of the errors in the reflectivity measurements	47
3.12 Determination of the error in optical conductivity	48
3.13 Low energy fitting of the reflectivity used for extrapolations	50
3.14 Comparison of the dc resistivity data with the optical conductivity extrapolations	51
3.15 Zn-substitution effect on in-plane and c -axis resistivity	52
3.16 c -axis resistivity obtained from the extrapolation of the optical conductivity	52
4.1 Doping dependent room temperature reflectivity of $\text{YBa}_2\text{Cu}_3\text{O}_y$	54
4.2 Doping dependent reflectivity of $\text{YBa}_2\text{Cu}_3\text{O}_y$ in the superconducting state	55
4.3 Doping dependent transverse Josephson plasma mode	56
4.4 Doping dependence of the Josephson plasma frequency of $\text{YBa}_2\text{Cu}_3\text{O}_y$	57

LIST OF FIGURES

4.5	Doping dependence of the oxygen bending mode in $\text{YBa}_2\text{Cu}_3\text{O}_y$	58
4.6	Zn-concentration dependence of the room temperature optical spectra	59
4.7	Zn-concentration dependence of the optical spectra in the superconducting region	60
4.8	Pseudogap behavior in the optical conductivity	62
4.9	Energy region dependence of the spectral weight	63
4.10	Doping dependence of the low energy SW	64
4.11	Pseudogap temperatures obtained from the low energy SW	64
4.12	Zn-doping dependence of the low and high energy SW	65
4.13	Scenarios of the pseudogap in the overdoped region	66
4.14	Zn-substitution effect on optical conductivity in the overdoped region	67
4.15	Low- ω optical conductivity: Demonstration of the pseudogap opening	68
4.16	Doping dependent $\Delta\sigma_1(T-T^*)$ spectra	69
4.17	Determination of the pseudogap energy	70
4.18	Zn-substitution effect on the pseudogap energy	71
4.19	Determination of the superfluid density from real optical conductivity	72
4.20	Determination of the superfluid density from imaginary optical conductivity	74
4.21	Doping and Zn-dependence of the superfluid density obtained from $\sigma_1(\omega)$ and $\sigma_2(\omega)$	76
4.22	Zn-doping effect on the observed temperature scales as a function of doping	77
4.23	Phase diagram of the Zn-substituted samples	78
4.24	Doping and Zn-doping dependence of the oxygen bending mode	80
4.25	Comparison of the T_p values obtained by several methods	80
4.26	Magnetic susceptibility of the heavily underdoped sample	81
4.27	Optical spectra of the heavily underdoped sample	82
4.28	Precursor superconductivity for the heavily underdoped sample	82
4.29	Temperature scale in the underdoped region	82
4.30	Obtained temperature scales of $\text{YBa}_2\text{Cu}_3\text{O}_y$ that are compared with other probes	84
4.31	Schematic of the inhomogeneous superconducting state scenario	86
4.32	Indication of the precursor superconducting state in STM	88
4.33	Indication of the precursor superconducting state in inplane resistivity	89

LIST OF FIGURES

4.34 Doping and Zn-doping dependence of the observed discrepancy of super- fluid density determined by two different methods	91
4.35 Cut-off frequency dependence of $\Delta N/\rho_s$	93

List of Tables

3.1	Zn-content (x), doping level (p), T_c , transition width ΔT_c and annealing condition	38
3.2	Light sources, detectors, and beamsplitters used in measurements	44
3.3	Windows and polarizers used in measurements	45

LIST OF TABLES

1

Introduction

The phenomenon called superconductivity was observed more than a century ago by H. Kamerlingh Onnes when he cooled down the mercury and observed the abrupt decrease of its resistivity [1]. Over the years many elemental superconductors had been reported, but the class that we refer as high temperature cuprate superconductors had been discovered by Bednorz and Müller after 75 years later from the first observation [2]. Later on, another class of high temperature superconductors had been discovered in iron-based compounds [3], namely the iron-pnictides. Today we have tremendous amount of experimental data for both cuprates and iron-pnictides, however, not so deep understanding how the superconductivity beyond the BCS theory [4] occurs in these materials. How we can explain the high temperature superconductivity and the unusual behaviors in these materials is still an open question. The main topic of this thesis is the charge dynamics of the cuprate high temperature superconductors in the normal and the superconducting state revealed by the optical spectroscopy.

Superconductivity in cuprates arises in the two-dimensional CuO_2 planes as a common behavior to all cuprate families. Parent compounds in these materials are antiferromagnetic Mott insulators. With hole doping to the system, the antiferromagnetic order is quickly suppressed and the superconducting state can be observed as a dome that gives a maximum around 16% hole doping. This doping level is referred as the optimally doped region. The lower doping region is called underdoped region, while the higher doping region is ascribed as the overdoped region. The overdoped region (especially highly overdoped region) is close to the Fermi-Liquid state, however, the underdoped region of the phase diagram is rather unconventional. The general behav-

1. INTRODUCTION

ior of the cuprate superconductors and the electronic phase diagram is discussed in Chapter 2.

Pseudogap region dominating the underdoped region of the phase diagram is one of the biggest questions in the cuprate superconductors' research. Despite the intensive study, the origin of the pseudogap, as well as its relation with the superconductivity is still under debate. There are theories that explain the pseudogap as the precursor of the superconductivity, while the others explain this state as a different competing order to the superconductivity. Especially increasing experimental evidence towards another defined state as the precursor superconductivity supports the conclusions about the pseudogap as a competing order, as well. In Chapter 2, the experimental and theoretical discussions about the pseudogap and the precursor state are summarized in a manner that leads to our motivation, as well. Chapter 2 will also describe the general c -axis optical properties of cuprates as a background of our study.

Optical spectroscopy is one of the powerful tools to investigate the charge dynamics in these materials. It is very sensitive to the charge gaps, therefore, it is a commonly used technique. We can obtain the energy dependent carrier lifetime and effective mass. It is a bulk sensitive technique in contrast to the other two very important techniques in HTSC research, angle resolved photoemission spectroscopy (ARPES), and scanning tunneling microscopy spectroscopy (STM). Optical conductivity in a general sense is not a momentum dependent measurement like ARPES. However, in certain cases we can observe a momentum dependent behavior, as well, even though it is a weighted average over the Fermi surface. In this thesis Fourier transform infrared (FTIR) spectroscopy had been used in experiments. The fundamentals of this technique, as well as the basic data analysis are given in Chapter 3. Moreover, we chose to perform c -axis optical study as this thesis topic.

Temperature dependent reflectivity measurements on one of the well known cuprate system $\text{YBa}_2\text{Cu}_3\text{O}_y$ had been performed as the topic of this thesis. The pseudogap behavior had been investigated where the measurement range expands from underdoped region to the overdoped region that includes several doping levels. A systematic study of Zn-substitution had also been performed as a controlled impurity, where the superconductivity is suppressed, as a result, the pseudogap and the superconductivity related features had been observed more clearly. Briefly, in this thesis, it has been shown that the pseudogap state that dominates the underdoped region of the phase diagram is not

the precursor of the superconductivity, moreover, it coexists with the superconducting state even below T_c . Furthermore, the pseudogap reaches to the quantum critical point in the overdoped region of the phase diagram. Although the pseudogap is not the precursor state, it is possible to find a precursor state of the superconductivity that is placed above the superconducting dome with a rather unusual behavior. This state is not only the existence of the Cooper pairs without long-range phase coherence, but also a state where the actual superconducting regions can be embedded into the normal regions as an inhomogeneous superconducting state. The details of the experiments, data, and results are shown in Chapter 4. And finally the conclusions are given in Chapter 5.

1. INTRODUCTION

2

High Temperature Cuprate Superconductors

2.1 General Properties of Cuprates

When Bednorz and Müller discovered the superconductivity in a compound La-Ba-Cu-O in 1986, it was considered as a breakthrough in the research of the superconductivity. This leads to the discovery of the other cuprate superconductors, and immediately the transition temperature of the synthesized materials reached to the liquid nitrogen temperature. Today the maximum transition temperature of the cuprate superconductors changes from 35 K for $\text{La}_{2-x}\text{Sr}_x\text{CuO}_4$ to 138 K for $\text{Hg}_{1-x}\text{Tl}_x\text{Ba}_2\text{Ca}_2\text{Cu}_3\text{O}_y$ (the highest record under normal pressure, which extends to ~ 160 K at high pressure) [5].

2.1.1 Crystal structure

As a common property, all cuprate superconductors have a layered perovskite structure that consists of alternating conducting CuO_2 layers and insulating blocking layers that provide charge carriers to the CuO_2 layers. Even though this is the general scheme, the numbers of the CuO_2 layers are different in different cuprate families. In Fig. 2.1, as an example to 1-, 2-, and 3- layer cuprate families had been shown.

In this thesis, we worked with double layer $\text{YBa}_2\text{Cu}_3\text{O}_y$ system, because the additional structures, namely the CuO-chains in this system give some advantage in our measurements by increasing the conductivity along the c -axis.

2. HIGH TEMPERATURE CUPRATE SUPERCONDUCTORS

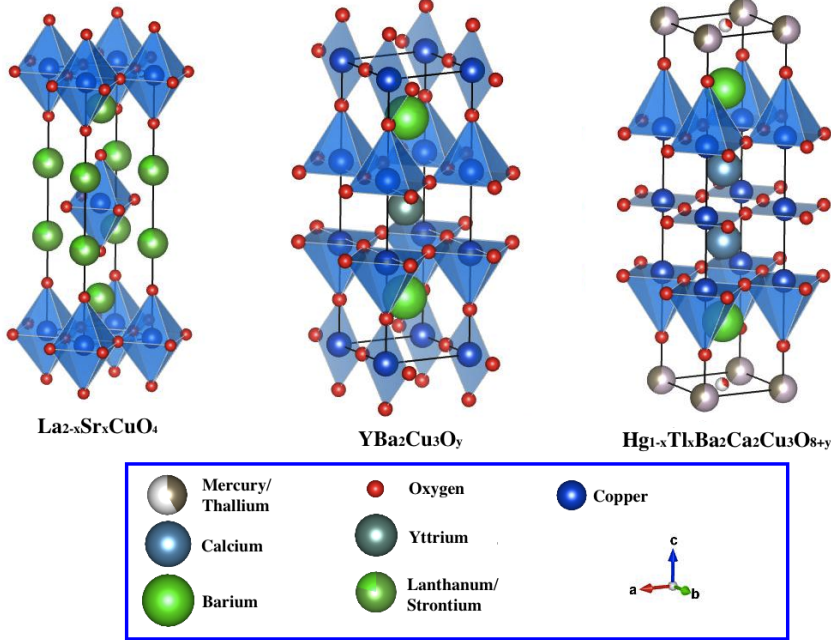


Figure 2.1: Crystal Structure of cuprates - Crystal Structure of 1- ($\text{La}_{2-x}\text{Sr}_x\text{CuO}_4$ [6]), 2- ($\text{YBa}_2\text{Cu}_3\text{O}_y$ [7]), and 3- ($\text{Hg}_{1-x}\text{Tl}_x\text{Ba}_2\text{Ca}_2\text{Cu}_3\text{O}_y$ [5]) layer cuprates.

$\text{YBa}_2\text{Cu}_3\text{O}_y$ is a system, where the charge doping can be adjusted with oxygen annealing. And this material belongs to the hole doped case, where we will show the electronic phase diagram in the next section. In cuprates, it is also possible to create hole doping in the system with substituting positive ions by ions of smaller valence, such as Sr^{2+} to La^{3+} sites in $\text{La}_{2-x}\text{Sr}_x\text{CuO}_4$. Zn-substitution that been used in this study, on the other hand does not alter the doping level.

2.1.2 Phase diagram

Phase diagram of the cuprate superconductors can be divided into two as the electron doped and the hole doped side. In Fig. 2.2, phase diagram of the hole doped and electron doped cuprate superconductors had been shown. The electron doped case is not the topic of this thesis; therefore, the hole doped side of the phase diagram will be explained in more detail.

The so-called parent compound in cuprates (for instance non-doped $\text{YBa}_2\text{Cu}_3\text{O}_6$ for $\text{YBa}_2\text{Cu}_3\text{O}_y$, hole concentration is zero) is an antiferromagnetic Mott insulator. The

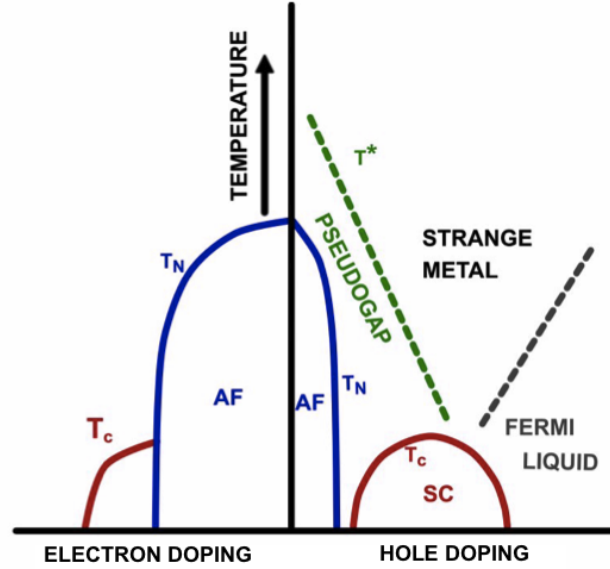


Figure 2.2: Phase diagram of the cuprate superconductors - Phase diagram of the cuprate superconductors.

Néel temperature is around 350 K. With hole doping to the system, the antiferromagnetic insulator state is rapidly suppressed and around 5% doping superconductivity starts to be observed.

The superconducting dome is another common behavior among the cuprate families, even though the transition temperature differs greatly from around 35 K to 138 K. The maximum T_c will be observed around 16% doping level that is referred as the optimally doped region.

The doping region between 5% and 16% is called the underdoped region. The normal state of this region is the strange metal region, which is characterized by the pseudogap. Although this region is metallic in the normal state, it cannot be defined with as the conventional Fermi liquid region, hence it is referred as the strange metal region.

Pseudogap region, where a partial gap in the density of states at the Fermi surface had been observed by several experimental probes, is one of the issues in the phase diagram. The pseudogap state strongly dominates the underdoped region with a behavior that is mostly agreed among different probes. On the other hand, some debates still continue about the behavior in the overdoped region. Pseudogap state is one of the

2. HIGH TEMPERATURE CUPRATE SUPERCONDUCTORS

main topics of this thesis in Chapter 4.

Beyond the optimum hole doping region, system is referred as overdoped. In the overdoped region system is getting closer to the Fermi-liquid state. In the heavily overdoped regime, it can be defined with the conventional Fermi-liquid theory.

2.1.3 Electronic structure of cuprates

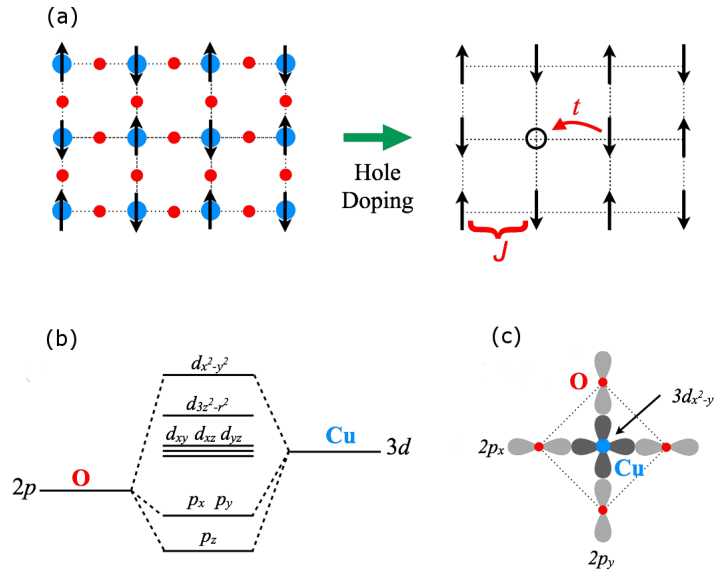


Figure 2.3: Electronic structure of the cuprate superconductors - (a) Schematic picture of the CuO₂ plane in the parent compound and in the case of hole doping. (b) Schematic diagram for the energies of Cu 3d and O 2p orbitals. (c) Hybridization of Cu 3d and O 2p orbitals.

It is well known that the superconductivity arises in the CuO₂ planes in the cuprate superconductors. Cu atoms are surrounded by six oxygen atoms creating an octahedral form (Fig. 2.3 (a), here the apical oxygens has not been shown). In this case the Cu band is half filled with a single hole that has spin 1/2. The Jahn-Teller distortion of this octahedral form (due to the apical oxygens) leads a splitting in the Cu energy states to e_g ($d_{x^2-y^2}$ and $d_{3z^2-r^2}$) (Fig. 2.3 (b)), where the highest partially occupied d states is the $d_{x^2-y^2}$. Oxygen p states also split and a hybridization of these states will

be observed (Fig. 2.3 (c)). Thus the electronic state of the cuprates can be described by the three-band model including the Cu $d_{x^2-y^2}$ and O p_x and p_y [8, 9].

Due to the partially gapped d -band, band structure calculations predict that the system is a metal, however, the parent compound of the cuprates shows insulating behavior (Mott insulator). It is insulating because the Coulomb repulsion U (a few eV between upper and the lower Hubbard band) on the Cu-sites are larger than the bandwidth. More precisely these compounds can be classified as the charge transfer insulators, because the lowest energy excitations, charge transfer excitations, are smaller than the on-site Coulomb repulsion, U .

It is believed that many aspects of the physics of the cuprates can be explained with a single band Hubbard model [10], which contains a kinetic energy term, t , and a Hubbard term, U . Here t is proportional to the nearest neighbor hopping amplitude and U defines the electron correlations. In the strong coupling limit at half filling (parent compound), where $U \gg t$, electrons tend to localize, hence we observe the insulating behavior. Since we have a localized system, as one unpaired electron on each unit cell with the spin $+1/2$ or $-1/2$, the configurations of the neighboring electrons determine the stability of the system. The antiparallel order of the spins is the chosen state, since this state allows the electrons to penetrate other sites with exchange process. In the parallel ordering, the exchange mechanism is prohibited due to the Pauli exclusion principle and there is no gained energy (J). Under this circumstances the hamiltonian of the system can be defined with the t - J model and given as:

$$\mathcal{H}_{Hubbard} = -t \sum_{i,j,\sigma} c_{i\sigma}^\dagger c_{j\sigma} + J \sum_{i,j} (\vec{S}_i \cdot \vec{S}_j - \frac{n_i n_j}{4}) \quad (2.1)$$

Here, J is the exchange energy, which also includes the Coulomb term. \vec{S}_i and \vec{S}_j are the spins in the site i and site j . When we start to dope holes to the Mott insulator, the situation becomes rather complicated. In the low doping level (non-superconducting state), when the kinetic term becomes dominant in one site, the electrons become itinerant. However, if the electron transferred to a vacant site has the spin with the same order with the neighboring site, the exchange energy will be destabilized, while the electronic energy will be stabilized. The condition between J and t will determine the result.

2. HIGH TEMPERATURE CUPRATE SUPERCONDUCTORS

With further hole doping (the region that we start to see the superconductivity) the antiferromagnetic order loses its stability and system starts to become metallic and superconductive. The Hubbard gap starts to close and with further doping it closes completely and a well-defined Fermi surface will be formed. In this case, the system shows Fermi-liquid behavior. However, there is no consensus about the electronic structure in the intermediate region, between the two extreme points. There are some theories, which try to explain this intermediate region with doped Mott insulator scenario, while others suggest that the difficulties seen in this region can be solved with modifications on Fermi-liquid theory (modified Fermi-liquid approach).

Although the BCS theory successfully explains the microscopic features for the conventional superconductors, it is quite insufficient to explain those of the high-temperature superconductors. Nevertheless, there is not a generally established theory for these materials. It seems that not only the superconducting state but also other regions of the phase diagram show interesting and unusual features. Therefore, the microscopic theories proposed for HTSCs are expected to explain these regions, too. There have been many theories proposed over the years. Some of these theories can be given as: Resonating Valance Bond (RVB) theory [11, 12], Spin fluctuations [13, 14] and Inhomogeneity induced pairing [15]. However, none of these theories can explain the phase diagram of the cuprate high temperature superconductors.

2.2 Pseudogap and Precursor Superconducting State

2.2.1 Pseudogap state

Pseudogap state has been observed by many experimental probes as the partial gap in the Fermi surface. In this section, a summary will be given on the techniques that presented the pseudogap behavior in the high temperature cuprate superconductors. Despite the variety of the probes and experiments, the origin of the pseudogap and its relation with the superconducting region is still controversial. Although there are a variety of theories, it seems they can be summarized in two main ideas: The one that explains the pseudogap as a precursor of superconductivity, and the other that presents this state as the competing order to the superconductivity.

The first technique that observed the existence of the pseudoap was the nuclear magnetic resonance (NMR) probe. The spin channel can be observed with this probe.

2.2 Pseudogap and Precursor Superconducting State

Therefore, this had been used as the evidence that the pseudogap is a spin density wave. On the other hand, the pseudogap had been observed in a charge channel, as well. The optical conductivity, which is the topic of this thesis, is one of these probes.

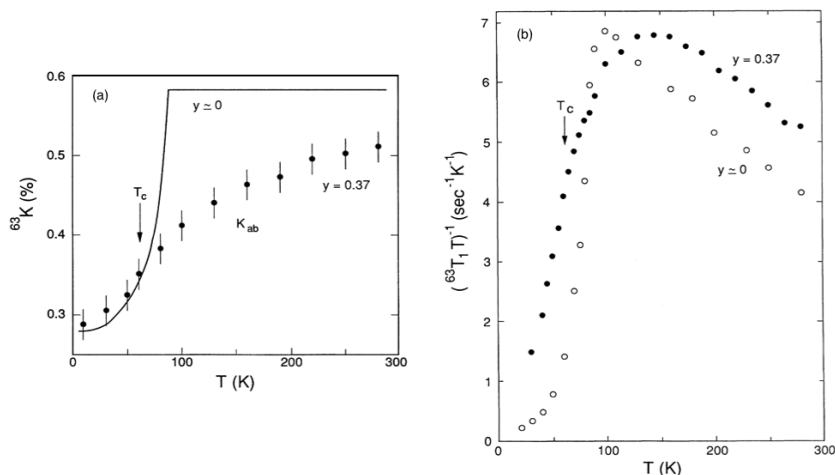


Figure 2.4: Pseudogap in NMR Knight shift and spin-lattice relaxation rate - (a) Cu Knight shift and (b) Cu relaxation rate for YBa₂Cu₃O_{7-y} with $y = 0$ (optimally doped) and $y = 0.37$ (underdoped) [16].

Pseudogap had been observed in Knight shift, K_s and spin-lattice relaxation rate, $1/T_1$. Both the Knight shift and the relaxation rate show a decrease below T_c indicating the superconducting transition. Some examples are shown in Fig. 2.4 for two different doping levels, namely for the optimally doped and for the underdoped region. For the optimally doped sample the decrease of the Knight shift and relaxation rate below T_c is observed. For the underdoped sample, on the other hand, the behavior is dramatically different. The decrease of K_s and $1/T_1$ start well above T_c , that is even decrease to its 20% above T_c . This had been attributed to the pseudogap behavior. The data in Fig. 2.4 belongs to the Cu ion. However, it has been shown that a similar behavior was also observed for other ion sites such as ⁸⁹Y, as well [17].

The ARPES measurements pointed out that the pseudogap dominates the antinodal region of the Fermi surface. Therefore, to use a momentum dependent technique is an advantage. The pseudogap had been observed for many cuprate families with ARPES. Bi-systems among them are the ones that were extensively studied. Due to the surface

2. HIGH TEMPERATURE CUPRATE SUPERCONDUCTORS

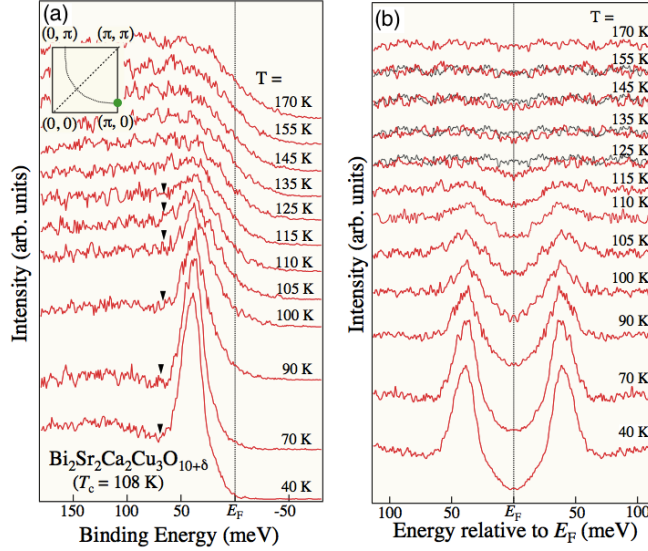


Figure 2.5: Temperature dependence of ARPES intensity that demonstrates the pseudogap behavior - (a) Temperature dependence of ARPES spectra (b) Symmetrized ARPES spectra [18].

conditions these systems are the most suitable ones. In Fig. 2.5, the temperature dependent ARPES spectra are shown for the $\text{Bi}_2\text{Sr}_2\text{Ca}_2\text{Cu}_3\text{O}_{10+\delta}$ sample in the antinodal region. As can be seen more easily from the symmetrized spectra (Fig. 2.5(b)), the gap closes at temperatures above T_c .

Some other ARPES results were also discussed in terms of the pseudogap behavior below the superconducting transition temperature. The sharp peak in the spectra had been associated with the superconducting gap. Moreover, the broad feature at the higher energies was attributed to the pseudogap. Two different energy scales support the scenario of two different gaps. Features of the superconducting gap and the pseudogap have been given in Fig. 2.6.

Moreover, some recent experiments showed that the gap function of the underdoped samples deviates from the d -wave form near the antinodal region, as is shown in Fig. 2.7. This can be explained if we assume that the pseudogap effect on the superconducting gap is getting stronger with underdoping (where the pseudogap is strong). Therefore, the observed gap function in the antinodal region is not only the superconducting gap, but also the effects of the pseudogap. This explanation is based on the two gap scenario.

Pseudogap behavior was also observed in the transport measurements. One of the

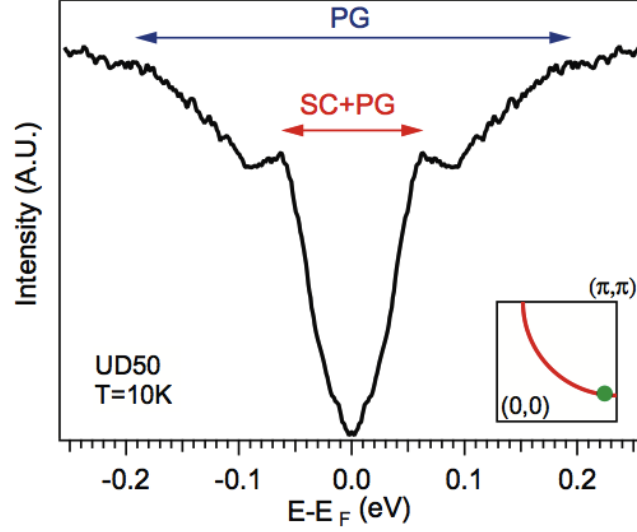


Figure 2.6: Pseudogap and superconducting gap in the symmetrized ARPES spectra - A low-energy peak associated with superconductivity (SC) and a broader feature at higher energy associated with the pseudogap (PG) [19]. This data belongs to underdoped sample.

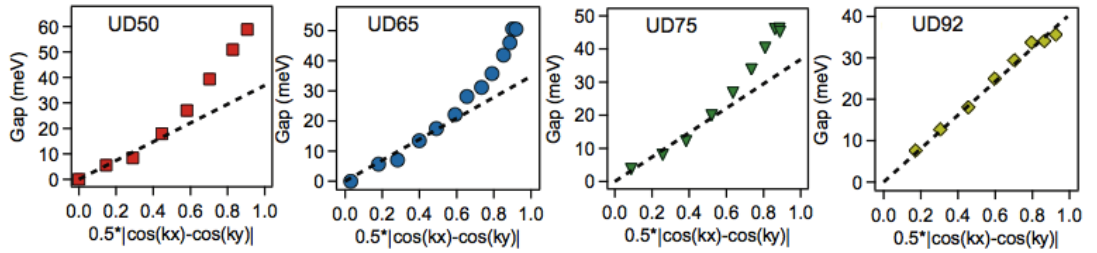


Figure 2.7: Momentum dependence of the superconducting gap function - Doping dependence of the momentum dependent SC gap function of $\text{Bi}_2\text{Sr}_2\text{CaCu}_2\text{O}_8$ [19]. Dashed lines are the simple d -wave function.

2. HIGH TEMPERATURE CUPRATE SUPERCONDUCTORS

most extensive studies on the pseudogap behavior in the in-plane resistivity had been performed by Ando *et al.* [20]. They measured the in-plane resistivity of series of cuprate families over the very wide doping range of the phase diagram. In Fig. 2.8 the data of $\text{YBa}_2\text{Cu}_3\text{O}_y$ are presented. By using these resistivity data, Ando *et al.* map the in-plane resistivity curve. Furthermore, they define the pseudogap behavior as the inflection point of the resistivity curve (where the second derivative of T is zero). As a result, the pseudogap temperature derived with this method becomes the diagonal white line on the phase diagram (Fig. 2.8(c)).

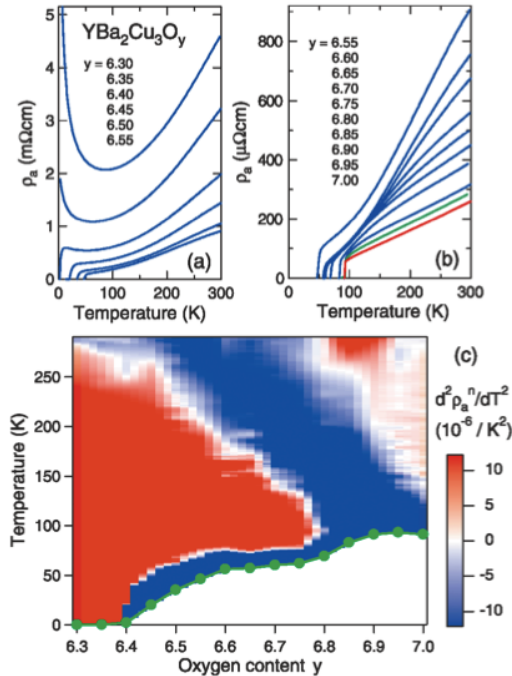


Figure 2.8: Inplane resistivity curvature mapping - Doping dependent in-plane resistivity curves (a, b) and the resistivity curve mapping (c) [20].

Another way to define the pseudogap behavior has been recently proposed by Naqib *et al.* [21] on out-of-plane resistivity. In Fig. 2.9, the out-of-plane resistivity data for $\text{YBa}_2\text{Cu}_3\text{O}_y$ are shown. Black curves are the proposed theory based on the t - J model calculations with some modifications. The fitting function is also on this figure. Here the first term defines the linear temperature-dependence, whereas, in the second term, β is a variable that depends on the c -axis tunneling matrix element and electronic density of states at high energies outside the pseudogap region. \mathcal{E}_g defines the pseudogap energy.

2.2 Pseudogap and Precursor Superconducting State

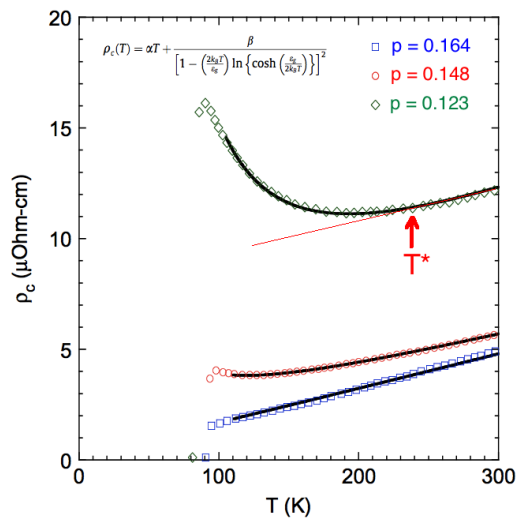


Figure 2.9: Out-of-plane resistivity and theory of pseudogap - Doping dependent out-of-plane resistivity curves [21]. Black fittings are obtained by theory. Red curve on $p = 0.123$ and the arrow with T^* is plotted by additionally to demonstrate the earlier interpretation of the pseudogap in the out-of-plane resistivity, although this method is also consistent with the temperature obtained by this theory.

If we know the pseudogap energy, then we can convert it to temperature as $T = \mathcal{E}_g/k_b$. This conversion has been done for both $\text{YBa}_2\text{Cu}_3\text{O}_y$ and Ca-substituted $\text{YBa}_2\text{Cu}_3\text{O}_y$ (with Ca-doping we can achieve more overdoped region than the case of Ca-free samples). Results are given as a phase diagram in Fig. 2.10. As can be seen from this figure, for the most overdoped sample (nearly 19%), the pseudogap line crosses the T_c dome and goes to the quantum critical point. This will indicate that the pseudogap is not a precursor of superconductivity, but an independent order. On the other hand, despite the improved explanations, in-plane and out-of-plane resistivity curves give significantly different temperature scales for T^* (in-plane case 30-40% lower than out-of-plane). This can be explained with the explanation that the in-plane resistivity is sensitive to the nodal region of the Fermi surface, while the out-of-plane resistivity is sensitive to the antinodal region. In this case, it assumes that the pseudogap gradually opens from the antinodal region towards the nodal region with lowering temperature. Our optical data are mostly consistent with out-of-plane resistivity data.

The pseudogap behavior in the infrared spectra will be given in the next chapter in detail.

2. HIGH TEMPERATURE CUPRATE SUPERCONDUCTORS

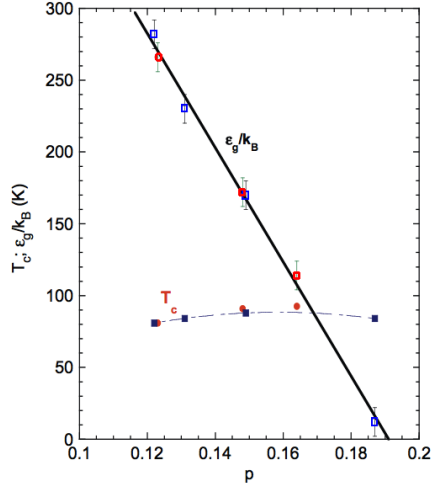


Figure 2.10: T_c and T^* obtained from out-of-plane resistivity - Doping dependent out-of-plane resistivity curves [21]. Black fittings are obtained by theory.

2.2.2 Precursor Superconducting State

Precursor superconductivity has been discussed by many experimental groups. Even though previously the pseudogap state was considered as a precursor of superconductivity, recent experimental results were of a favor of different order scenario. On the other hand, different experimental probes reported the existence of the superconducting fluctuation regime, yet, there is no consensus about the temperature region and doping dependence of these states.

One of the first experiments that reported the existence of a new temperature region in the phase diagram was Nernst effect measurement [22]. Nernst signal and the temperature dependence are shown in Fig. 2.11. Nernst signal shows a tilted-hill behavior that is generic to the cuprates. In the Nernst experiment, the flow of vortices and antivortices with the applied temperature gradient generates signals with opposite signs. Therefore, the Nernst signal will pick up vorticity. The existence of vortex state can be explained even if the long-range phase coherence disappears with the thermally generated vortices and antivortices. On the other hand, the pair amplitude of the Cooper pairs persists up to very high temperatures. In Fig. 2.12, the region with the enhanced Nernst signal is shown.

Another method that proposed the existence of the precursor superconductivity is the ARPES measurements [23]. Previously, the continuous evolution of the gap

2.2 Pseudogap and Precursor Superconducting State

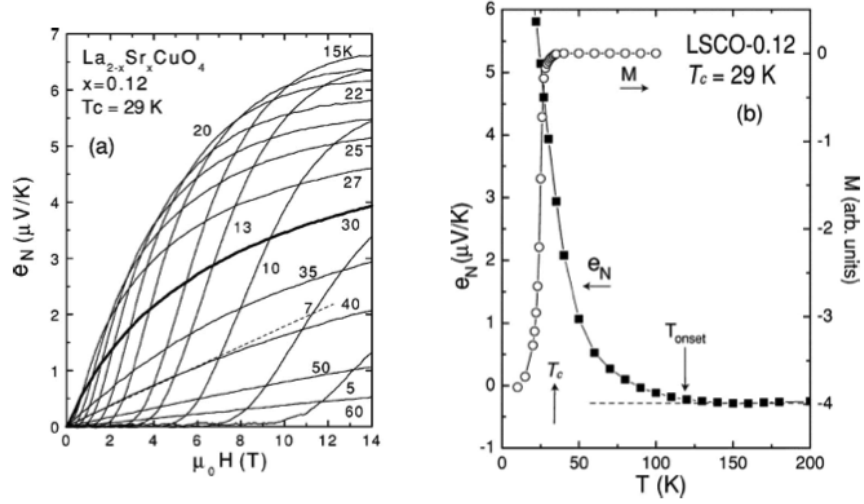


Figure 2.11: Nernst signal of cuprates - Nernst signal of $\text{La}_{2-x}\text{Sr}_x\text{CuO}_4$ in the underdoped region (a). The Nernst signal also given for this sample. The appearance of the Nernst signal starts well above T_c (b) [22].

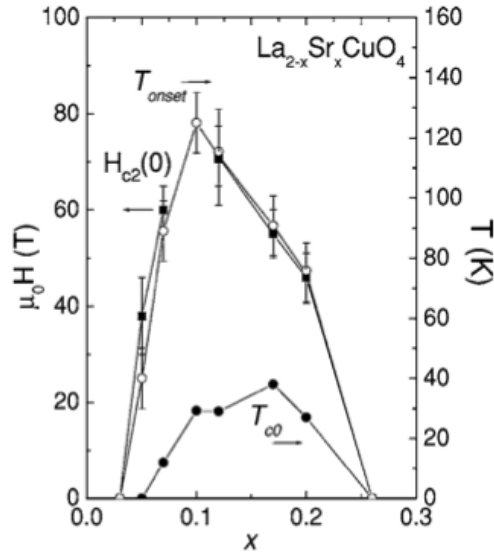


Figure 2.12: Enhanced Nernst signal region for $\text{La}_{2-x}\text{Sr}_x\text{CuO}_4$ - The doping dependence of the Nernst signal for $\text{La}_{2-x}\text{Sr}_x\text{CuO}_4$. Similar behavior also observed for other cuprates [22].

2. HIGH TEMPERATURE CUPRATE SUPERCONDUCTORS

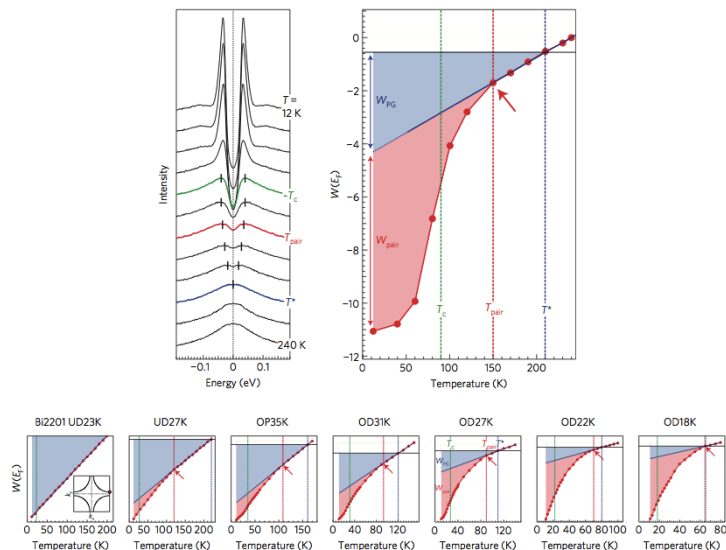


Figure 2.13: Indication of the precursor superconducting state in ARPES measurement - Weighted contributions of the pseudogap and the precursor superconducting state to the ARPES spectral weight. Doping dependence of this state has been given in the bottom panels [23].

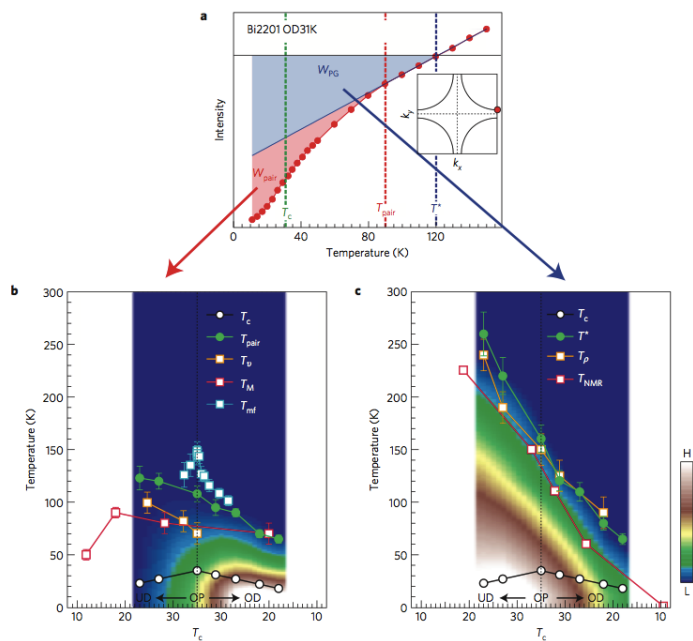


Figure 2.14: Doping dependence of the precursor state obtained by ARPES measurement - The doping dependence of the precursor state and the pseudogap state [23].

2.2 Pseudogap and Precursor Superconducting State

feature from superconducting region to the pseudogap had been interpreted as that the pseudogap and superconducting gap have the common origin. On the other hand, the detailed spectral weight analysis of the ARPES signal showed another scale in between T^* and T_c (Fig. 2.13). The doping evolution of this new scale is also straightforward. With decreasing doping level, it has been found that this temperature scale is increasing and clearly shows a different behavior from the pseudogap one. The contributions of the pairing state (T_{pair}) and the pseudogap on to the spectral weight is shown on the phase diagram in Fig. 2.14. It has been mentioned in this study that the pairing-amplitude and the phase fluctuations are equally important below T_{pair} . Therefore, we cannot interpret this scale as the classically explained superconducting fluctuation regime.

Both ARPES and the Nernst effect measurements show fairly good consistency among them. They both give a precursor state that decreases with increasing doping and extends up to 3-4 T_c as a temperature scale. They are also consistent with other probes such as diamagnetism measurements. If this contribution indeed originates from superconductivity, then it might be explained with a phase separated state [24] or unusually fast vortices [25, 26]. The later one was theoretically proposed, however, such kind of experimental observation has not been reported. Other experiment groups, such as microwave and terahertz, on the other hand, reported a temperature scale that follows the doping dependence of the T_c dome and only extends up to close vicinity of T_c .

Terahertz in-plane transmittance measurement was performed on $\text{La}_{2-x}\text{Sr}_x\text{CuO}_4$ cuprate thin films over the entire phase diagram. The superfluid density was calculated by using the imaginary optical conductivity. In Fig. 2.15, the doping dependent variable (related to the superfluid density) as a function of temperature is plotted. As it will be explained later in this thesis, in the result and discussion part, this data also include a normal carrier component. Since the samples are metallic, a Drude component of the normal carriers should be considered in this variable. On the other hand, THz-time domain measurements can only be performed in a low energy (limited) region. Therefore, to determine the normal carrier component is not an easy job and was not done here. Hence, the rapid changes of this variable were taken into account as the indication of the appearance of the superfluid density. The rapid changes were traced with the second derivative of this variable with respect to the temperature.

2. HIGH TEMPERATURE CUPRATE SUPERCONDUCTORS

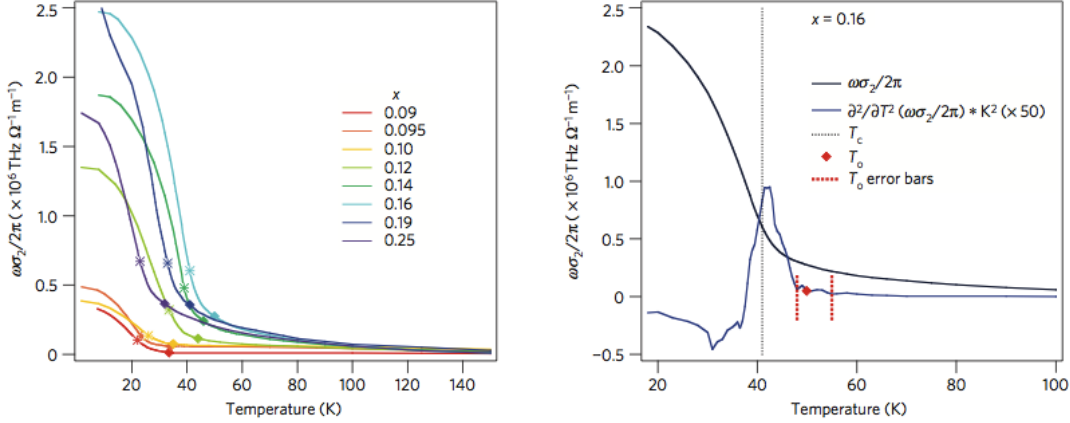


Figure 2.15: Superfluid density along in-plane of the cuprates revealed by THz-time domain spectroscopy - Doping dependent superfluid density curves of $\text{La}_{2-x}\text{Sr}_x\text{CuO}_4$ [27]. Stars are T_c values, while circles define the precursor state. Right panel shows the obtaining method of the precursor state.

Analysis in this study showed that the observed region can be explained with usual Ginzburg-Landau formalism [28]. On the other hand, it is significantly different from what was observed in diamagnetism [29] or Nernst effect [22] measurements. A general view has been plotted in Fig. 2.16. One possibility to this discrepancy is that the probes like diamagnetism, etc. might be sensitive to something other than superconductivity. Furthermore, there might be two different kinds of fluctuations, while one of them greatly contribute to the magnetism, the other one may contribute to the conductivity. A convincing explanation has yet to be found.

Microwave measurements also reported similar results to that of THz measurements. In principle, these two methods are similar, where the microwave measurement is more confined to the low energy. However, to obtain the superfluid density (imaginary optical conductivity), we have to assume some theoretical work and analysis. These make the situation more complicated [30].

2.3 General Optical Properties of Cuprates

2.3.1 In-plane and c -axis optical properties

In the last three decades many cuprate families have been discovered. Even though the chemical composition and structure of these families greatly differ from each other, they

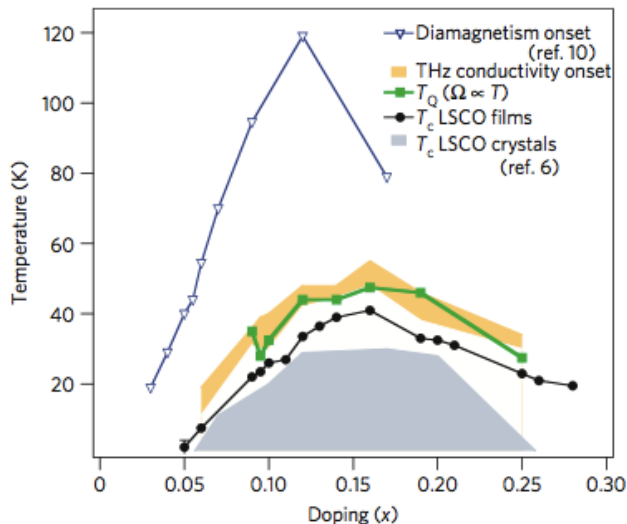


Figure 2.16: Precursor superconductivity state revealed by THz-time domain measurements - Phase diagram of $\text{La}_{2-x}\text{Sr}_x\text{CuO}_4$ [27]. Comparison with other probes also given. Precursor state does not extend up to very high temperatures and follow T_c dome.

all have common copper oxide planes, where the superconducting current flows, and a metallic response can be observed within those planes. Transport along the c -axis, on the other hand, is significantly different from the in-plane one. It is incoherent in the normal state and originates from the hopping between the copper oxide planes, which gives rise to a semiconducting behavior along the c -axis. Below the critical temperature, system becomes superconducting along the c -axis due to the Josephson coupling of the conducting planes. Therefore, the conductivity along c -axis is orders of magnitude smaller than the conductivity in planes. In Fig. 2.17 the difference between c -axis and in-plane transport can be seen clearly. These results belong to one of the prototypical cuprate superconductor $\text{YBa}_2\text{Cu}_3\text{O}_y$ for several oxygen concentrations (y).

The optical properties of cuprates also greatly differ in between in-plane and out-of-plane directions. At high energies both spectra reflect the intraband transitions. At low energies, we can observe Drude like behavior along the in-plane of cuprates that reflects the metallic behavior. The electronic component along the in-plane conductivity is very strong, and therefore, the contributions of the phonon effects are difficult to be observed (many cases they are wiped out in the electronic component) and very weak. In contrast, the c -axis conductivity is dominated by phonon modes with a weak

2. HIGH TEMPERATURE CUPRATE SUPERCONDUCTORS

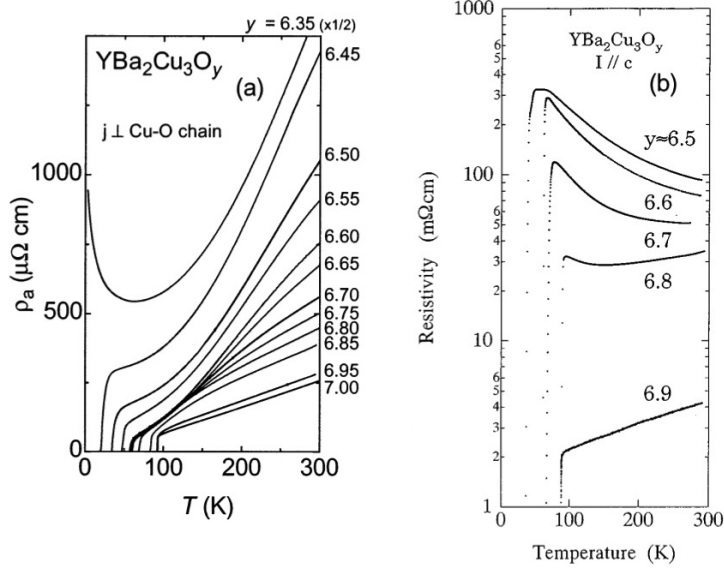


Figure 2.17: Doping dependent resistivity - inplane and c -axis - Doping dependent resistivity of YBa₂Cu₃O_y for (a) in-plane and [31] (b) c -axis directions [32].

electronic component. In Fig. 2.18, the generic behaviors of optical conductivity for the in-plane and out-of plane polarization are given. There are many interesting properties of the in-plane response of the cuprate superconductors. But the main topic of this thesis is related with the c -axis properties. Therefore, from now on the general behavior in this polarization will be discussed in more detail.

In-plane conductivity shows metallic behavior over the wide doping region and for all the superconducting samples, c -axis on the other hand, semiconducting for the samples with lower doping. It becomes metallic for the optimally doped and overdoped samples. For YBa₂Cu₃O_y (this sample is special) the c -axis conductivity is higher compared to the other cuprates due to the crystal structure of the YBa₂Cu₃O_y, where we know the existence of the CuO chain structure in addition to the Cu₂O planes. Therefore, the hopping between the planes becomes easier due to the chain structures. In YBa₂Cu₃O_y and another class of cuprate YBa₂Cu₄O₈ that has a double chain structure, c -axis conductivity is relatively higher than in the other cuprates. In Fig. 2.19, optical conductivity at the optimally doped region is given for a single-, double-, and trilayer cuprate family. As can be seen from this figure, YBa₂Cu₃O_y has the highest

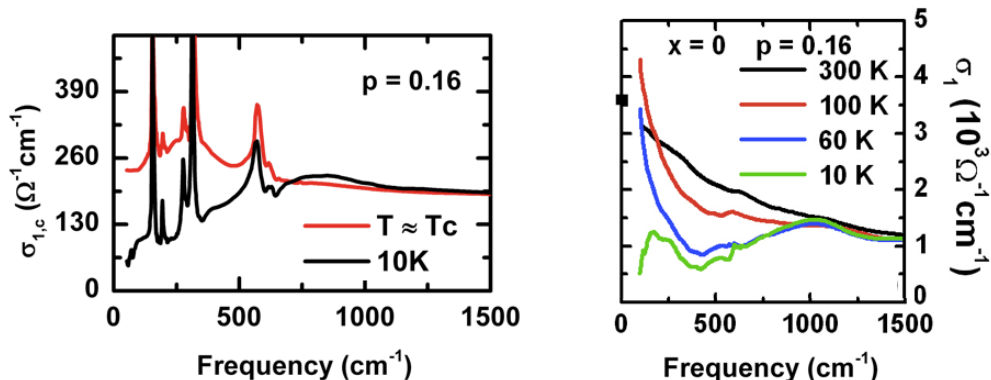


Figure 2.18: Inplane vs. c -axis optical conductivity - Doping dependent optical conductivity of $\text{YBa}_2\text{Cu}_3\text{O}_y$ for c -axis (left panel) and inplane (right panel) direction.

conductivity among the cuprates at the same doping level. For instance, the c -axis conductivity at the optimally doped region for $\text{YBa}_2\text{Cu}_3\text{O}_y$ is one order of magnitude higher than the $\text{La}_{2-x}\text{Sr}_x\text{CuO}_4$ at the same doping level. This is one of the reasons why we chose $\text{YBa}_2\text{Cu}_3\text{O}_y$ system to work with in this study, where the details will be explained further in later chapters.

2.3.2 Pseudogap and superconducting gap behavior in c -axis optical spectrum

The pseudogap state has been observed by many spectroscopic probes as discussed in Ref. [36]. Optical spectroscopy is an especially powerful probe because it can clearly distinguish a superconducting gap from the insulating gaps. In particular, the c -axis polarized optical spectrum is very sensitive to the electronic density of states in the antinodal region [37, 38] of the Fermi surface near $(0, \pi)$ and $(\pi, 0)$, where the pseudogap has a strong effect, while a major pseudogap effect on the in-plane spectra is the reduction of the carrier scattering rate [39]. Therefore, it is possible to observe the pseudogap state more easily in the c -axis conductivity ($\sigma_{1,c}(\omega)$) than in the a -axis one ($\sigma_{1,a}(\omega)$).

In Fig. 2.20 the optical conductivity spectrum for an under doped $\text{YBa}_2\text{Cu}_3\text{O}_y$ is shown. T_c of this sample is approximately 70 K. This graph clearly demonstrates the suppression of the low energy optical conductivity that starts much above the super-

2. HIGH TEMPERATURE CUPRATE SUPERCONDUCTORS

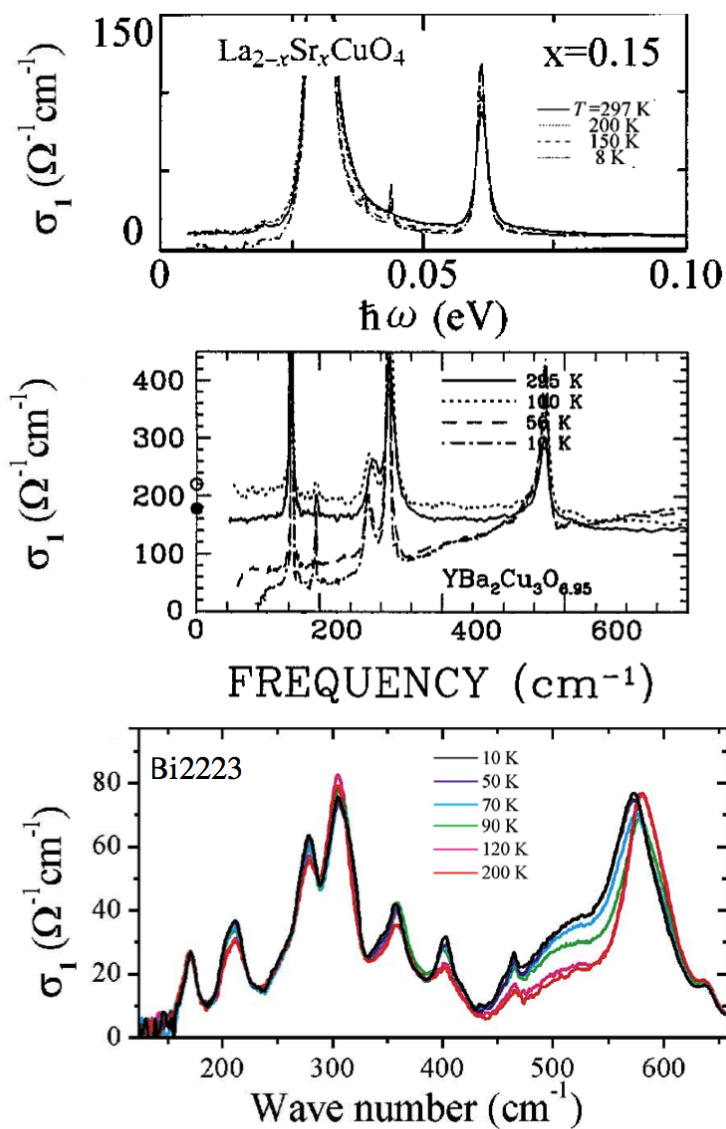


Figure 2.19: Comparison of the c -axis optical conductivity for several cuprate family - Optical conductivity of single layer $\text{La}_{2-x}\text{Sr}_x\text{CuO}_4$ [33], double layer $\text{YBa}_2\text{Cu}_3\text{O}_y$ [34], and trilayer $\text{Bi}_2\text{Sr}_2\text{Ca}_2\text{Cu}_3\text{O}_{10}$ [35].

conducting transition. In Fig. 2.20(b), the phonon modes are subtracted; therefore, it is easier to see this suppression. Moreover, in the inset of the graph, the conductivity at 50 cm^{-1} normalized with respect to the room temperature conductivity (open circles) is given.

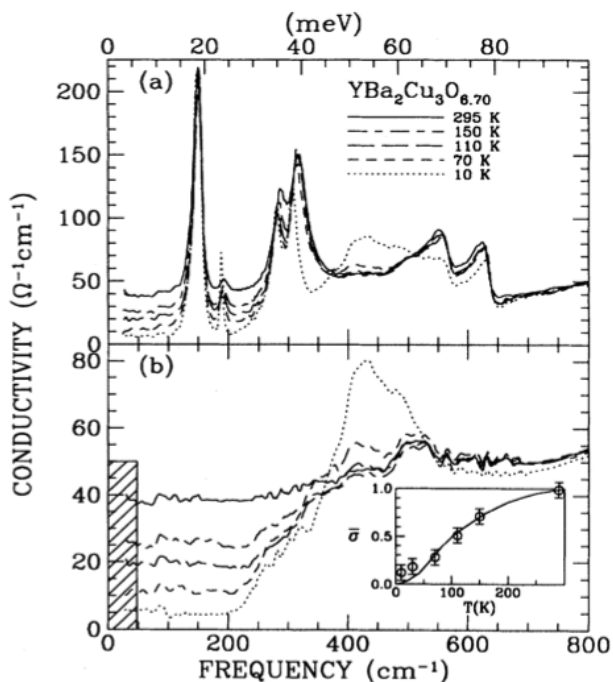


Figure 2.20: Pseudogap behavior in the c -axis optical conductivity - Optical conductivity of underdoped $\text{YBa}_2\text{Cu}_3\text{O}_y$ ($T_c = 70 \text{ K}$) [40]. (b) shows the same plot after subtracting the phonon modes. Inset: the conductivity at 50 cm^{-1} normalized with respect to the room temperature conductivity (open circles) together with Knight shift (solid line).

The suppressed spectral weight in the low energy region will be transferred to the high energy region in the pseudogap state. In Fig. 2.21(a), the transfer to the high energy region can be seen. In the superconducting state, on the other hand, the low energy optical conductivity is suppressed and it is transferred to the $\delta(0)$. Fig. 2.21(b) shows the superconducting gap behavior. As can be seen from the figure, the low energy conductivity decreases and is lost from the spectrum. The absorption like structures pointed by the arrows in the graph are the structures ascribed to the transverse Josephson plasma (TJP) mode that will be explained in the next section. In Fig. 2.21(c), the low energy spectral weight has been calculated which shows the

2. HIGH TEMPERATURE CUPRATE SUPERCONDUCTORS

continuous suppression of the low energy conductivity starting from the pseudogap temperature, T^* and continues below T_c .

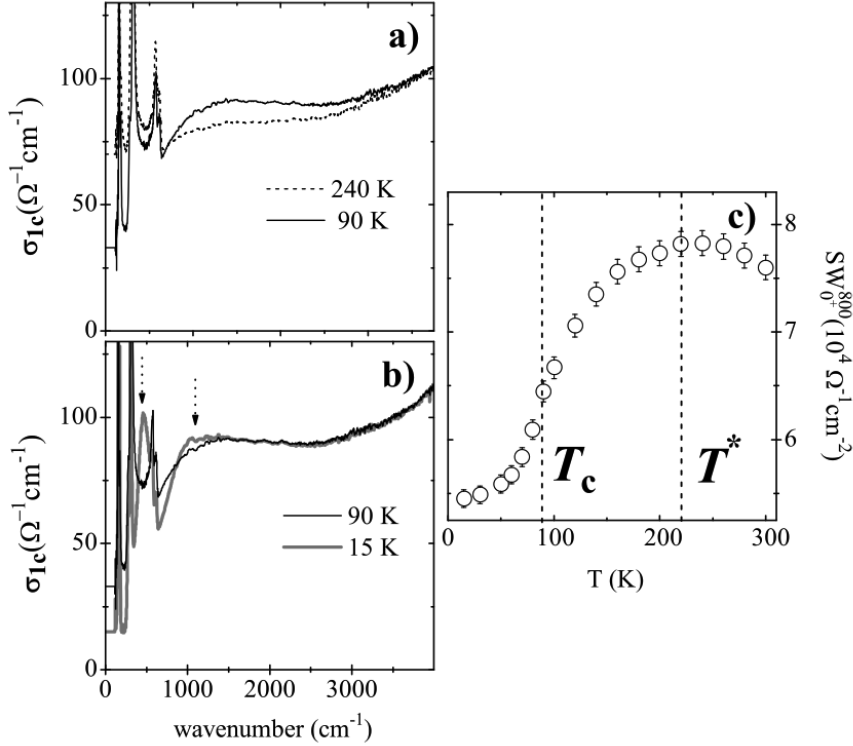


Figure 2.21: Pseudogap and superconducting gap in the c -axis optical conductivity - spectral weight calculation - Optical conductivity of underdoped $\text{NdBa}_2\text{Cu}_3\text{O}_y$ ($T_c = 85$ K) [41]. (a) High energy transfer with pseudogap opening. (b) Behavior of the superconducting state (Low energy suppression without high energy transfer). (c) shows the spectral weights of specific energy region, 0 - 800 cm^{-1} .

2.3.3 Superfluid density in c -axis optical spectra

The most significant behavior of the superfluid density in the c -axis optical spectrum is the formation of the Josephson plasma edge in the reflectivity spectrum. In Fig. 2.22 the behavior of the Josephson plasma resonance is given for $\text{La}_{2-x}\text{Sr}_x\text{CuO}_4$ for several doping levels. With superconducting transition, the reflectivity at high frequencies starts to drop, which forms a dip and then at lower frequencies it reaches to unity. With decreasing temperature and with increasing doping level, this dip position shifts to the higher energy region. For $\text{La}_{2-x}\text{Sr}_x\text{CuO}_4$ sample this edge position is confined

2.3 General Optical Properties of Cuprates

below 100 cm^{-1} , on the other hand for $\text{YBa}_2\text{Cu}_3\text{O}_y$ it might be as high as 300 cm^{-1} . This edge is called Josephson plasma edge, because the study of the doping evolution, etc. led to the conclusion that this feature originates from the Josephson coupling between the CuO_2 planes.

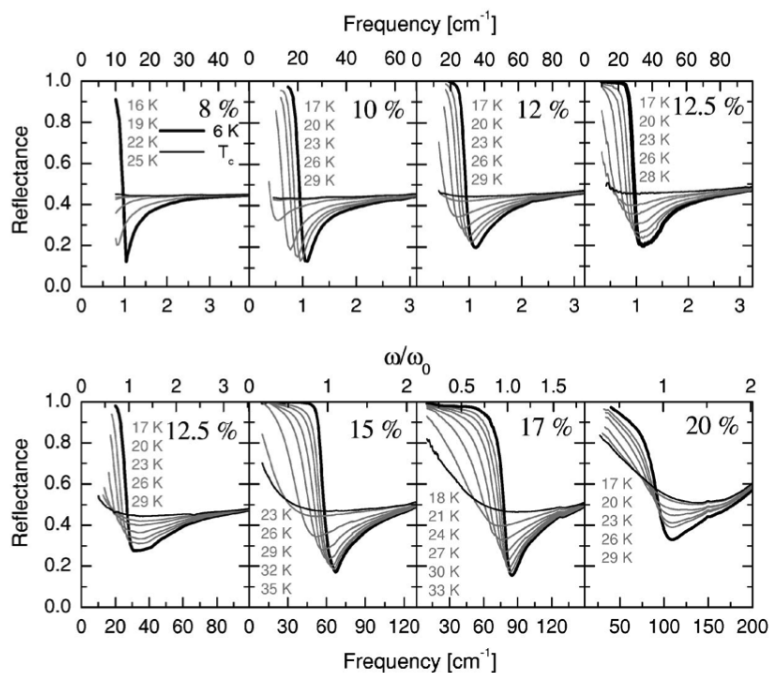


Figure 2.22: Doping dependent Josephson plasma edge - Doping dependent Josephson plasma edge of $\text{La}_{2-x}\text{Sr}_x\text{CuO}_4$. With increasing doping level, the edge position shifts to the higher energies [42].

As mentioned previously, the superconducting carriers are condensed to the δ -function at zero frequency, and therefore, the spectral weight that is associated with this δ -peak defines the superfluid density. The density of the condensed electrons can be defined with the penetration depth. A detailed characterization regarding the electro-dynamics of the superconducting state will be explained in Chapter 3, optical constants section. However, it has been shown that in the case of a Josephson array like c -axis dynamics, the penetration depth can be explained with the relation: $\lambda_c^{-2} \propto \sigma_c$ [43, 44], where indeed this relation had been observed for the c -axis case of the cuprates for a wide doping range. In Fig. 2.23 the general behavior of the penetration depth is shown

2. HIGH TEMPERATURE CUPRATE SUPERCONDUCTORS

for several cuprate families. Please note that the penetration depth is calculated from the missing area of the real part of the optical conductivity in this case. Some other theoretical explanations are also proposed [45, 46, 47, 48].

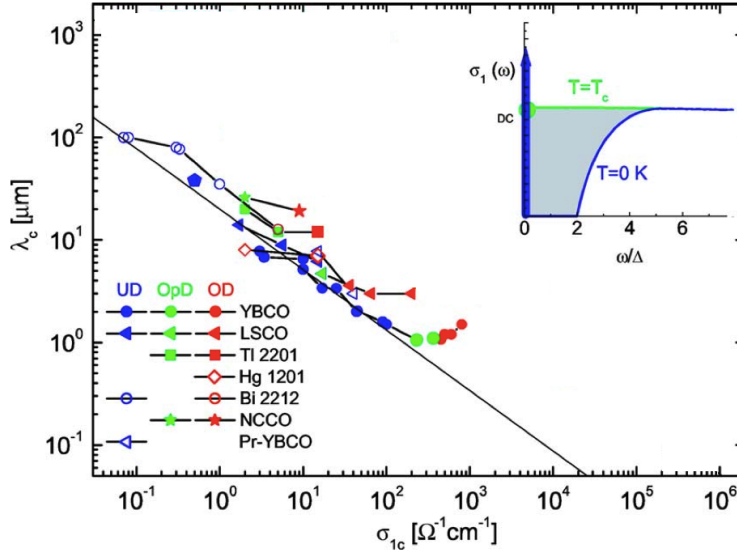


Figure 2.23: Penetration depth vs. dc conductivity curve of cuprates - Doping dependence of the penetration depth with respect to dc conductivity for cuprates [49].

2.3.4 Transverse Josephson plasma (TJP) resonance mode

As mentioned previously, *c*-axis optical conductivity is dominated by the phonon modes at low energy region and reported for many cuprate families. As the superconducting response, the low energy optical conductivity is suppressed and the lost spectral weight is transferred to the δ -function at zero frequency. However, for some of the cuprates, a broad absorption peak was observed around $\sim 400 \text{ cm}^{-1} - 500 \text{ cm}^{-1}$. Even though, in early studies it has been thought as a phonon mode, in reality it is too broad to be a phonon mode. Later on van der Marel and coworkers proposed an explanation [50] that takes into account of a geometrically separated consecutive metallic layers as shown in Fig. 2.24. There are two different Josephson junctions resonating in the interbilayer and intrabilayer part of the unit cell, which introduces a new transverse mode at finite frequency region in addition to the bulk plasma mode at zero frequency. In this explanation two or more metallic layer compounds are predicted to show an

2.3 General Optical Properties of Cuprates

absorption at finite energy region. Indeed, it has been observed for many multilayer cuprate families (two and three layer). Moreover, if the system has alternating different blocking layers, even if the system has only single layer, the TJP resonance mode can be observed (Like in $\text{SmLa}_{1-x}\text{Sr}_x\text{CuO}_{4-d}$ [51]).

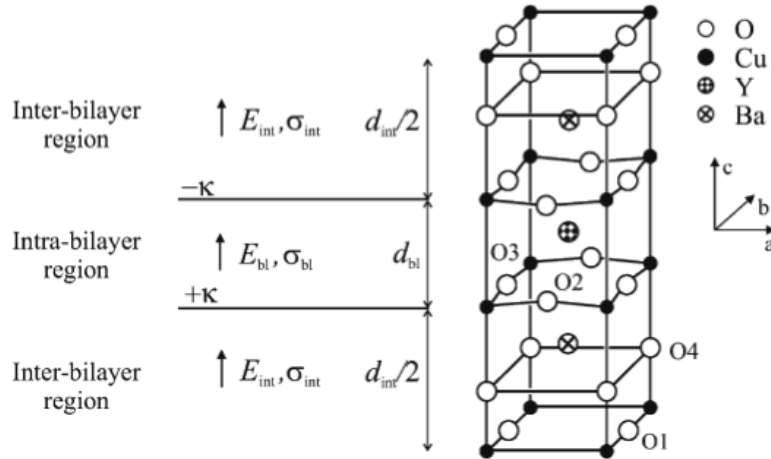


Figure 2.24: Schematic of intra-bilayer and inter-bilayer formation in the crystal structure - In multilayer compounds the alternating planes causes the TJP mode [41].

This model is very successful to explain the growth of a broad peak in the c -axis spectra, and it can explain the observed phonon anomalies. Especially, the phonon mode resulting from the in-plane oxygen and Cu bending mode is highly affected by the TJP resonance. Originally, this mode was assigned to Josephson currents, and it was thought to appear at T_c , like the Josephson plasma edge. However, later on a careful examination of this mode and the phonon anomalies showed that, in reality it starts to appear at temperatures much higher than the T_c [52], and it has been attributed to the preformed Cooper pairs as a precursor of superconductivity [41, 53]. In Fig. 2.25 the evolution of the absorption peak related to the TJP mode is shown.

Beside the observed anomalies on the phonon modes, TJP mode has a complicated behavior. For instance, it has been found that the TJP mode can split in the existence of the phonon modes [54]; some impurity doping such as Zn to Cu sites in the planes

2. HIGH TEMPERATURE CUPRATE SUPERCONDUCTORS

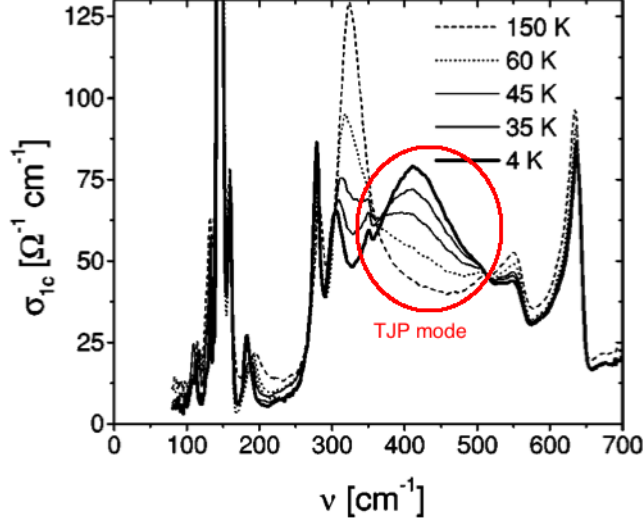


Figure 2.25: Transverse Josephson plasma resonance in the c -axis optical spectrum - Evolution of the TJP mode in the c -axis optical spectrum [52].

can suppress this mode; and in the existence of a magnetic field TJP mode can be suppressed. Moreover, it has been shown that the observed frequency range of the TJP mode is not always the same energy range, but it changes with changing the doping level [52, 55]. This is in a sense is reasonable, since the Josephson plasma edge also shifts in energy region with doping. This is the indication of the change of the superfluid density, just like the Josephson plasma edge. Nonetheless, during the data analysis, it is necessary to be careful.

2.3.5 Impurity effect on c -axis optical properties

It might be preferred to study impurity free systems, when we try to understand the fundamentals of a phenomenon, since introducing impurities may have complicated effects on the observed properties. However, controlled impurities will allow us to obtain some desired properties that may help us to understand the phenomena more easily. Some effects of impurities on cuprate superconductors were studied, and in this section these studies done on c -axis optical properties will be summarized.

Impurity effects can be classified into two groups: effects on normal state properties and effects on superconducting state properties. The most common, impurity effect on

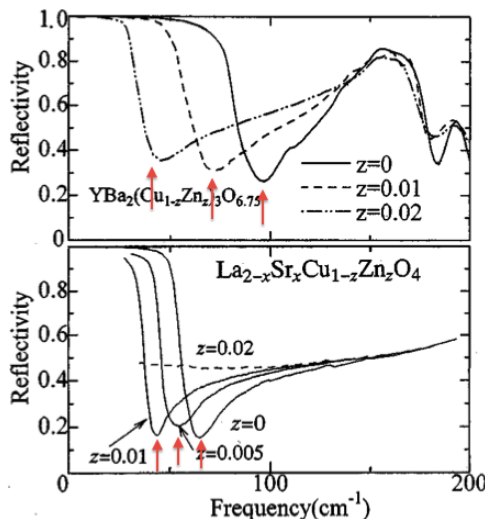


Figure 2.26: Impurity effect on Josephson plasma frequency - Behavior of the Josephson plasma edge with Zn-substitution for $\text{YBa}_2(\text{Cu}_{1-x}\text{Zn}_x)_3\text{O}_y$ and $\text{La}_{2-x}\text{Sr}_x\text{Cu}_{1-z}\text{Zn}_z\text{O}_4$ [56].

high temperature cuprate superconductors is the gradual suppression of T_c . Significant effects are observed also in the c -axis optical properties.

The first change in the spectrum is the shift of the Josephson plasma edge to the lower energy region. In Fig. 2.26 this effect is shown for the two cuprate families. This is an expected behavior, since Josephson plasma is the signature of the collective motion of the superconducting carriers in the reflectivity spectra; hence the edge position is related with the superfluid density. Impurities act as pair breakers and decrease the superconducting carrier density, causing a shift of the Josephson plasma edge [56].

Secondly, a change in the TJP resonance mode was observed for the Zn-substituted systems. The softening of the phonon modes related with the TJP resonance mode was also recovered for the Zn-substituted samples. Even though some phonon modes become slightly asymmetric, this difference is negligibly small. This is also surprising especially because the splitting of the phonon band with disorder is expected. In Fig. 2.27, the effect of impurity doping on to TJP mode has been shown.

Another impurity effect on the spectrum can be observed in the overdoped region of the phase diagram. A low energy absorption, so-called residual conductivity at lower energies than the superconducting condensation energy, is observed for many cuprate

2. HIGH TEMPERATURE CUPRATE SUPERCONDUCTORS

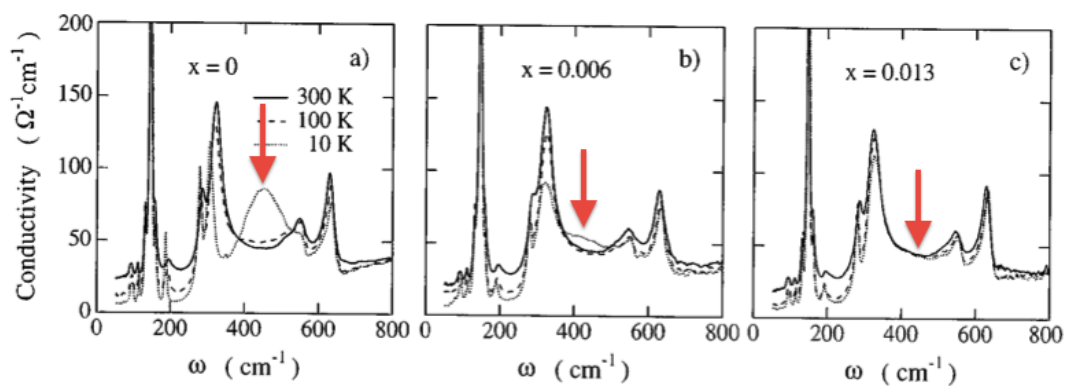


Figure 2.27: Impurity effect on Transverse Josephson plasma mode - Behavior of the transverse Josephson plasma resonance with Zn-substitution for $\text{YBa}_2(\text{Cu}_{1-x}\text{Zn}_x)_3\text{O}_y$. TJP mode is suppressed gradually with increasing Zn-content [57].

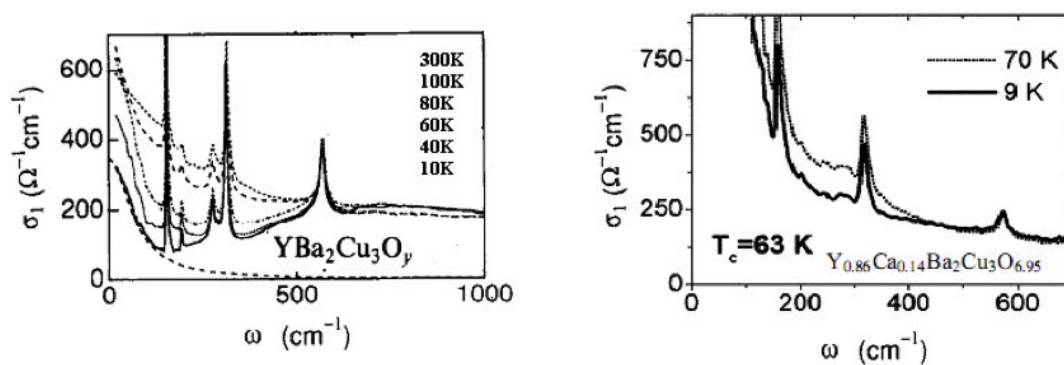


Figure 2.28: Impurity effect on c -axis properties in the overdoped region - Increase of the residual conductivity with impurity doping [58, 59].

families [60, 61] (Fig 2.28 [58, 59]). The residual conductivity was observed for both in plane and c -axis polarization. It seems that this behavior is intrinsic to the cuprates in the overdoped region. This can be related to the electronic inhomogeneities due to phase separation or pair-breaking occur with the carrier-overdoping. In addition to the intrinsically observed overdoping effect, it is also pointed out that the residual conductivity is increasing with impurity substitution [62], which can be discussed in terms of disorder-induced pair breaking effects.

2.4 Aim of This Study

Despite the variety of the experimental probes and the work done on the pseudogap, there are many questions remained about the content of the pseudogap. The relation of pseudogap with superconductivity; the behavior of the pseudogap in the superconducting region, and the overdoped regime of the phase diagram, still needs to be investigated. In this thesis, the controlled impurities were used to obtain some answers in addition to a systematic doping dependent study. The pseudogap region has been investigated over a wide doping range, in a wide energy region (essential for detailed analysis), and with smaller temperature intervals. So far there has been no systematic study for Zn- and carrier-doping dependence of the c -axis optical spectra, which satisfies all the conditions above.

Moreover, the precursor superconductivity idea should be revisited with more accurate analysis of the data. This motivated us to measure the high and low energy optical spectra for a series of crystals that is thick along c -axis enough for accurate analysis. In many cases, it was difficult to obtain such big crystals; hence measurements were difficult.

Finally, although there are some reports about the kinetic energy driven superconductivity in cuprates for which some pieces of evidence were given by the results of the c -axis infrared spectroscopy, there is no report on this issue for the impurity introduced samples. This systematic study will provide some insight to this topic, as well.

2. HIGH TEMPERATURE CUPRATE SUPERCONDUCTORS

3

Experimental Procedure

3.1 Samples

To obtain large homogeneous single crystals with a good quality surface along c -axis is relatively difficult process, compared to the ab -plane surface. Samples used in this study were grown with a pulling technique [63]. Sample sizes were approximately 2.5 mm² in the ac -plane, and the Zn concentrations in the samples were homogeneous, which can be seen with a sharp superconducting transition (Fig. 3.1). Superconducting transition temperatures of the samples are determined with dc susceptibility measurements. Susceptibility measurements are performed on samples, that the FTIR measurements are performed. The magnetic susceptibilities of the samples are obtained with the Magnetic Property Measurement System Superconducting Quantum Interference Device (MPMS SQUID) with applied 10 Oe magnetic field and with the zero field cooling (ZFC) method. In ZFC configuration, the sample is cooled down below the superconducting transition temperature without applying any magnetic field and at low temperature a magnetic field is applied. Then the magnetization of the sample will be measured with a temperature sweep under a constant magnetic field. T_c values are determined as the middle of the transition curve, and the width ΔT_c of the superconducting transition was estimated by the 10-90% criterion of the transition curve.

All the samples are placed in a tube furnace with an alumina boat and the tube is sealed with glass fibers to keep the temperature stable inside the furnace. Samples are annealed under 100% oxygen flow at specific temperatures for each doping level.

3. EXPERIMENTAL PROCEDURE

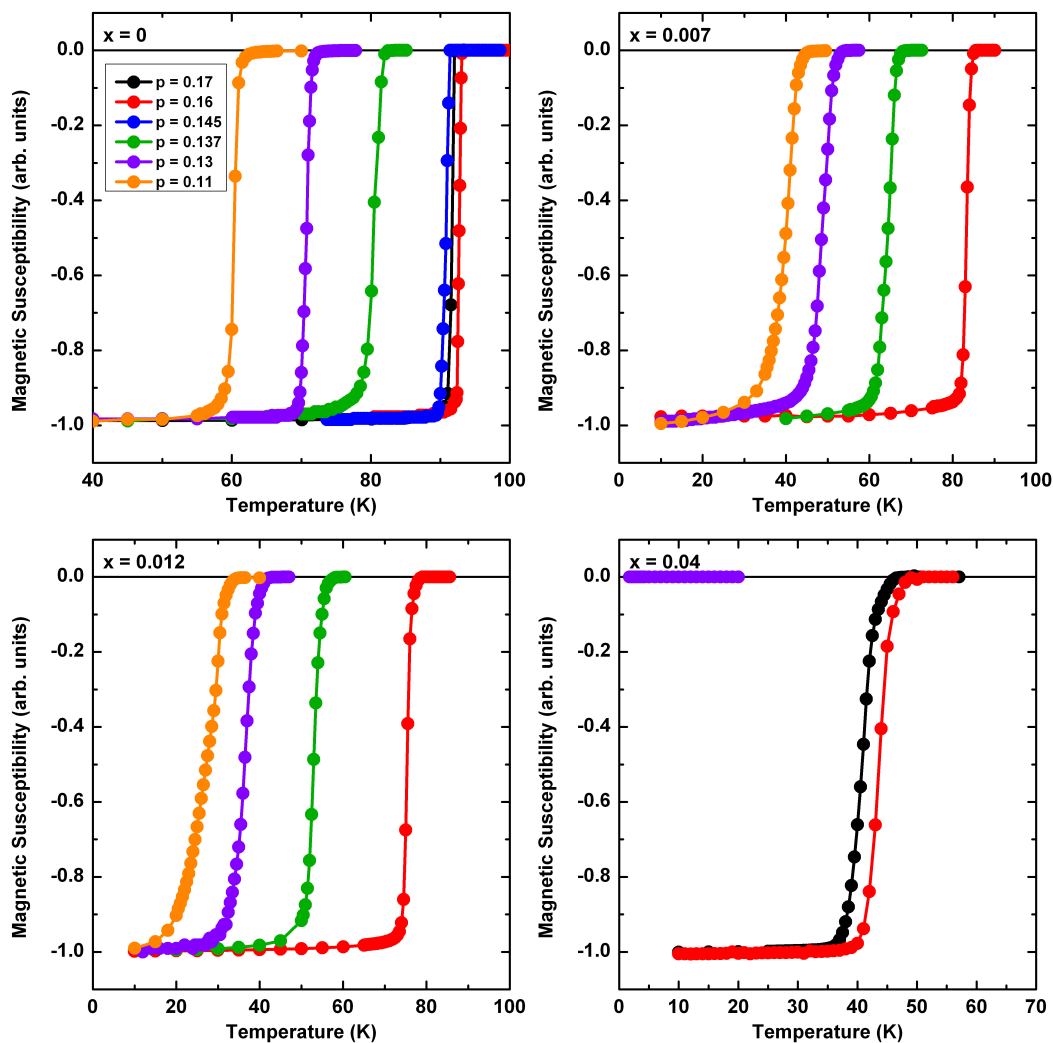


Figure 3.1: Zn- and doping dependence of dc magnetic susceptibility - Magnetic susceptibility of the samples used in measurements. Please note that, the FTIR spectroscopy of the $p = 0.16$ of $x = 0.012$ and 0.04 had not been measured. These data has been given for comparison.

Temperature is raised to the desired temperature quickly (within 15-20 min.) and kept at that temperature for 2-3 weeks that is depend on the doping level. The minimum annealing time depends on the sample size and the doping level that we want to achieve. At higher doping region, samples are annealed at low temperatures; therefore, it is necessary to anneal the samples longer time. For the low doping samples, we use high temperature annealing, where the oxygen diffusion becomes easier, hence the annealing time is decreasing. Annealing temperatures are determined from the annealing temperature vs. oxygen concentration curve that is given by the Jorgensen *et al* [64]. Zn-substitution to the Cu site does not alter the oxygen concentration; therefore, the annealing conditions to obtain the same doping level were the same as the Zn-free samples. We annealed the Zn-free and Zn-substituted samples together to keep the annealing condition in the maximum accuracy. After the annealing is finished, samples are quenched into liquid nitrogen. For small samples a copper plate can be used as the quenching environment, as well. However, in our case the samples are quite big, therefore, it is difficult to cool them down to the room temperature quickly with the copper plates, hence, liquid nitrogen has been chosen. If the cooling rate is low, the oxygen concentration in the system changes very quickly, and it becomes difficult to obtain the wanted doping level.

Previously an empirical formula has been proposed to determine the doping level of the cuprates with a known T_c , as is given in Eq. 3.1. However, this empirical formula does not work for all the cuprate systems. For instance $\text{YBa}_2\text{Cu}_3\text{O}_y$, used in this study, shows a plateau region around 1/8 doping level. Therefore, the T_c vs doping level p curve significantly deviates from the empirical formula as can be seen in Fig. 3.2. Instead of using the empirical formula we determined the doping levels of the samples by the literature values [65], which has been evaluated from the relation between the c -axis lattice constant vs oxygen concentration. Since the doping levels do not change with Zn-substitution, we determined the doping level of the Zn-substituted samples based on the Zn-free ones. This determination works well, since we can see a specific behavior in the optical conductivity, that will be explained in later chapters. The annealing conditions, T_c values with the transition width ΔT_c and the corresponding doping levels are given in Table 3.1.

$$\frac{T_c}{T_{c,max}} = 1 - 82.6 \times (p - 0.16)^2 \quad (3.1)$$

3. EXPERIMENTAL PROCEDURE

Table 3.1: Zn-content (x), doping level (p), T_c , transition width ΔT_c and annealing condition

Zn-content (x)	Doping Level (p)	T_c (K)	ΔT_c (K)	Annealing condition
0	0.17	92	0.5	450 °C, 5 weeks
0	0.16	93.5	0.5	500 °C, 3 weeks
0	0.145	89	0.5	540 °C, 3 weeks
0	0.137	81	2	580 °C, 3 weeks
0	0.13	71	3	625 °C, 2 weeks
0	0.11	61	3	675 °C, 2 weeks
0	0.06	15	7	740 °C, 2 weeks (in nitrogen flow)
0.007	0.16	82	1	500 °C, 3 weeks
0.007	0.137	64	4	580 °C, 3 weeks
0.007	0.13	53	6	625 °C, 2 weeks
0.007	0.11	43	7	675 °C, 2 weeks
0.012	0.137	53	5	580 °C, 3 weeks
0.012	0.13	37	5	625 °C, 2 weeks
0.012	0.11	29	7	675 °C, 2 weeks
0.04	0.17	40	2	450 °C, 5 weeks
0.04	0.13	non superconducting		625 °C, 2 weeks

The Zn-contents, x , of the samples are determined from the work of the Masui *et al* [66]. Zn content vs. maximum T_c curve is prepared by using their data, where the amount of Zn is determined with the inductively coupled plasma (ICP) analysis (Fig. 3.3). And then from the linear fitting of the data the Zn-contents have been decided for the samples that are used in this study.

Flat, mirror-like surfaces are necessary for the infrared measurements. The samples are polished with the Al_2O_3 powders gradually as fine as $0.3 \mu\text{m}$ prior to the annealing. After annealing, before the reflectivity measurements, a final polishing is performed with $0.3 \mu\text{m}$ Al_2O_3 powders to obtain clean surface before the measurements. The T_c of the samples are checked after the final polishing performed and the sample is placed on the sample holder by using silver paste.

3.2 Principle of the Fourier Transform Infrared (FTIR) Spectroscopy

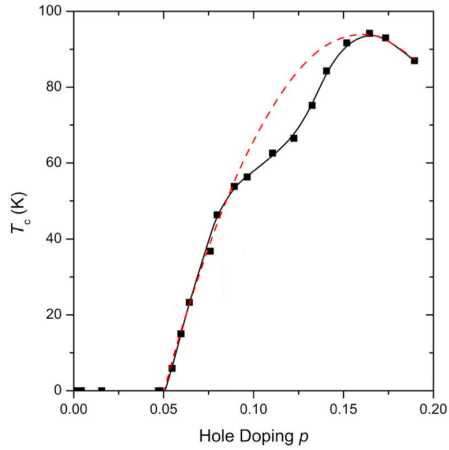


Figure 3.2: Doping level vs T_c curve of $\text{YBa}_2\text{Cu}_3\text{O}_y$. Solid symbols are experimental results, while the red dashed curve is the empirical formula for $\text{YBa}_2\text{Cu}_3\text{O}_y$ [65].

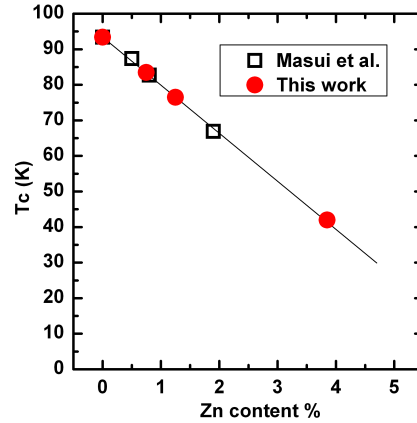


Figure 3.3: Zn content vs. maximum T_c curve of $\text{YBa}_2\text{Cu}_3\text{O}_y$. Open symbols are from [66], close symbols are the samples that are used in this study.

3.2 Principle of the Fourier Transform Infrared (FTIR) Spectroscopy

Infrared radiation is the region that lies between the microwave and the visible region of the electromagnetic spectrum. Electromagnetic radiation interacts with material in different ways and different phenomena can be observed for the light propagating the material such as refraction, scattering, interference, and diffraction. Infrared spectra are based on the transitions between quantized vibrational energy states. Samples in all phases of matter can be studied with infrared spectrometry.

FTIR (Fourier Transform InfraRed) spectrometers have a dominant position for the measurements of infrared spectra. In FTIR spectrometry, all the wavelengths are measured at all times during the measurement (the multiplex or Fellgetts advantage). Moreover, more radiation can be passed between the source and the detector for each resolution element (the throughput or Jacquinots advantage). Due to these advantages, transmission, reflection and emission spectra can be measured significantly faster and with higher sensitivity with FTIR, compared to prism or grating monochromator.

The design of many interferometers used for infrared spectrometers today is based on the two-beam interferometer originally designed by Michelson in 1891. Moreover,

3. EXPERIMENTAL PROCEDURE

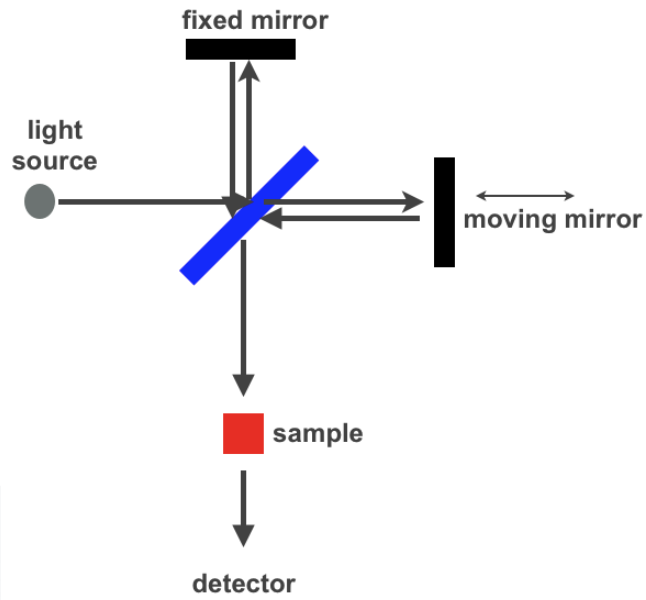


Figure 3.4: Schematic of a Michelson interferometer - Schematic of a Michelson interferometer.

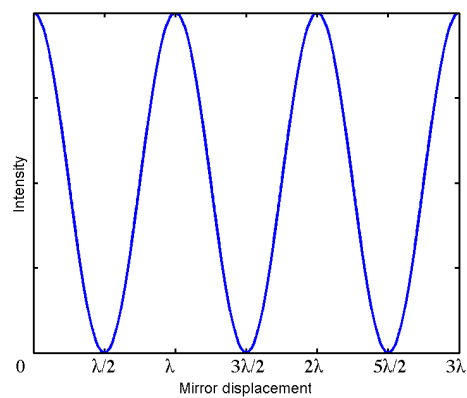


Figure 3.5: Schematic of an interferometer of monochromatic light - Schematic of an interferogram of monochromatic light.

3.2 Principle of the Fourier Transform Infrared (FTIR) Spectroscopy

some other two- beam interferometers also have similar basics. A schematic of this interferometer is shown in Fig. 3.4. The Michelson interferometer is a device that can divide a beam of radiation into two paths and then recombine them after a path difference is introduced. The variation of intensity of the beam emerging from the interferometer is measured as a function of path difference by a detector.

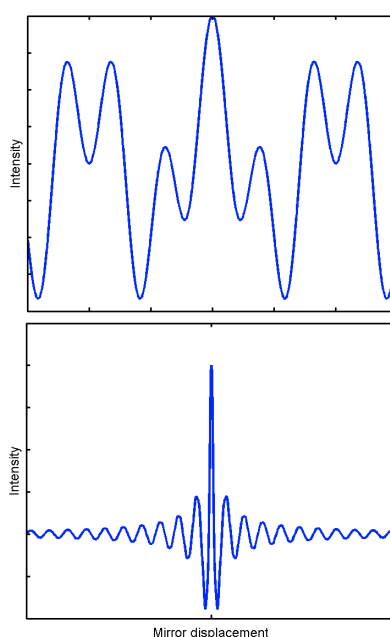


Figure 3.6: Schematic of an interferogram of polychromatic light - Upper panel: Interferogram for a light source with two wavelength. Bottom panel: Interferogram for a polychromatic light.

A detailed explanation regarding to the interferometers has been given in Ref. [67]. If we consider a monochromatic light, the obtained intensity will be given as a function of the displacement of the moving mirror. The split light reflected from the fixed and moving mirrors will produce a destructive interference when the wavelength of the light source is equal to $m\lambda$, while they exhibit constructive interference when the wavelength of the light source is equal to $(m + \frac{1}{2})\lambda$. Therefore, we will observe an interferogram as presented in Fig. 3.5. Here m is an integer.

In FTIR spectrometer, a polychromatic light source is used, hence we can obtain all the information of all wave numbers at the same time. In this case the interferometer can be shown as in Fig. 3.6 for a two-wavelength light source and a polychromatic

3. EXPERIMENTAL PROCEDURE

light source. Please note that these are for an ideal light sources obtained for the infinite mirror displacement. In reality we can measure the interferogram only for a finite mirror displacement. Therefore, an apodization function will be used beyond the measured displacement.

After an interferometer has been obtained by taking the Fourier transform of this interferometer, we can obtain the power spectrum. Comparing the power spectrum of the sample with that of background gives us the spectrum of the sample in the measured energy range.

3.3 Experimental Details

3.3.1 Fourier Transform Infrared (FTIR) system

In our laboratory, we perform spectroscopic measurements with a Bruker Vertex 80V Fourier transform infrared spectrometer. By utilizing a series of different sources, beamsplitters, and detectors, we can measure an energy range from 20 cm^{-1} to 20000 cm^{-1} . Above this energy region up to $\sim 350000 \text{ cm}^{-1}$, the spectra were measured in UVSOR (Ultraviolet Synchrotron Orbital Radiation) facility, Okazaki, JAPAN. In Fig. 3.7, the relative positions of the used light sources, beamsplitters, and detectors are illustrated with a general view to the FTIR system. The system control and measurements are done with OPUS software program.

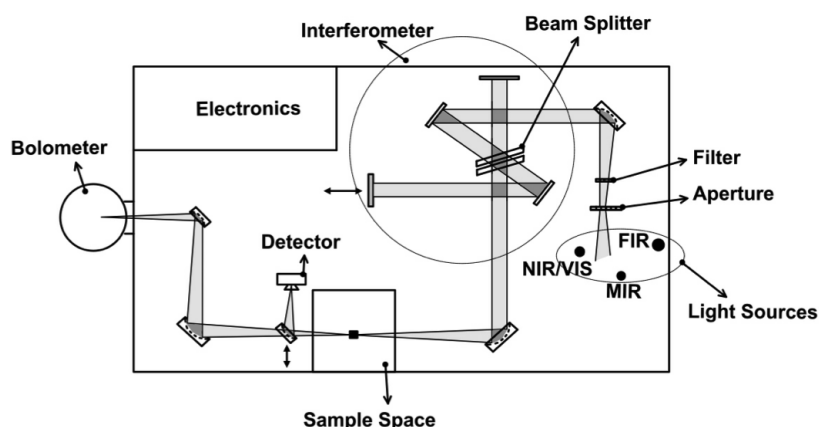


Figure 3.7: Schematic view of Bruker 80V FTIR system - Schematic view of Bruker 80V FTIR system.

3.3 Experimental Details

In this system, the light emitted from one of the sources passes through the aperture and the filter, then sent to the beamsplitter. After the path difference is introduced, it is redirected to the sample space, and finally reaches the detector. In our measurements we use the reflectivity configuration, therefore, the light should be reflected at the sample surface after the beamsplitter. In Fig. 3.8, we plot the schematic picture of the sample space for the reflectivity measurements. We use an external aperture before the sample, to adjust the spot size according to our sample size. Then the reflected light is polarized to perform axis dependent measurements (polarizer information has been given in Table 3.3). Moreover, by using the s -polarization, we eliminate the additional reflection component (in the present case in-plane component). A second aperture cut the window reflections of the cryostat, where the details are given later. In each temperature measurement, we measure a spectrum of a reference mirror, preferably reflective 100% in the chosen energy region as a background to our sample. Then we measure the sample spectrum. During this process, the optical path should be identical for both of the reference mirror and the sample. Therefore, the positions and angles of these two surfaces are checked by a He-Ne laser during the measurement.

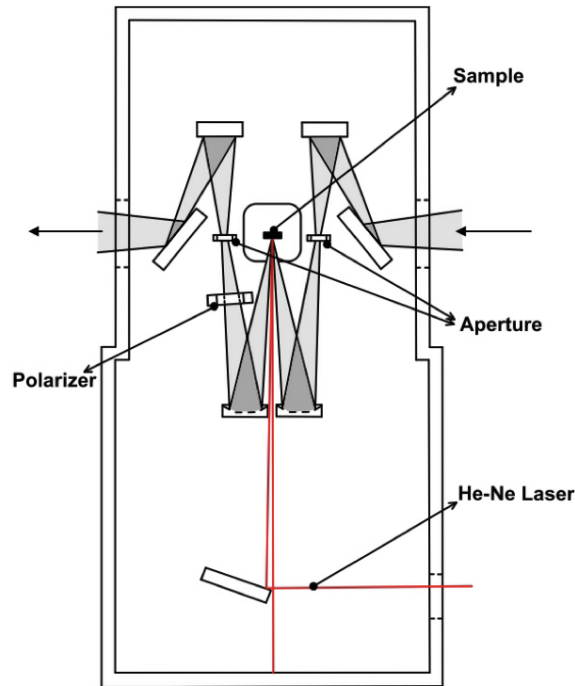


Figure 3.8: Schematic view of sample space - Schematic view of sample space.

3. EXPERIMENTAL PROCEDURE

We perform our measurements in five energy region, where the details are given in Table 3.2. The power spectra of each energy region are shown in Fig. 3.9. The overlapping energy regions in each measurement range allow us to obtain a continuous spectrum over the whole energy range.

Table 3.2: Light sources, detectors, and beamsplitters used in measurements

Region	Measurement range	Light source	Beamsplitter	Detector
Far infrared_1	20 ~ 120 cm^{-1}	Mercury Lamp	Mylar 50 μm	1.7 K Bolometer
Far infrared_2	50 ~ 600 cm^{-1}	Mercury Lamp	Mylar 6 μm	4.2 K Bolometer
Middle infrared	550 ~ 5000 cm^{-1}	Globar Lamp	Ge/KBr	DTGS
Near infrared	3500 ~ 10000 cm^{-1}	Tungsten Lamp	Si/CaF ₂	InGaAs Diode
Visible	9000 ~ 20000 cm^{-1}	Tungsten Lamp	UV/CaF ₂	Silicon Diode

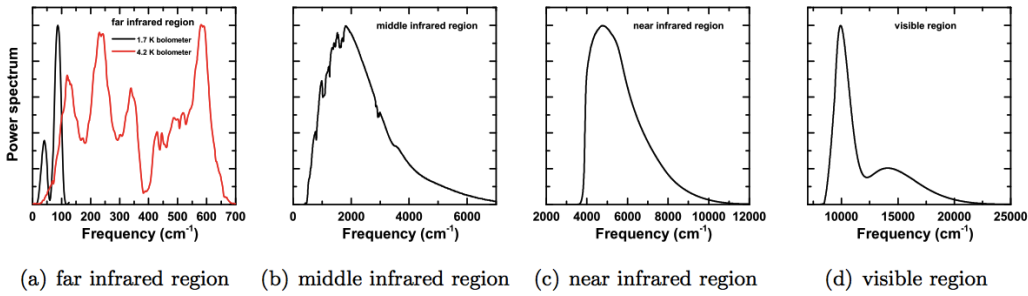


Figure 3.9: Power spectra of the different energy regions used in measurements
- Power spectra of the different energy regions used in measurements. These curves were obtained with 1 cm^{-1} spectral resolution.

3.3.2 Low temperature measurements

The low temperature measurements have been performed in a He-flow cryostat of which the schematic view is given in Fig. 3.10. To avoid the absorption of the environmental gasses, we need to perform our measurements in vacuum. Moreover, to achieve the low temperature measurements, we need a higher vacuum condition that requires to isolate the sample space from the rest of the system. Therefore, we close the system with inner and outer windows. We give the relevant information in Table 3.3. Appropriate windows have been chosen to the measurement range, since the specific windows are transparent only for the specific energy ranges. Some of the windows, like the

3.3 Experimental Details

quartz ones, are crystal quartz window. Therefore, even though they transmit the light with high efficiency, they also reflect some portion. Moreover, we also observe multiple reflections between samples and the windows, as well. These might affect the spectrum greatly in some conditions; therefore, we cut these reflections by using a second aperture.

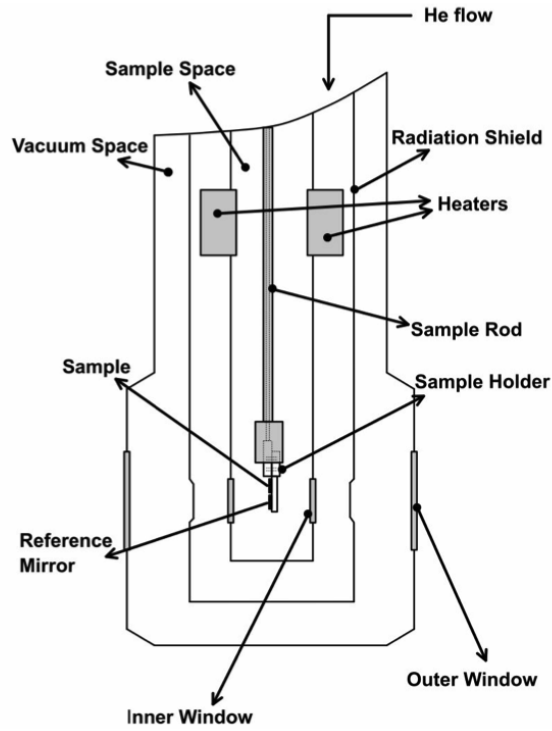


Figure 3.10: Schematic view of the cryostat - Schematic view of the cryostat.

Table 3.3: Windows and polarizers used in measurements

Region	Inner windows	Outer windows	Polarizer
Far infrared_1	polypropylene	polypropylene	polyethylene wire grid
Far infrared_2	polypropylene	polypropylene	polyethylene wire grid
Middle infrared	Zn-Se	KBr	KRS-250 wire grid
Near infrared	quartz	quartz	Glan-Taylor prism
Visible	quartz	quartz	Glan-Taylor prism

3. EXPERIMENTAL PROCEDURE

3.3.3 Reflectivity measurements

The reflectivity measurements are performed in five different energy regions from 20 cm^{-1} to 20000 cm^{-1} . Measurements at each temperature are performed with 256-512 scans. Moreover, measurement at each temperature is repeated several times (3-5 times). The repetition of the measurements at each energy region allows us to specify an error bar in this energy range. Moreover, we can also define another error bar in the overlapped energy regions for different measurement ranges. The overall error in the reflectivity is chosen as the highest error calculated in the measurements (from the repetition of the same energy range or from the overlapped regions). The error bars are calculated with the same way for each temperature separately. As a result, the maximum error in our reflectivity measurements is better than 0.4%. In Fig. 3.11, the spectra measured for each energy region and the overlapped part for the different energy regions are given for a chosen sample as an example. Errors in measurements are determined with the spectral weight calculations of the used range of the spectra. The regions for which the spectral weights are calculated were shown with the vertical lines and the calculated errors for each spectrum is given on the corresponding graph as percentage.

The optical conductivity spectra are determined with the Kramers-Kronig transformations from the measured reflectivity spectra, where the formalizations are given in the next section. Errors in the optical conductivities (real and imaginary) and superfluid densities are determined with the recalculations from the reflectivity spectra after the errors are included. One of the recalculated spectra for the real and imaginary optical conductivity, as well as the superfluid density is given in Fig. 3.12. In the next chapter, the temperature dependence of the superfluid densities is given with the error bars in Fig. 4.21. As can be seen from the figures, the errors on the calculated superfluid densities have no effect on the obtained temperature scales.

3.4 Optical relations

The interaction of electromagnetic radiation with matter is based on the calculations that are derived from Maxwell's equations. The interaction of the material with light can be defined with response functions. Complex dielectric function $\hat{\epsilon}$ and complex conductivity $\hat{\sigma}$ can be taken into account as the prime response functions that describe

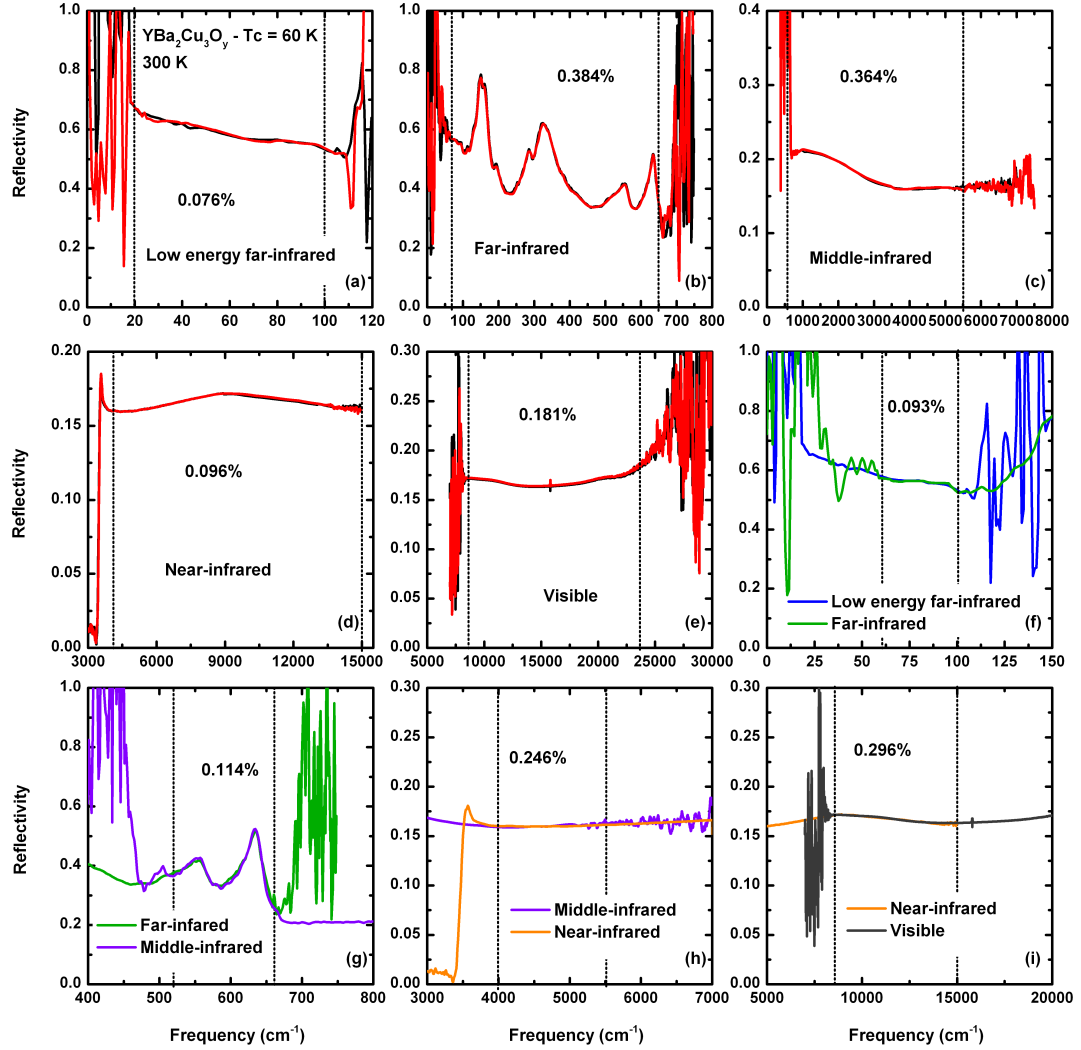


Figure 3.11: Determination of the errors in the reflectivity measurements - The errors in each energy scales had been determined from the spectral weight difference of the repeated measurement in the same energy range (a-e). The error of the connection of the different energy scales are also determined from the spectral weight difference between the different energy scales that is calculated for the overlapped energy region of the spectra (f-i). The dotted lines are the limits where the spectral weight calculations had been done. These regions show the reliable part for the each energy region.

3. EXPERIMENTAL PROCEDURE

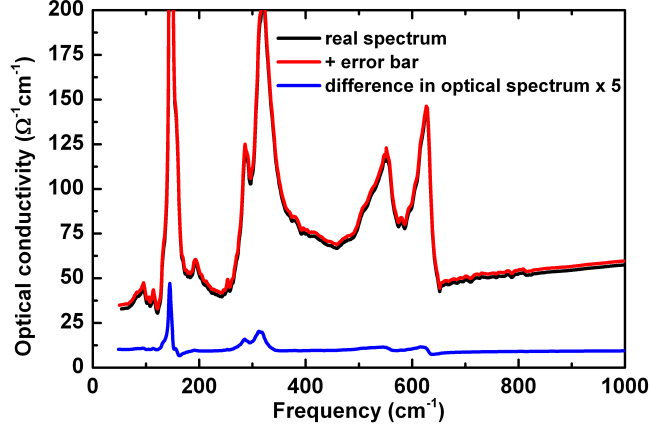


Figure 3.12: Determination of the error in optical conductivity - Optical conductivity has been determined from the reflectivity measurements with Kramers-Kronig transformation. After the calculated error bar is added to the reflectivity, the optical conductivity recalculated with the same method. And the difference between two calculations are determined as the error on the optical conductivity.

the response to the applied electric field. These response functions contain both dissipation (real part) and phase (imaginary part) information. The general considerations that can be used to derive important relations between these real and imaginary parts of the response functions are given by Kramers and Krönig [68, 69]. These are called Kramers-Krönig relations (KK relations). It is possible to set series of relations between the real and the imaginary parts of the several response functions. For instance these relations for the complex dielectric function can be given as Eqs. 3.2, 3.3, 3.4:

$$\hat{\epsilon}(\omega) = \epsilon_1(\omega) + i\epsilon_2(\omega) \quad (3.2)$$

$$\epsilon_1(\omega) - 1 = \frac{2}{\pi} \mathcal{P} \int_0^\infty \frac{\omega' \epsilon_2(\omega')}{\omega'^2 - \omega^2} d\omega' \quad (3.3)$$

$$\epsilon_2(\omega) = -\frac{2\omega}{\pi} \mathcal{P} \int_0^\infty \frac{\epsilon_1(\omega')}{\omega'^2 - \omega^2} d\omega' \quad (3.4)$$

Usually the normal-incidence reflectivity $R(\omega)$ spectra are obtained experimentally and the real and the imaginary parts of the complex dielectric function are calculated

from this reflectivity value. Both $\epsilon_1(\omega)$ and $\epsilon_2(\omega)$ depend to an unknown phase of the complex reflectivity $\hat{r}(\omega)$ (Eq. 3.5).

$$\hat{r}(\omega) = \frac{1 - \sqrt{\hat{\epsilon}(\omega)}}{1 + \sqrt{\hat{\epsilon}(\omega)}} = \sqrt{R(\omega)} \exp(i\theta(\omega)) \quad (3.5)$$

Here $\theta(\omega)$ is the phase, in other words the imaginary part of the complex reflectivity, while $R(\omega)$ is the real part of the complex reflectivity response function. $R(\omega)$ is experimentally measured, and we can calculate the phase with KK relations as Eq. 3.6.

$$\theta(\omega) = -\frac{2\omega}{\pi} \mathcal{P} \int_0^\infty \frac{\ln \sqrt{R(\omega')}}{\omega'^2 - \omega^2} d\omega' + \theta(0) \quad (3.6)$$

Once we have the real and imaginary components of the complex reflectivity function, we can obtain the complex dielectric function and its components, as well, by using the Eq. 3.5.

Moreover, we can obtain the complex optical conductivity and its components, as well, by using the equations 3.7 and 3.8.

$$\sigma_1(\omega) = \frac{\omega \epsilon_2(\omega)}{4\pi} \quad (3.7)$$

$$\sigma_2(\omega) = \frac{(1 - \epsilon_1(\omega))\omega}{4\pi} \quad (3.8)$$

3.5 Fitting of the Reflectivity Spectra

As can be seen from the KK relations, these relations require data set from zero frequency up to infinity. Such kind of measurement is not possible in reality. Therefore, we need to consider some extrapolations beyond our measurement limits. These extrapolations can be chosen in different ways depending on the measurement sample. As mentioned previously, *c*-axis optical spectra of the cuprates are dominated by phonon modes. Therefore, in the normal state, Lorentz oscillators (for phonon modes) and a Drude component (for the weak electronic background) had been used to fit our experimental data (Dielectric function given in Eq. 3.9). In the superconducting state, instead of Drude, two-fluid fitting with Lorentz oscillators was chosen (Dielectric function given in Eq. 3.10). The fitting results were used as the low energy extrapolations

3. EXPERIMENTAL PROCEDURE

(Below 20 cm^{-1}). At high energy region (above 40 eV) free carrier approximation had been used as an extrapolation ($R(\omega) \propto \omega^{-4}$). Low energy fittings are shown in Fig. 3.13.

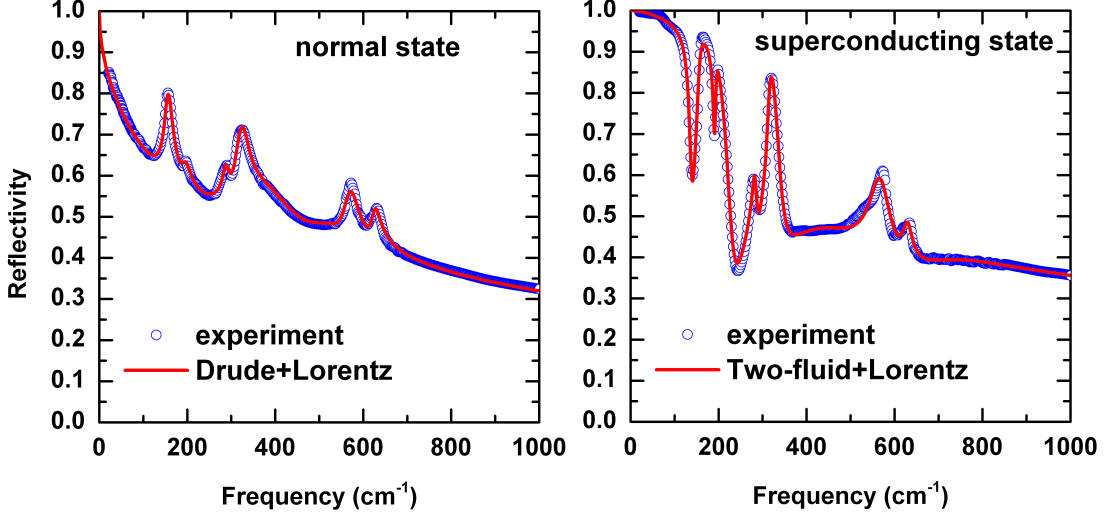


Figure 3.13: Low energy fitting of the reflectivity used for extrapolations - Low energy fitting of the reflectivity used for extrapolations.

$$\hat{\epsilon}(\omega) = \epsilon_{\infty} - \frac{\omega_{p,Drude}^2}{\omega^2 - i\omega\Gamma_{Drude}} + \sum_j \frac{\omega_{p,j}^2}{\omega_{0,j}^2 - \omega^2 - i\omega\Gamma_j} \quad (3.9)$$

Here ω_p is the plasma frequency that can be defined as $\omega_p^2 = ne^2/\epsilon_0m$. Γ is the damping term. $\omega_{0,j}$ is the resonance frequency of the phonon oscillators.

$$\hat{\epsilon}(\omega) = \epsilon_{\infty} - f_s \frac{\omega_p^2}{\omega^2} - f_n \frac{\omega_p^2}{\omega^2 + i\omega\Gamma_n} + \sum_j \frac{\omega_{p,j}^2}{\omega_{0,j}^2 - \omega^2 - i\omega\Gamma_j} \quad (3.10)$$

Here f_s and f_n are the superconducting and normal carrier volume fractions, respectively. $f_s + f_n = 1$

The extrapolation values of the optical conductivity to the zero frequencies also confirm that our fittings are reasonable. dc conductivity values can be compared directly with the dc resistivity values ($1/\rho_{dc} = \sigma_{dc}$). In Fig. 3.14, the dc resistivity values obtained with the extrapolations of our $\sigma_1(\omega)$ to the zero frequencies are given for the Zn-free samples (symbols) for several doping levels. The dc resistivity curves are also plotted for some of the samples. We chose the resistivity curves of the samples, which

3.5 Fitting of the Reflectivity Spectra

have the closest T_c to our samples; nonetheless, there might be 2-3 K T_c differences between the resistivity curves and our samples. The T_c of the optimally doped sample is the only one that exactly matches to our sample. In the lower doping regions, the physical properties of the system changes rapidly, but, be that as it may, our extrapolation values show a reasonable agreement with the dc resistivity measurements. Moreover, our extrapolation values show a gradual change with doping.

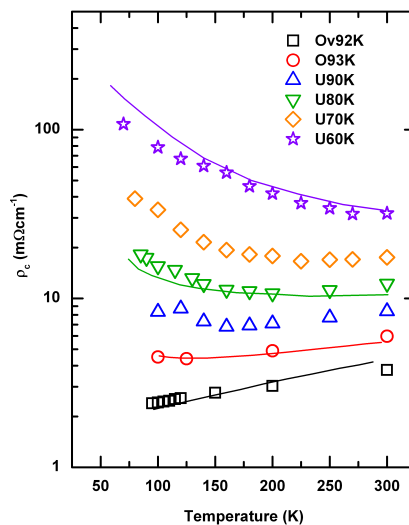


Figure 3.14: Comparison of the dc resistivity data with the optical conductivity extrapolations - Comparison of the dc resistivity data with the optical conductivity extrapolations to the zero frequency. Resistivity data are taken from [34]. There might be 2-3 K T_c differences between samples used in this study and the samples that the resistivity data belong to.

With Zn-substitution, although the in-plane resistivity and the residual resistivity are gradually increasing, it has been shown that the c -axis resistivity does not change significantly. In Fig. 3.15, a comparison of the in-plane and c -axis resistivity as a function of Zn-content is shown [70]. Other groups also report similar Zn-insensitive behavior along the c -axis direction for lower doping region [56]. In Fig. 3.16, we plotted the extrapolation values of the optical conductivity to the zero frequency for several doping levels for several doping levels.

3. EXPERIMENTAL PROCEDURE

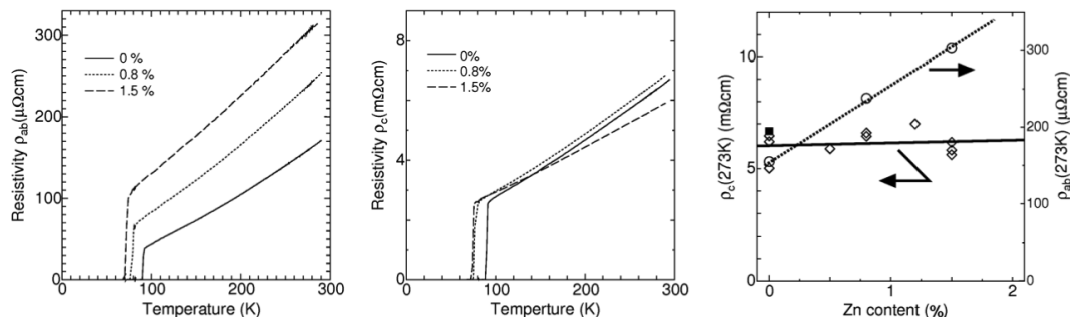


Figure 3.15: Zn-substitution effect on in-plane and c -axis resistivity - Zn-substitution effect on in-plane (a) and c -axis (b) resistivity. (c) shows the absolute values of the resistivity at 273 K as a function of the Zn-content for in-plane and c -axis resistivity [70].

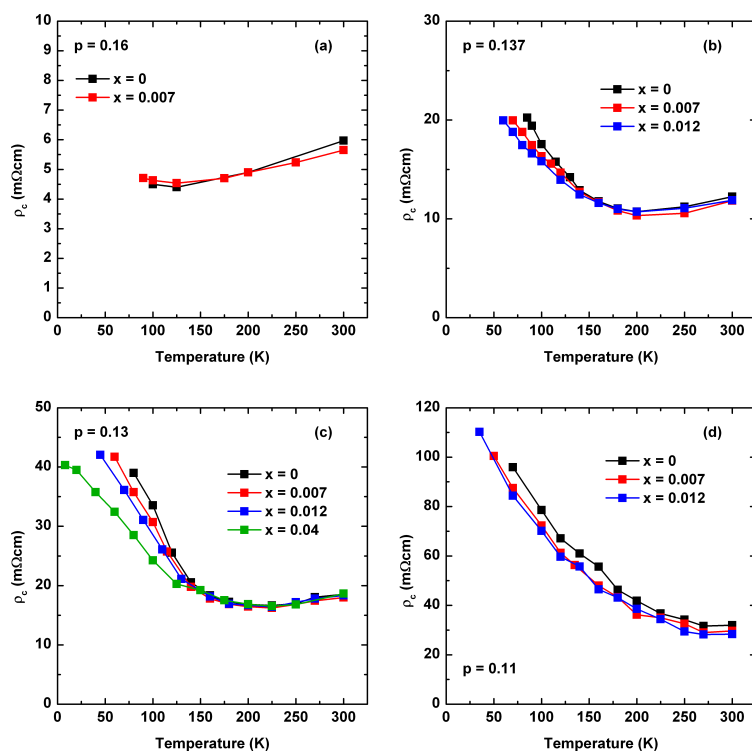


Figure 3.16: c -axis resistivity obtained from the extrapolation of the optical conductivity - Doping and Zn-dependence of the c -axis resistivity obtained from the extrapolation of the optical conductivity.

4

Results and discussion

4.1 $E//c$ -axis Optical Measurements

YBa₂Cu₃O_{*y*} system is one of the cuprate families, where significant amounts of study on the *c*-axis properties were presented. In this study, we extend the energy region (both lower and higher energy region), and decrease the temperature steps for measurement, therefore, we could make a more precise discussion on the observed properties. In this section, I will give some general insight to the observed optical properties of YBa₂Cu₃O_{*y*} and Zn-substitution effects with the comparison to the other studies. In the later sections, more detailed discussion on the observed properties with new observations will be given.

4.1.1 Doping dependent optical spectra of YBa₂Cu₃O_{*y*}

Overall features

As mentioned previously, YBa₂Cu₃O_{*y*} has relatively higher conductivity along *c*-axis than the other cuprate families. In Fig. 4.1(a) the room temperature reflectivity spectra up to UV energy region are presented for several doping regions. In the optimally doped regime, the electronic component can be clearly seen as the continuous increase towards the zero frequency (Drude component), even though the spectrum is dominated by the phonon modes. With decreasing doping the electronic component is getting weaker.

4. RESULTS AND DISCUSSION

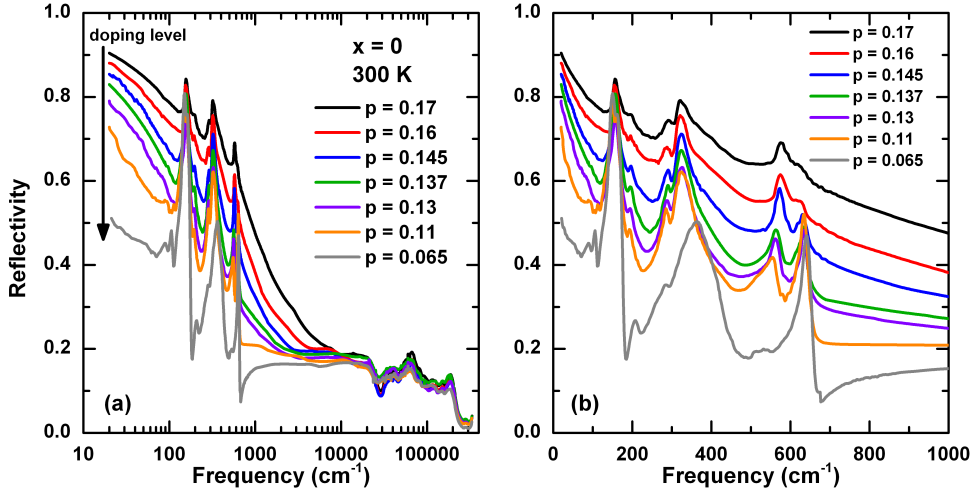


Figure 4.1: Doping dependent room temperature reflectivity of YBa₂Cu₃O_y - Doping dependence of the room temperature reflectivity of YBa₂Cu₃O_y. (a) The reflectivity spectra for three chosen doping level is shown up to high energy region. Weakening of the Drude component can be seen. (b) Low energy spectra is shown for all doping levels. Phonon modes can be seen clearly. The evolution of the apical oxygen modes also can be seen as a function of doping.

Phonons

As reported in previous studies [71], we can observe five main phonon modes in the optical spectrum in the overdoped region. The lowest phonon mode around 150 cm⁻¹ is ascribed to the out of phase displacement of the Ba to the in-plane Cu and the vibration of the Ba against the chain Cu. With decreasing doping level, this mode splits and it is possible to see these two more clearly. This splitting occurs due to the two inequivalent Ba-sites with and without the chain site oxygen. The phonon mode around 200 cm⁻¹ is due to the Y vibrations. The phonon modes around 280 and 320 cm⁻¹ are described as the in-plane oxygen bending mode. With decreasing doping these phonon modes also merge and shift to a little higher energy region due to the orthorhombic to tetragonal phase transition in the low doping region. The 320 cm⁻¹ phonon mode has been discussed in terms of anomalies. Other phonon modes do not show very significant changes with temperature, except the sharpening with decreasing temperature as expected. On the other hand, this phonon mode is significantly reconstructed with temperature, especially in the superconducting state. The last phonon modes around 550 and 620 cm⁻¹ are due to the apical oxygen modes.

In high doping region we only see the low energy mode in a very strong way, while in the low doping region, the low energy phonon mode disappears and the higher energy phonon mode becomes stronger. In the intermediate doping levels, we observe both phonon modes, the relative intensities are changing, depending on the doping level. In Fig. 4.1(b), the doping dependence of these phonon modes can be seen. The splitting of this phonon mode is due to the motion of the apical oxygen between the in-plane Cu and chain Cu sites. Two frequencies for the apical oxygen mode imply the presence of two environments, namely, with and without the chain-site oxygen. Moreover, the intensity ratios of these phonon modes strongly depend on the oxygen concentration in the system. Therefore, these two phonon modes can be a good measure in our measurement to see that the doping levels of the Zn-free and Zn-substituted samples are the same or not. Since Zn-substitution does not alter the oxygen concentration, we expect these phonon modes to be similar in both Zn-free and Zn-substituted samples.

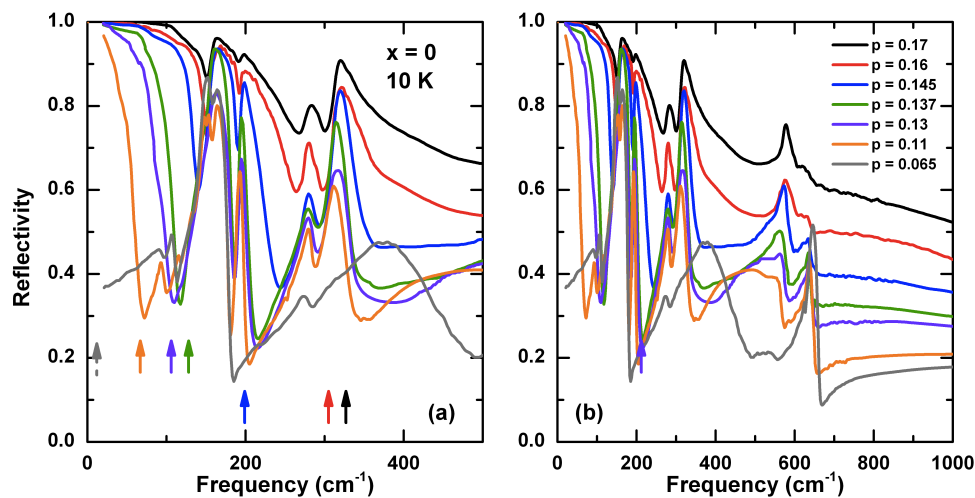


Figure 4.2: Doping dependent reflectivity of $\text{YBa}_2\text{Cu}_3\text{O}_y$ in the superconducting state - Doping dependence of the low energy reflectivity of $\text{YBa}_2\text{Cu}_3\text{O}_y$ at 10 K. (a) Arrows represent the Josephson plasma edge. These values had been obtained with the two fluid fittings of the reflectivity. (b) Focus on the TJP mode region

Josephson plasma

When the system becomes superconducting, the reflectivity spectra show significant changes (Fig. 4.2(a)). First of all in the low energy region, we start to observe

4. RESULTS AND DISCUSSION

the Josephson plasma resonance. This is due to the collective motion of the superconducting carriers and does not give any feature to the optical conductivity, indicating that this is not a superconducting gap. The Josephson plasma frequency is closely related to the superconducting carrier concentration with the following relation: $\omega_{ps,screened} = \omega_{ps}/\sqrt{\epsilon_\infty}$. Here ω_{ps}^2 is proportional to the superfluid density (n_s). $\omega_{ps,screened}$ is the frequency of the Josephson plasma edge. With decreasing doping level, the edge shifts to the lower energy region, indicating the decrease of superconducting carrier concentration. Superfluid density of this system had been calculated by several groups. In Fig. 4.4 we compare our results with previously published data [56]. Our results show an excellent agreement with the previous results. During our calculations, ϵ_∞ was determined by the fitting of the reflectivity spectrum as 22.

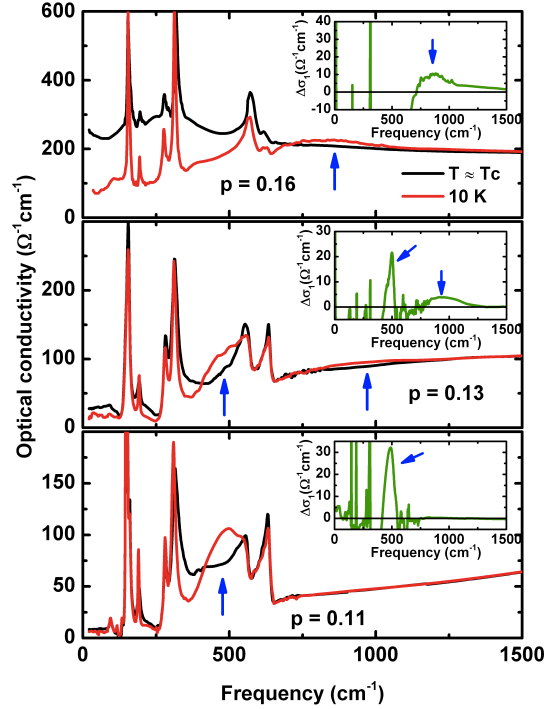


Figure 4.3: Doping dependent transverse Josephson plasma mode - Doping dependence of the transverse Josephson plasma mode of $\text{YBa}_2\text{Cu}_3\text{O}_y$. Insets show the difference spectra of the same plots. Arrows indicate the TJP mode. The shift of the mode and the splitting can be seen.

Transverse Josephson plasma

Another important feature in the superconducting state spectrum is the broad absorption around $400 - 500 \text{ cm}^{-1}$ (Fig. 4.2(b)). This structure has been attributed to the transverse Josephson plasma (TJP) resonance. It is easier to see the behavior of this mode in the optical conductivity. At high doping region, this mode starts to appear at high energies, and gradually shifts to the low energy region. Moreover, in the existence of the phonon modes, it splits. In Fig. 4.3, the doping dependence of the TJP mode is plotted.

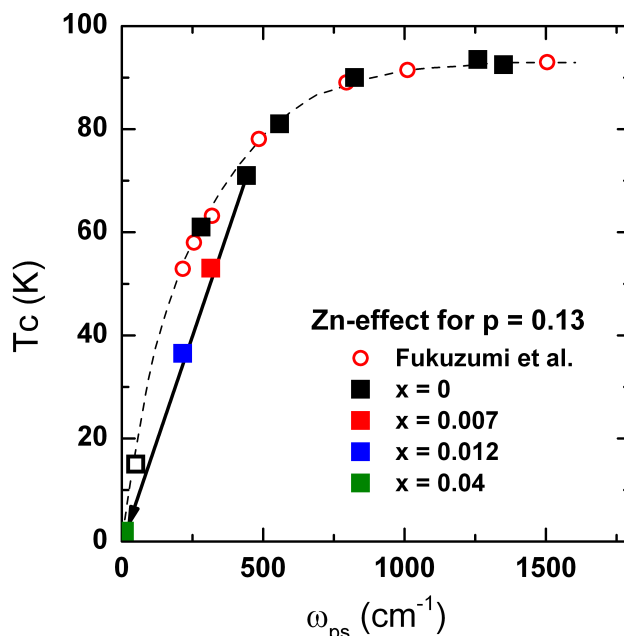


Figure 4.4: Doping dependence of the Josephson plasma frequency of $\text{YBa}_2\text{Cu}_3\text{O}_y$ - Doping dependence of the Josephson plasma frequency of $\text{YBa}_2\text{Cu}_3\text{O}_y$ is given with the published data by Fukuzumi *et al.* [56]. Datum for the lowest T_c sample (open square) is the expected value based on the dashed line plotted on this graph. These data shows that our fittings are reasonable and reproduced. Zn-dependence of the $p = 0.13$ is also plotted here. The shift of the JP edge to zero frequency with Zn-susbtitution can be seen. Please note that for this doping level $x = 0.04$ is not superconducting.

Furthermore, with the appearance of this mode, we also observe the softening of the oxygen bending mode. It was also shown that the TJP mode starts to appear at higher temperatures than T_c [52, 72]. Then, it was proposed that the appearance of the TJP

4. RESULTS AND DISCUSSION

mode is the precursor of the superconductivity. However, it is difficult to observe this mode directly from the optical conductivity above T_c since the contribution is very weak. However, the softening of the oxygen bending mode is very clear. Therefore, it is a suitable way to trace the softening of this phonon mode to see the temperature dependence of the TJP resonance. In Fig. 4.5 we presented the doping dependence of the frequency of the oxygen bending mode. These frequencies were obtained from the raw reflectivity data. It can be seen that the decrease of the phonon frequency (namely the softening) starts to appear at high temperatures, compared to T_c . Moreover, the temperature that we start to see the softening also shifts to the higher temperatures with decreasing doping level. These results are consistent with the previously presented results [72].

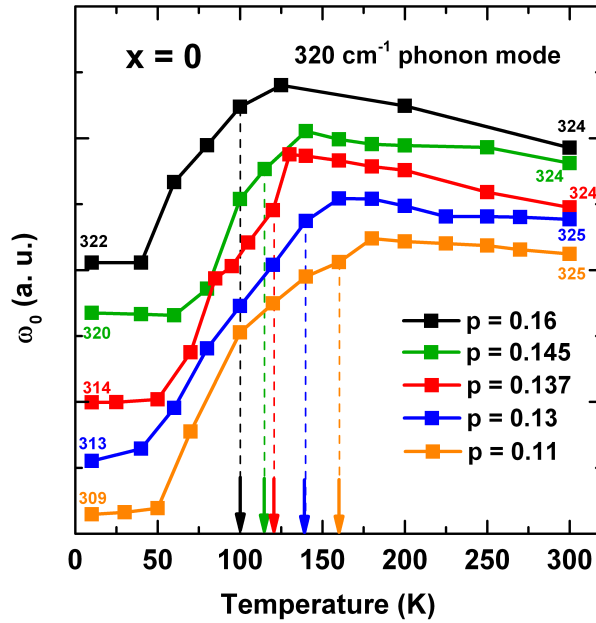


Figure 4.5: Doping dependence of the oxygen bending mode in $\text{YBa}_2\text{Cu}_3\text{O}_y$ - Doping dependence of the 320 cm^{-1} phonon mode for $\text{YBa}_2\text{Cu}_3\text{O}_y$. Plots had been shifted to show all the doping levels on the same plot. The arrows show the temperature that the softening started. This is associated with the appearance of the TJP mode.

4.1.2 Zn-substitution effects on optical response

So far we presented the general remarks on the c -axis optical study of the $\text{YBa}_2\text{Cu}_3\text{O}_y$ system. In this part we will discuss the general properties of the Zn-substituted systems. Zn is a well known non-magnetic impurity that causes pair breaking in the system, hence suppresses the superconductivity. The effects of Zn-substitution on the superconductivity have been investigated by many experimental probes. In optical spectrum we also see very clear effects of the Zn-substitution.

When we compare the spectra at room temperature for the Zn-free and the Zn-substituted samples, we observe that the spectrum does not change significantly. In Fig. 4.6, the room temperature reflectivity and optical conductivity spectra are shown for $p = 0.13$. We cannot observe any significant difference with Zn-substitution. Moreover, the apical oxygen phonon modes are similar in all the Zn-free and Zn-substituted samples, indicating that the samples have the same oxygen concentration; hence they are in the same doping region.

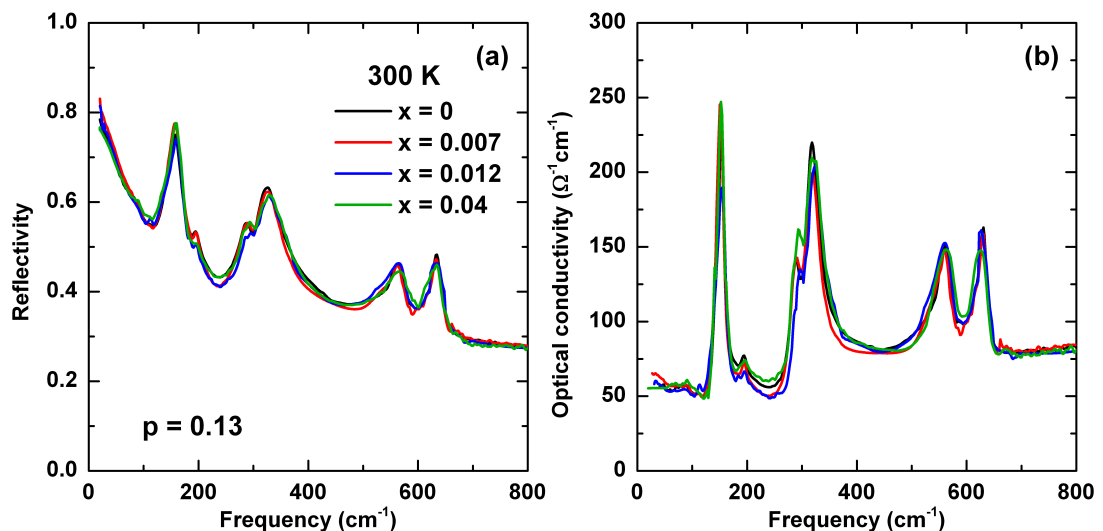


Figure 4.6: Zn-concentration dependence of the room temperature optical spectra - Zn-concentration dependence of the room temperature reflectivity and optical conductivity at $p = 0.13$. There is no significant difference with Zn substitution.

In the superconducting state, the effect of Zn-substitution is prominent (Fig. 4.7). In the low energy region, we observe the shift of the Josephson plasma edge to the low energy region with increasing Zn-content. This behavior indicates the decrease of the

4. RESULTS AND DISCUSSION

superfluid density with increasing doping level. This is expected since Zn-impurities act as pair breakers and suppresses the superconductivity. The Zn-doping effect on the superfluid density is also demonstrated in Fig. 4.4. Although Zn-doping effect is demonstrated for one doping level, similar results were observed for the other doping regions, as well.

Another Zn-doping effect happens on the TJP mode. This mode is also suppressed with increasing Zn-content, and for 1.2% Zn-doped sample, it disappears. We used this behavior to study the pseudogap region, because it is easier to see the small conductivity changes in the absence of the complications of this TJP mode. In the next section the pseudogap region will be discussed.

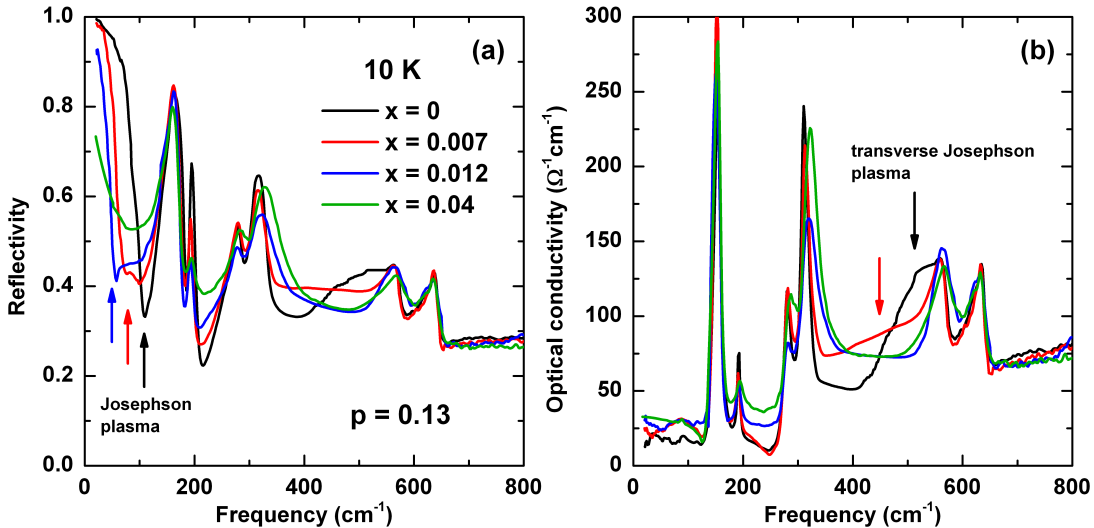


Figure 4.7: Zn-concentration dependence of the optical spectra in the superconducting region - Zn-dependence of the reflectivity and optical conductivity at 10 K for $p = 0.13$. Shift of the JP edge to the low energies (reflectivity spectra) and the disappearance of the TJP mode (easier to see in optical conductivity) with increasing Zn-content can be seen. Features are indicated with arrows.

4.2 Discussion on Pseudogap

4.2.1 Pseudogap in the underdoped region

$E//c$ -axis optical study is one of the powerful tools to study the pseudogap behavior in cuprates. Pseudogap behavior dominates the antinodal region of the Fermi sur-

face. This behavior has been intensively discussed by the experimental probes that can perform momentum resolved measurements, such as Angle Resolved Photoemission Spectroscopy and Raman Spectra. $E//c$ -axis optical conductivity is not a momentum resolved measurement. However, it has been shown that the interlayer tunneling matrix element is one of the key parameters to describe the conduction along the c -axis, and it is strongly momentum dependent [73, 74]. Owing to the two dimensional crystallographic properties, this matrix element is basically defined by the antinodal region of the Fermi surface [75]. Even though the c -axis properties reflect the average over the Fermi surface, this is a weighted average in favor of the antinodal region.

With the pseudogap opening in the antinodal region, we can observe the suppression of the low energy c -axis optical conductivity, which is restored in the high energy regions. On the other hand, the pseudogap effect on the in-plane spectra is mainly Drude narrowing, namely, the reduction in scattering rate, which results in the spectral weight transfer to lower energy regions. Since we cannot measure a spectrum down to $\omega = 0$ (20 cm^{-1} is the low- ω limit in our case), it is hard to judge whether the observed suppression of the low energy in-plane conductivity is due to the pseudogap or to the superconducting gap. By contrast, for the case of the c -axis spectra, we can easily distinguish the effects of the superconducting gap and the pseudogap, because the direction of the spectral weight (SW) transfer is opposite in the two gaps. In Fig. 4.8 the clear behavior of the pseudogap is demonstrated.

The more clear behavior of the pseudogap can be seen by tracing the SW over the energy region for each temperature. In Fig. 4.9, we plot the calculated SW for three energy regions for several doping levels. The first is the low energy region, where we can see the suppression of the low energy optical conductivity due to the pseudogap opening ($50\text{-}800 \text{ cm}^{-1}$). The second is the high energy region, where the SW is gained with the pseudogap opening ($800\text{-}5000 \text{ cm}^{-1}$). And the third region is the overall energy region, where we can confirm the SW transfer occurs due to the pseudogap ($50\text{-}5000 \text{ cm}^{-1}$). In all energy regions, SW is calculated by using the Eq. 4.1. Here 'a' and 'b' represent the energy region that we calculated the SW.

$$SW_a^b = \int_a^b \sigma_{1,c}(\omega) d\omega \quad (4.1)$$

In the low energy region ($50 - 800 \text{ cm}^{-1}$), especially at high doping levels, the SW increases with lowering T above T^* , which reflects a metallic behavior of the system.

4. RESULTS AND DISCUSSION

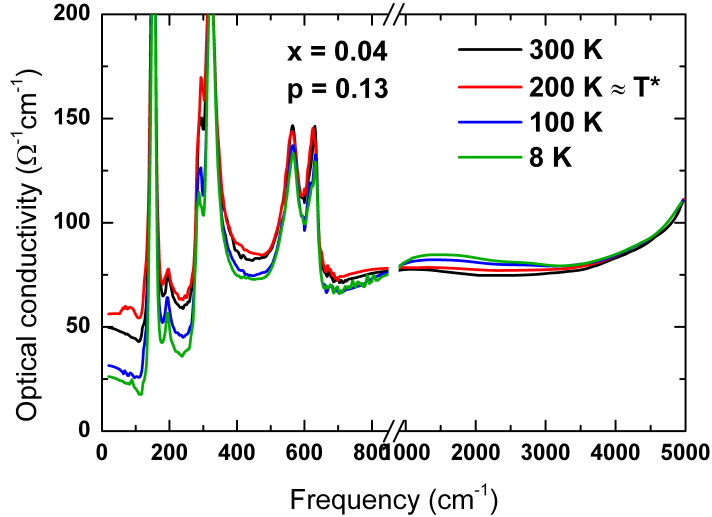


Figure 4.8: Pseudogap behavior in the optical conductivity - Temperature dependent optical conductivity of the sample with $x = 0.04$ at $p = 0.13$. In this doping region this sample is non-superconducting, however, present a clear pseudogap behavior. The lost SW at the low energy region (left panel) is transferred to the high energy region (right panel) below T^* , hence a crossover can be seen.

At the temperatures where the pseudogap opens, the increase stops and below this temperature we observe continuous decrease of the SW. This decrease continues below T_c due to the superconducting gap opening. The turning point of the SW can be defined as the pseudogap temperature. This point gradually decreases with increasing doping level (shown in Fig. 4.10), which is consistent with the pseudogap behavior presented by several other probes in Fig. 4.11 [76, 77].

The SW that is lost in the low energy region should be transferred to the high energy region ($800 - 5000 \text{ cm}^{-1}$) with pseudogap opening. This behavior indeed has been observed in the high energy spectral weight (Fig. 4.9). Again at high doping region, at high temperatures we observe the increase of the SW due to the metallic behavior of the system with an over-damped Drude response, marked with grey background (Please note that this region expands with increasing doping). With pseudogap opening, on the other hand, we observe an increase due to pseudogap with a step-like anomaly. With further decreasing temperature, we observe that the increase of the SW due to pseudogap is interrupted by the superconducting condensation. However, the SW that is transferred to the high energy region with pseudogap opening, does not show any

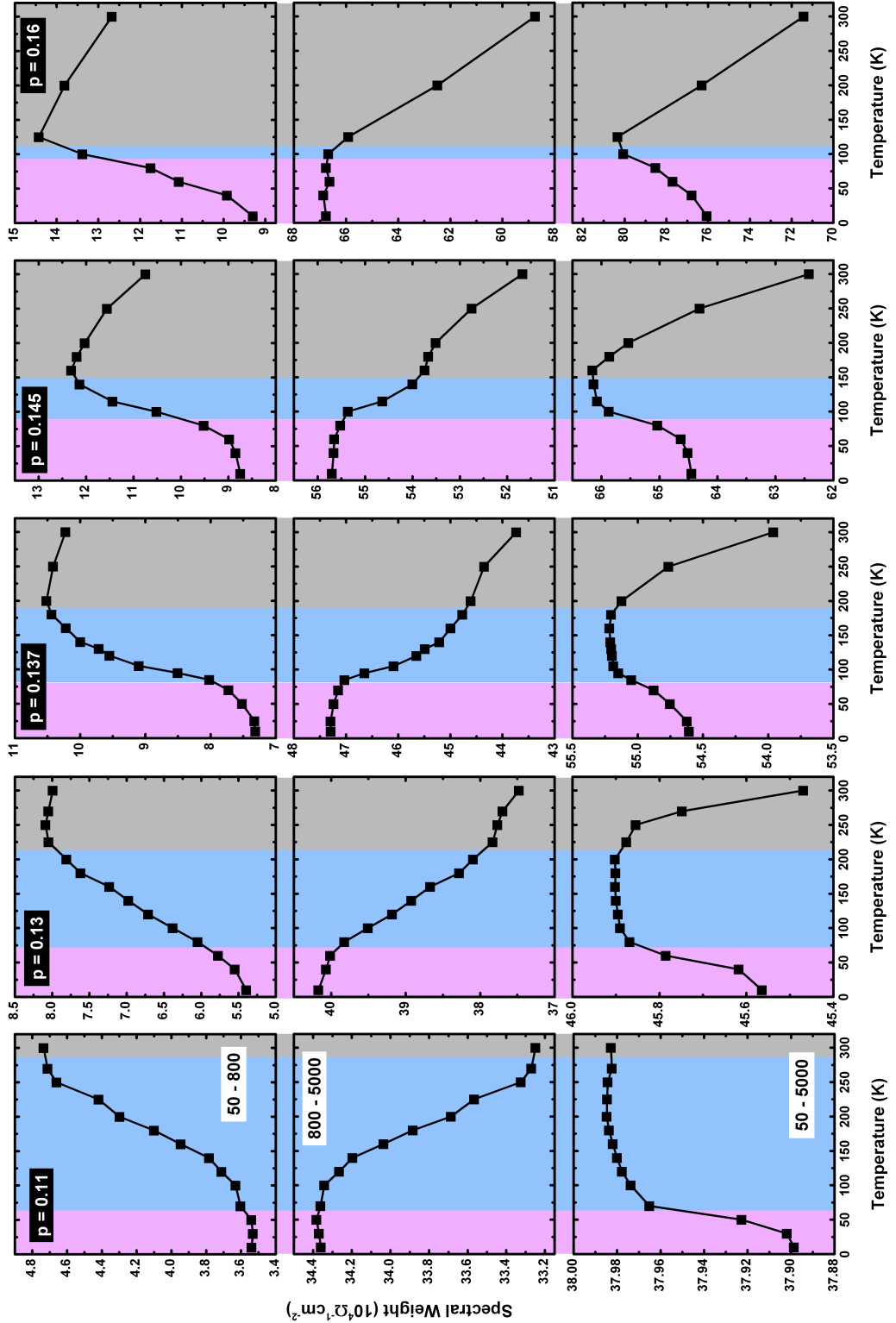


Figure 4.9: Energy region dependence of the spectral weight - Spectral weight in specific energy regions for $p = 0.11$ to $p = 0.16$. The temperature region where we see the weak metallic behavior of the system expands with increasing doping (grey backgrounds). Moreover, the blue area indicates the region where the sum-rule holds below 5000 cm^{-1} . With superconducting transition we observe a missing area in the overall spectral weight as indicated with the red background.

4. RESULTS AND DISCUSSION

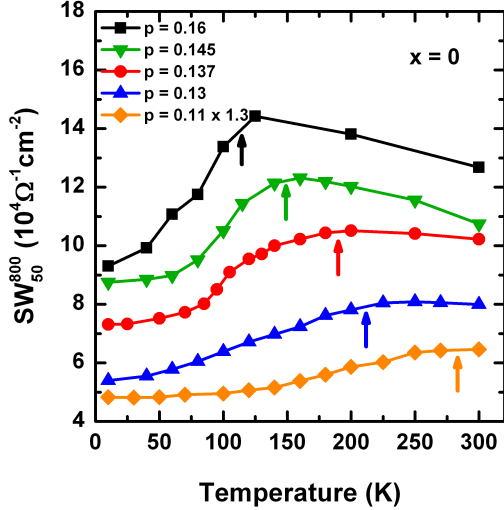


Figure 4.10: Doping dependence of the low energy SW for $\text{YBa}_2\text{Cu}_3\text{O}_y$. The suppression of the low energy SW clearly shows the pseudogap behavior.

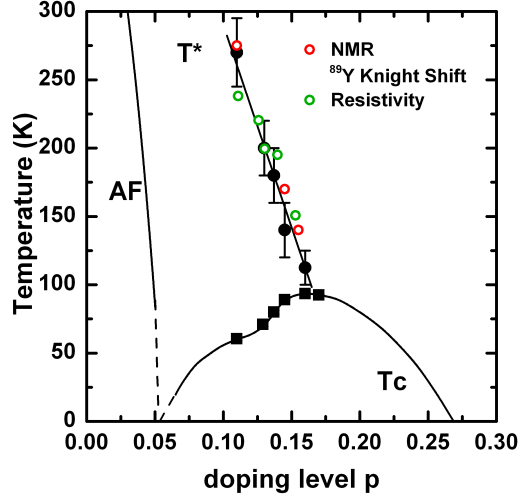


Figure 4.11: Doping dependence of the obtained T^* as a comparison to other methods. NMR Knight shift: [76] and Resistivity [77].

decreasing behavior below T_c . This suggests that the pseudogap does not contribute to the superconducting condensation. Therefore, we can suggest that the pseudogap is not a precursor of superconductivity. For high doping samples, we observe an increasing behavior of the high energy SW below T_c . However, this increase is not due to the pseudogap but it is an artifact of the TJP mode that we can see as an absorption at the high energy region. This may mislead the discussion; therefore, the suppression of this mode is necessary.

In the energy region when the spectral weight transfer due to the pseudogap opening is completed, SW is expected to be conserved. Our calculations showed that the 5000 cm^{-1} is this energy region. Therefore, the SW in the overall energy region ($50 - 5000 \text{ cm}^{-1}$) should be conserved in the case of the pseudogap opening. In the superconducting state, on the other hand, we should see a missing SW because the superconducting carriers are condensed to the δ -function at zero frequency, which causes a missing area in the optical conductivity spectrum. As can be seen in Fig. 4.9, the overall spectral weight is conserved below pseudogap temperature (marked with blue background). Below T_c we can clearly observe the behavior of the superconducting condensation (marked with red background). Change above T^* is due to the metallic response of

the system.

We also performed the same calculations for the Zn-substituted samples. Zn-substitution suppresses the TJP mode, therefore, we can give more precise discussions about the pseudogap behavior especially in the superconducting regime. The Zn-doping dependence of the low energy SW is given in Fig. 4.12. The overall behavior does not change significantly with Zn-substitution. Moreover, the pseudogap temperature does not change with Zn-doping.

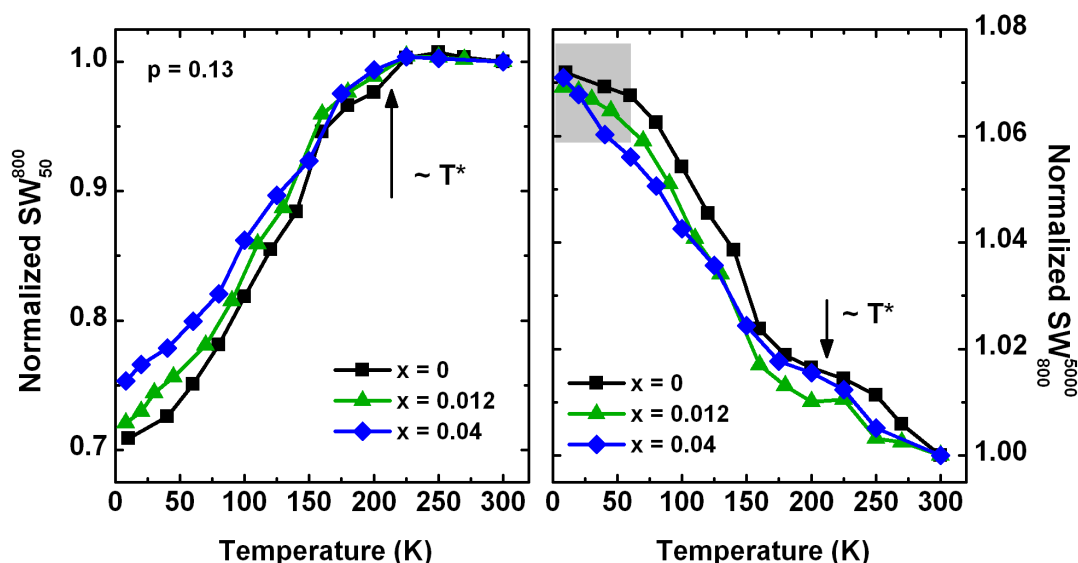


Figure 4.12: Zn-doping dependence of the low and high energy SW - Zn-dependence of the low (left panel) and high (right panel) energy SW. Low energy part shows that T^* does not change with Zn doping. Below T_c the high energy transfer continues for the Zn-substituted samples.

For the high energy SW, on the other hand, we can observe some differences below T_c with Zn-substitution. As shown in Fig. 4.12, when Zn is substituted, the increase of the SW with pseudogap opening continues even below T_c (Grey shaded area in the figure). This behavior observed for the Zn-free sample cannot be attributed to the pseudogap solely due to the TJP mode; however, please note that the TJP mode is suppressed with Zn-substitution. Therefore, the increase below T_c can be solely attributed to the pseudogap behavior. This implies that the pseudogap state coexists with the superconducting state below T_c . The coexistence possibly takes place even in the Zn-free sample, if we suppose that the SW saturation below T_c is due to the

4. RESULTS AND DISCUSSION

strong competition between the decrease due to superconductivity and the increase due to the pseudogap. Furthermore, the pseudogap behavior is observed even for the non-superconducting sample ($x = 0.04$), which further supports the idea that the pseudogap is not a precursor of superconductivity.

4.2.2 Pseudogap in the overdoped region

Another open question about the pseudogap is the behavior of the pseudogap in the overdoped region. There are different experiments reporting different behaviors. One group of experiments reported that the pseudogap line gradually decreases with increasing doping level and merges with the T_c dome in the overdoped region [78]. Other groups of experiments reported that the pseudogap line crosses the T_c dome, and reaches to zero at near $p = 0.19$ doping level [79]. These scenarios are shown as a schematic view in Fig. 4.13.

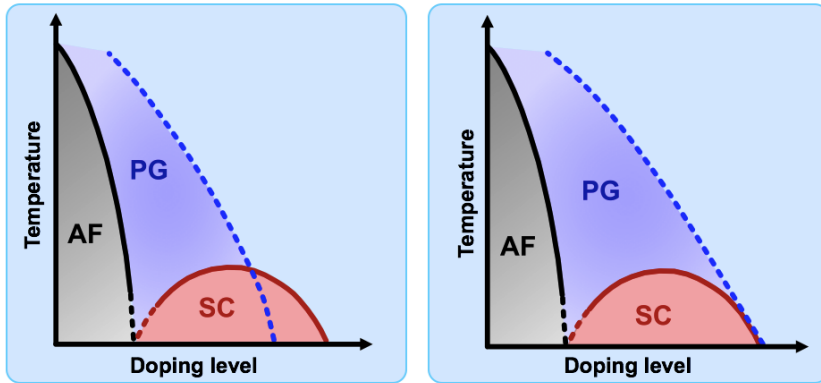


Figure 4.13: Scenarios of the pseudogap in the overdoped region - Scenarios for the behavior of the pseudogap in the overdoped region: Pseudogap goes to quantum critical point (left panel) or it merges with the superconducting dome (right panel).

In the previous part, the effects of Zn-substitution on the pseudogap behavior have been discussed. And we showed that the pseudogap temperature, T^* , is robust to Zn-substitution, even does exist for the non-superconducting sample. By using this property, we search for the pseudogap behavior in the overdoped region of the phase diagram. If the pseudogap line crosses the T_c dome, by reducing the T_c below the pseudogap temperature with Zn-substitution, we can observe the pseudogap opening.

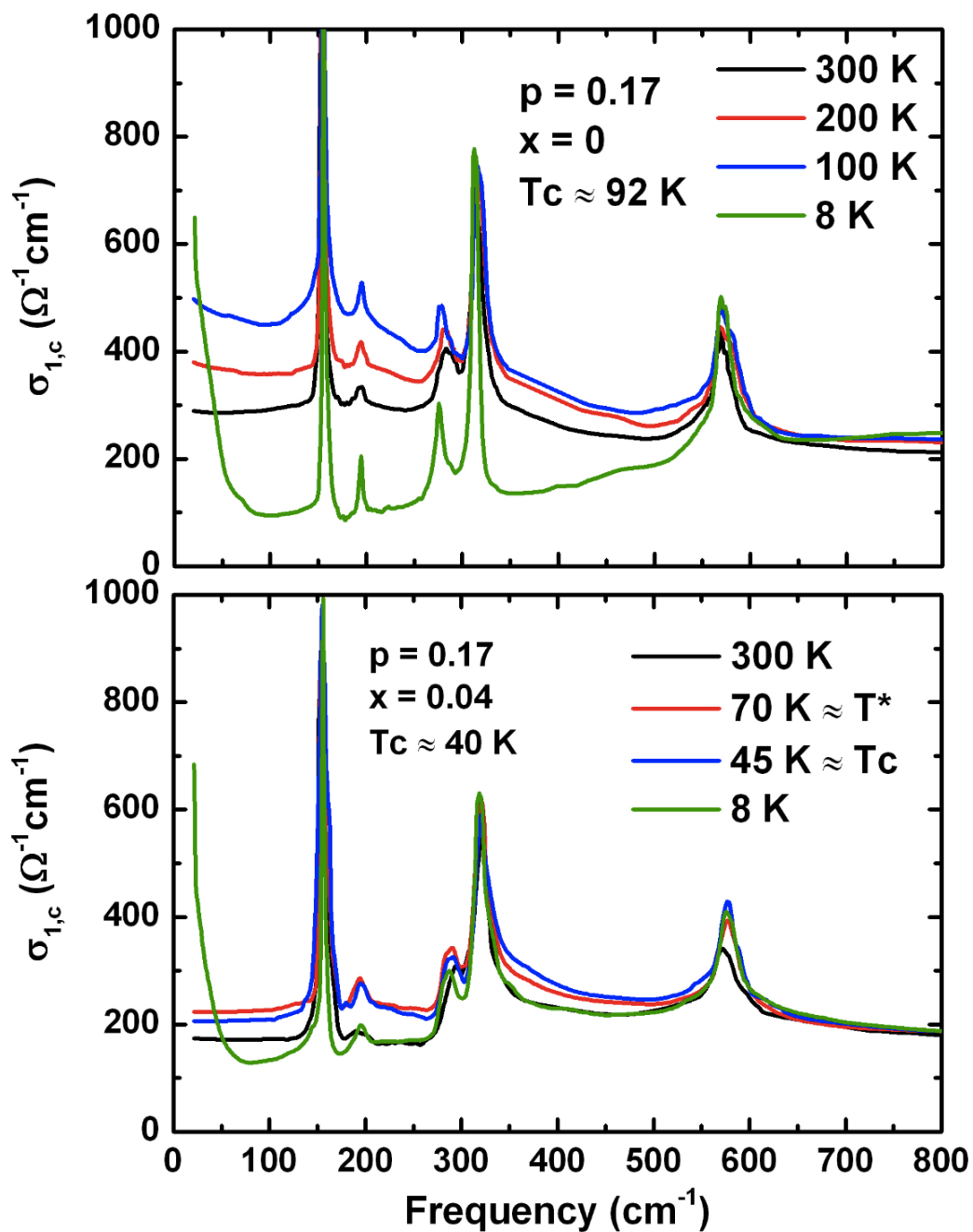


Figure 4.14: Zn-substitution effect on optical conductivity in the overdoped region - Temperature dependent optical conductivity of Zn-free and Zn-substituted samples in the overdoped region.

4. RESULTS AND DISCUSSION

To test this assumption, we prepared slightly overdoped samples with Zn-content $x = 0$ and 0.04 . Optical conductivity of those samples for several temperatures is given in Fig. 4.14. The sample with $x = 0$ shows a metallic behavior down to T_c . With superconducting gap opening, the suppression of the low energy optical conductivity can be seen. However, no pseudogap behavior was observed for this sample. For the Zn-substituted sample, the superconducting transition temperature is significantly lower than that for the Zn-free case. Even though at high temperatures, we observe a metallic behavior for this sample as well, with decreasing temperature, the low energy optical conductivity starts to show a suppression below T^* . In Fig. 4.15, the optical conductivity values at 50 cm^{-1} are plotted as a function of temperature for both samples in the underdoped and overdoped region, where we can easily follow the low- ω optical conductivity suppression with pseudogap opening. This result clearly demonstrates that in the overdoped region a clear pseudogap behavior is observed for the Zn-substituted sample. Since the pseudogap temperature does not change with Zn-substitution, we can suggest that it also exists for the Zn-free sample in the overdoped region. This supports the second scenario mentioned above. Moreover, this behavior supports the idea that the pseudogap is not a precursor of superconductivity, as well.

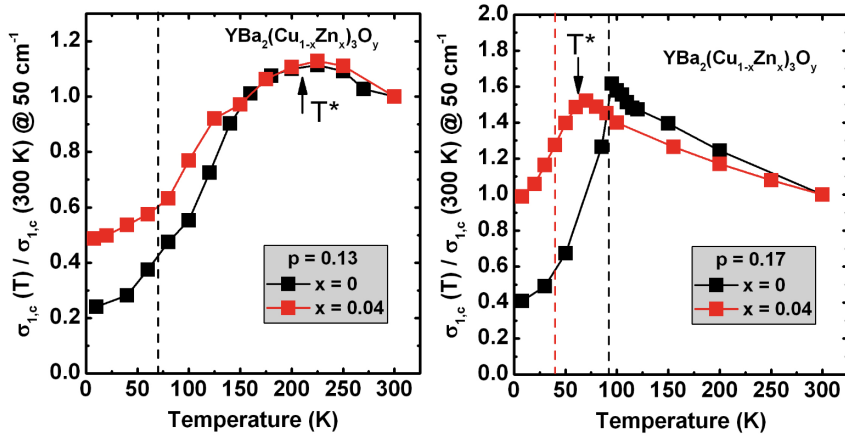


Figure 4.15: Low- ω optical conductivity: Demonstration of the pseudogap opening - Low- ω optical conductivity as a function of temperature in the underdoped (left panel) and overdoped (right panel) region. Pseudogap is robust to Zn-substitution, therefore, we see a suppression of low- ω optical conductivity at the same temperatures for Zn-free and Zn-doped samples. In the overdoped region a pseudogap behavior was observed for Zn-doped sample, which also can be thought as the same for the Zn-free sample, as well.

4.2.3 Interpretation of the pseudogap

It is difficult to pinpoint the origin of the pseudogap from our measurements. However, the results presented in this thesis show strong evidence to that the pseudogap is not the precursor of the superconductivity, but it is rather a different order. Therefore, we can eliminate the theories related with the pre-formed pairing scenarios. Moreover, we still can give some findings about the pseudogap initiated from our measurements.

As mentioned in Chapter 2, with the pseudogap opening, the low energy optical conductivity will be suppressed and the lost spectral weight in the low energy region is transferred to the high energy part of the spectrum. As a result, the overall spectral weight is conserved within the energy region in which the low energy to high energy transfer is completed. In Fig. 4.16, the doping dependence of the $\Delta\sigma_1$ ($\sigma_1(T_c) - \sigma_1(T^*)$) is given for the Zn-free sample. The difference spectra allow us to see the low energy suppression and the high energy transfer more easily. As can be seen from the figure, the high energy transfer shows a systematic behavior with doping. To talk about the origin of the pseudogap it is natural to look for an energy scale that defines the pseudogap. This might make easy the comparison with the proposed theories.

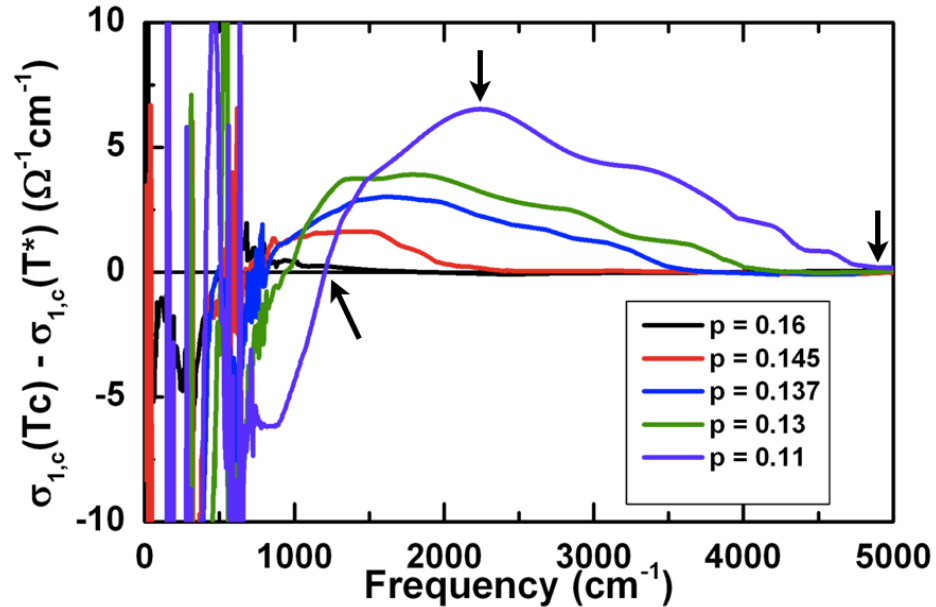


Figure 4.16: Doping dependent $\Delta\sigma_1(T-T^*)$ spectra - Doping dependent $\Delta\sigma_1(T-T^*)$ spectra. Arrows show the zero-crossing point, peak point, and the merge point.

4. RESULTS AND DISCUSSION

From the spectral weight transfer point of view, pseudogap behavior resembles to a density wave-like behavior. Unfortunately, we do not know the real energy scale (Δ_{PG}) of the pseudogap. Several points in the $\Delta\sigma_1$ spectrum can be associated with the pseudogap energy scale. For instance, the zero-crossing point, the peak position or the merge point (all are indicated by arrows in Fig. 4.16) can be thought as the energy scales that are related with the pseudogap. The scaling of the crossing, peak, and merge points with the obtained pseudogap opening temperature is shown in Fig. 4.17. Fig. 4.17 (a) shows the fitting that we obtained the peak position, although the broad structure of the spectrum makes the determination difficult. The anomaly points are compared with the pseudogap temperature with the $2\Delta_{PG}/k_B T^* = \text{constant}$ scaling. The constants for each anomaly points are given on the figures. As it can be seen from the figures all the anomaly points can be defined as a point that is related with the pseudogap phenomenon with a rather good scaling with T^* . It is clear that the features related to pseudogap phenomenon extend to high energies, especially with underdoping. On the other hand, it is challenging to explain these energies with the current theories.

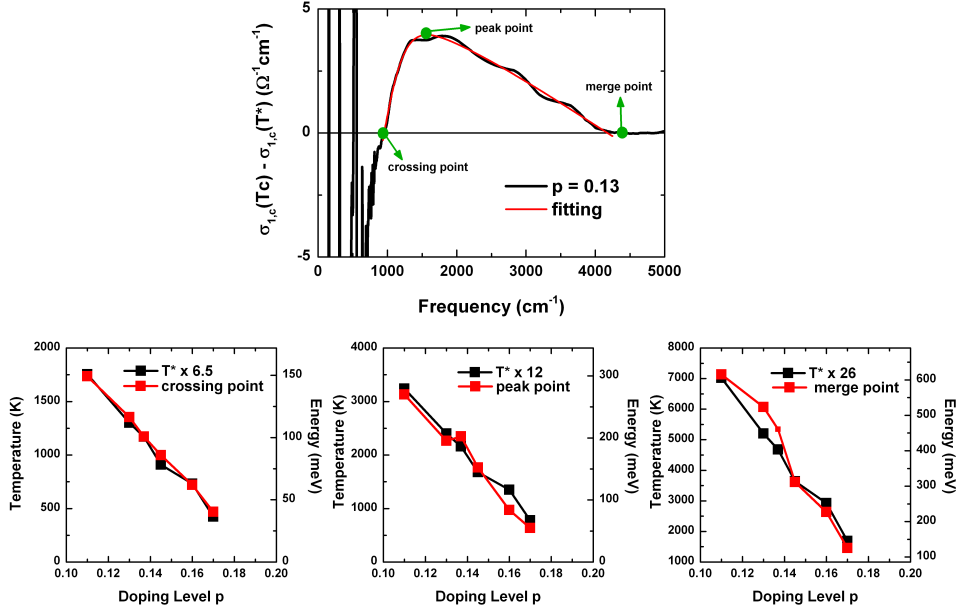


Figure 4.17: Determination of the pseudogap energy - (a) Determination of the crossing, peak, and merge points with fitting. Scaling of the anomaly points with obtained T^* values for crossing (b), peak (c), and merge points (d).

The Zn-substitution effects on the proposed anomaly points can also be examined as given in Fig. 4.18. None of these anomaly points show significant difference with Zn-substitution. This is especially surprising in terms of spin-density-wave or charge density-wave approach to the pseudogap, because, it had been shown that these orders are very sensitive to the impurity and they will be strongly suppressed with impurity doping [80, 81].

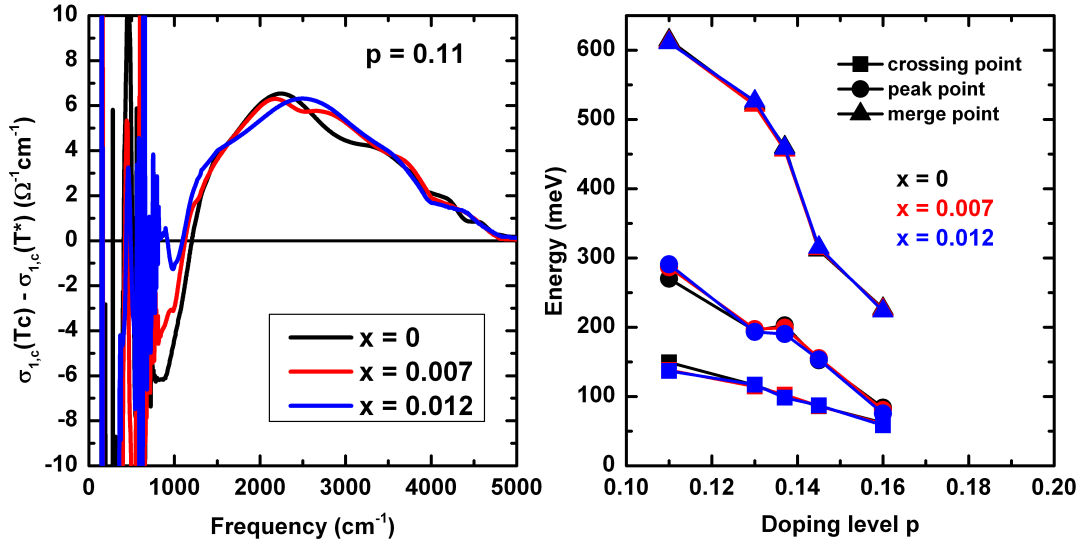


Figure 4.18: Zn-substitution effect on the pseudogap energy - (a) Zn-substitution effects on the observed anomaly points. (b) Doping and Zn-dependence of the crossing point

4.3 Discussion on Precursor Superconductivity

4.3.1 Precursor superconducting state in the optical conductivity

Our results indicate that the pseudogap is not a precursor of the superconductivity, but rather it is a competing order that coexists with superconductivity in the superconducting state. Further precise investigation of our SW calculations showed other interesting facts, as well. In the overall spectral weight shown in Fig. 4.9, we observed almost temperature independent SW below T^* with an abrupt decrease at T_c for our samples, as expected, since the SW transfer has happened in our calculation limits. However, a closer look at the data revealed that the observed decrease due to superconducting con-

4. RESULTS AND DISCUSSION

densation starts at temperatures higher than T_c . Even though the change relative to lowest temperature decrease is small, this behavior shows a systematic change with carrier doping, and Zn-substitution. Moreover, the temperature range also coincides with some discussions related to precursor superconductivity in the literature [22, 29, 72]. This situation encouraged us to investigate this point further.

Calculations from the real part of the optical conductivity

As mentioned previously, the missing area in the overall spectral weight is the indication of the superfluid density. Therefore, we calculated the SW in a wide energy region. Although given previously, in Fig. 4.19, an example is plotted again. Below T^* , the sum rule holds and temperature-independent SW can be seen. However, if we carefully look at the figure, we can see that the decrease of the SW actually starts above T_c . We determined the point where we start to see the decrease as the precursor state and marked as T_p . We also calculated the temperature dependence of the superfluid density. Usually in the literature of the optical studies, the superfluid density is calculated from the real part of the optical conductivity as in Eq. 4.2 [82].

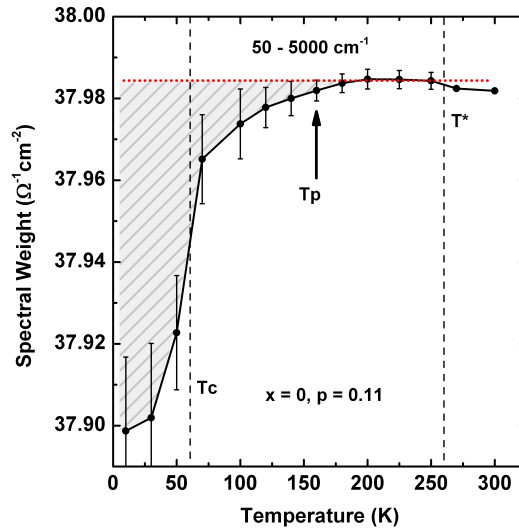


Figure 4.19: Determination of the superfluid density from real optical conductivity - The suppression of the overall spectral weight as an indication of the superfluid density. The abrupt suppression can be seen below T_c , however, it starts above T_c .

4.3 Discussion on Precursor Superconductivity

$$\frac{n_s}{m^*} \propto \omega_{ps}^2 = \frac{120}{\pi} \int_0^{\omega_{cut}} [\sigma_{1,n} - \sigma_{1,s}] d\omega \quad (4.2)$$

Here $\sigma_{1,n}$ is the real part of the optical conductivity in the normal state, for which will be the data just above T_c ; $\sigma_{1,s}$ is the real part of the optical conductivity in the superconducting state, which will be the data of the lowest measured temperature. In our case, we did the same analysis for each consecutive temperature where we start to see a missing area.

Calculations from the imaginary part of the optical conductivity

Although the missing area in the real part of the optical conductivity is very specific to the superconducting condensation state, it is not the only way to determine the superfluid density. We also can determine superconducting carrier density from the imaginary part of the optical conductivity. In the superconducting state, the superconducting carriers are condensed to a δ -function at $\omega = 0$, which leads to the relation $\sigma_2(\omega) \sim \omega_{ps}^2/\omega$ through Kramers-Kronig transformation. Therefore, $\omega\sigma_2(\omega)$ should show a frequency independent value which gives the superfluid density. However, this approach assumes that there is no normal carrier component below the superconducting gap energy in the superconducting regime, which is not the case for the high temperature cuprate superconductors that shows residual absorption below the superconducting gap even at $T \ll T_c$. Therefore, we have to subtract the normal carrier component from $\sigma_2(\omega)$ labeled as $\sigma_{2,normal}(\omega)$ in this thesis - which can be calculated by taking the KK transformation of the real part of the optical conductivity, $\sigma_1(\omega)$. In Fig. 4.20 an example of the analysis is shown at several temperatures for $p = 0.11$ and $x = 0$. The detailed analysis regarding $\sigma_2(\omega)$ was proposed previously and this method was examined by several research groups and well justified [82].

After calculating the normal carrier component in $\sigma_2(\omega)$, we can easily obtain the superconducting carrier component by subtracting the normal part from the overall $\sigma_2(\omega)$. We repeated this process for each temperature and in Fig. 4.21 plotted the superfluid density for each temperature that is calculated from $\sigma_1(\omega)$ and $\sigma_2(\omega)$. The same calculations for the Zn-substituted samples were also plotted. Here each column show the doping dependence, whereas each row represents the Zn-doping effect. The superfluid densities calculated with both methods coincide with each other except for

4. RESULTS AND DISCUSSION

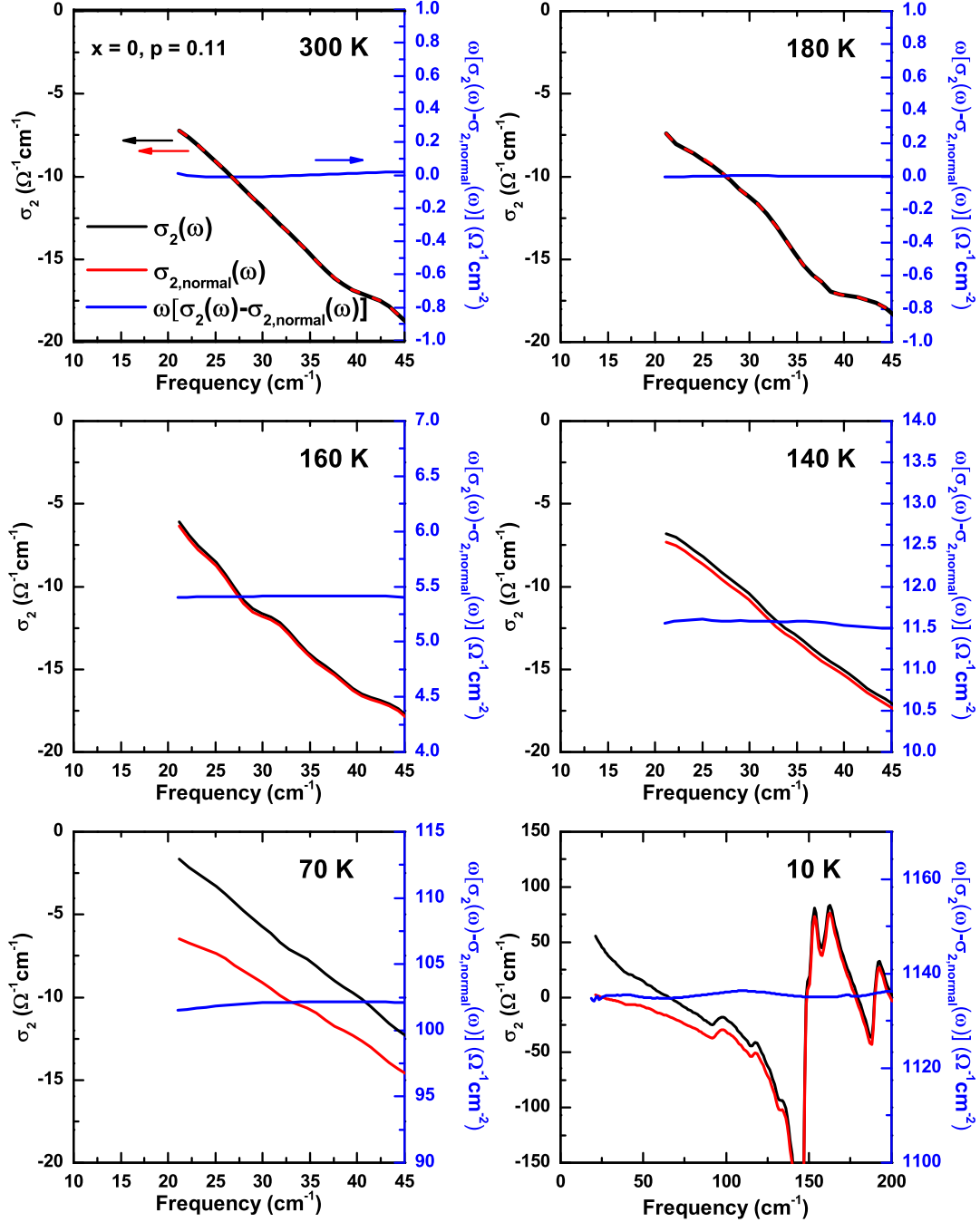


Figure 4.20: Determination of the superfluid density from imaginary optical conductivity - The normal component in $\sigma_2(\omega)$ has been calculated with the KK-transformation of the $\sigma_1(\omega)$. By subtracting this value we can determine the $\sigma_2(\omega)$ of superconducting carriers where $\omega\sigma_2(\omega)$ gives a constant that is related with the carrier density.

4.3 Discussion on Precursor Superconductivity

the superconducting state, while the temperature dependence of the superfluid density is exactly the same for both methods. The discrepancy in the superconducting state will be discussed later.

Results of the calculations show that the superfluid density starts to appear at temperatures much higher than T_c (marked as T_p) and gradually increases towards T_c . However, the increase is not monotonous down to T_c . At slightly higher temperatures (marked as T'_c) the increase becomes steeper. And finally below T_c , we observe a very fast increase of the superconducting carrier density.

The doping dependence of these two characteristic temperatures above T_c is surprisingly different. T_p shows increasing behavior with decreasing doping, while T'_c follows the T_c dome closely. Due to these different behaviors, they are getting closer to each other towards the optimum doping level. Our temperature steps are not small enough to resolve the difference between these two temperature scales in this doping region. However, the Zn-doping dependence of these scales show similar behavior, namely, with increasing Zn-content, we observe the decrease of both T_p and T'_c . This strongly suggests that both temperature scales are related to superconductivity, and unlike pseudogap they are not robust to the suppression of the superconductivity with Zn-substitution. In Fig. 4.22 we plot all of our temperature scales on the phase diagram. Moreover, a normalized scale (normalization has been done to the optimum doping level) also demonstrates the decrease of the T_p , T'_c , and T_c with x , while T^* is not the case (Fig. 4.23).

4. RESULTS AND DISCUSSION

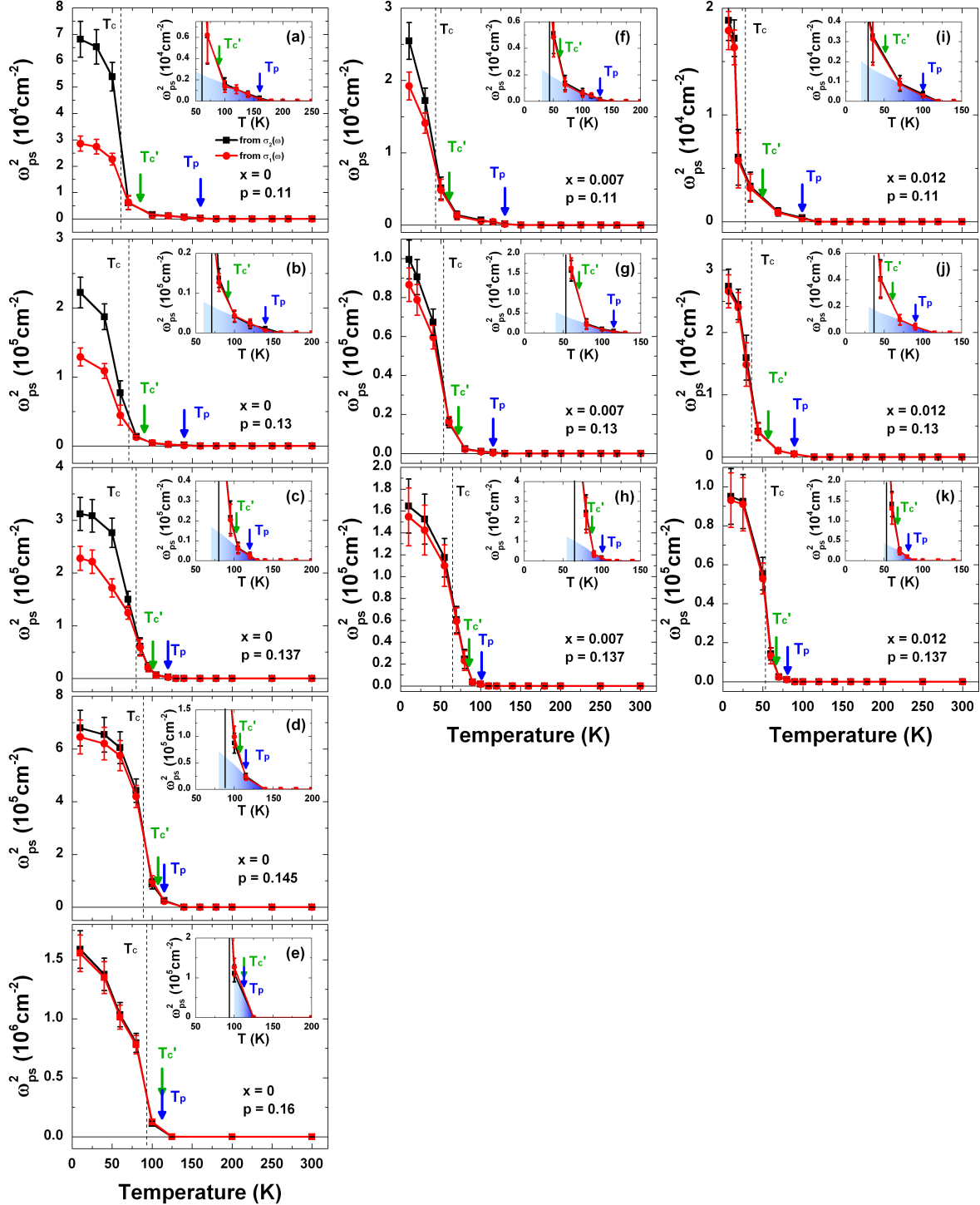


Figure 4.21: Doping and Zn-dependence of the superfluid density obtained from $\sigma_1(\omega)$ and $\sigma_2(\omega)$ - Each column demonstrates the doping dependence of the superfluid density and each row shows the Zn-dependence of the superfluid density obtained from $\sigma_1(\omega)$ (red curves) and $\sigma_2(\omega)$ (black curves). Insets enlarge the high temperature part of each curve to show the T_p and T'_c scales more clearly.

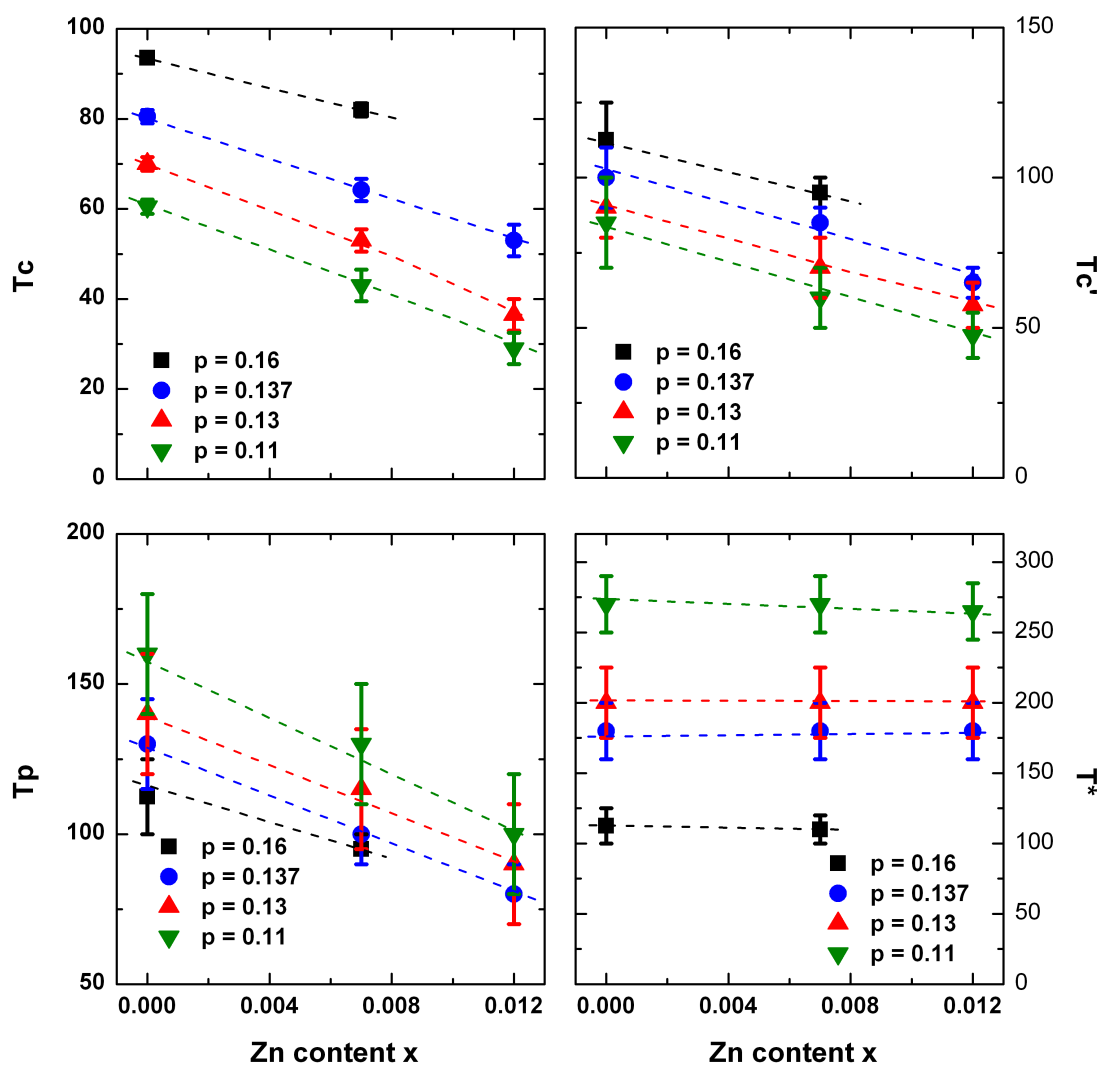


Figure 4.22: Zn-doping effect on the observed temperature scales as a function of doping - Zn-doping effect on the observed temperature scales as a function of doping

4. RESULTS AND DISCUSSION

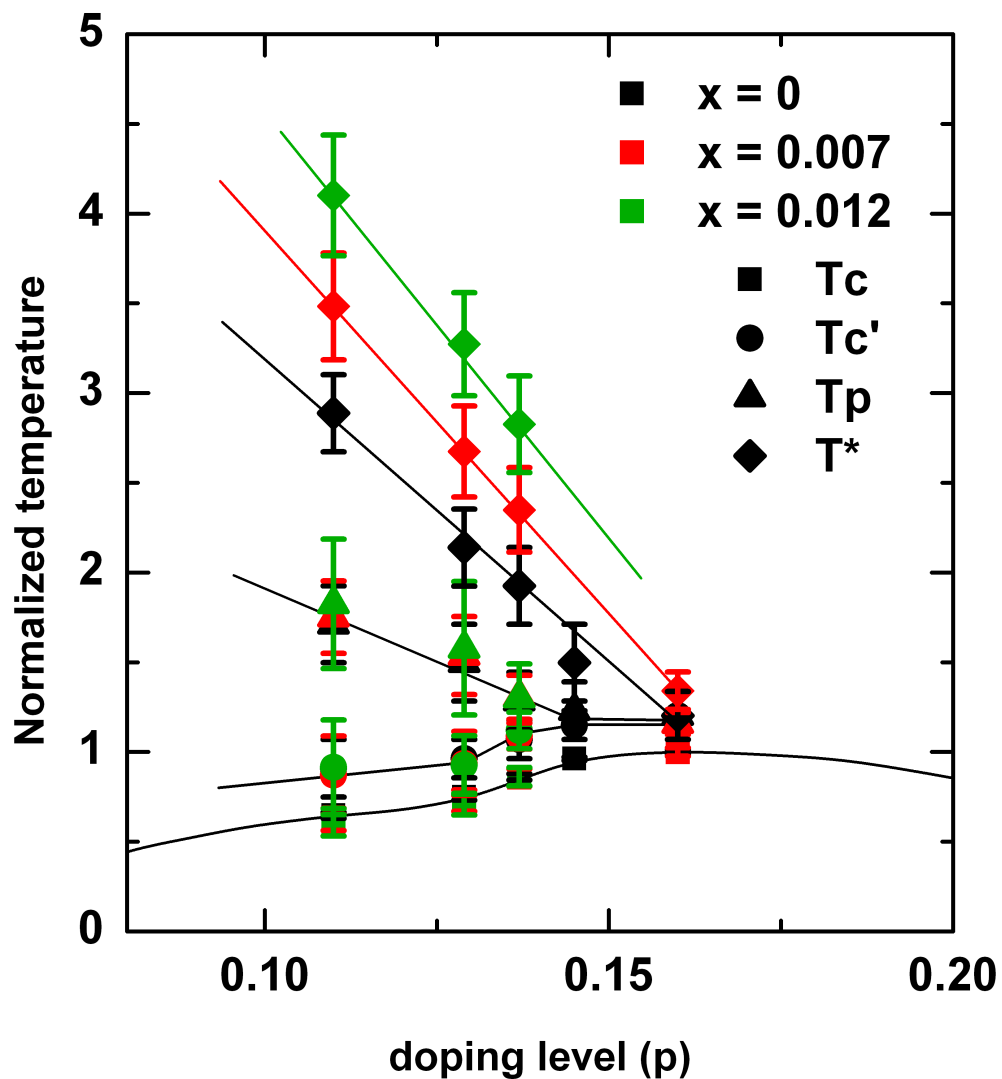


Figure 4.23: Phase diagram of the Zn-substituted samples - Normalized phase diagram which show the decrease of the temperature scales with respect to the T_c decrease with Zn-doping. All the values are normalized to the optimum doping T_c . As can be seen that the T_c' and T_p decrease almost same with T_c , hence a single curve had been observed for all samples. T^* greatly deviates from a single curve, because it does not change with Zn-substitution.

Other implication of the precursor state in the c -axis optical spectrum

Previously the TJP resonance seen above T_c was attributed to the precursor superconducting state, as [72]. The study was performed on impurity-free samples for several doping levels. In our study, we also obtained the temperature dependence of the TJP mode by tracing the phonon anomaly of the oxygen bending mode (at 320 cm^{-1}) and compared the temperature region with our results of Fig. 4.21. Moreover, it is new to obtain the Zn-doping dependence of the TJP mode.

In Fig. 4.24, the temperature dependent frequencies of the oxygen bending mode are plotted at several doping levels for Zn-free and Zn-substituted samples. Here the arrows show the temperatures obtained with the optical conductivity calculations. As can be seen in the figure, the softening of the phonon mode starts at very high temperatures, indicating the appearance of the TJP mode at high temperatures. And the softening temperature shifts to higher temperature with decreasing doping level. The comparison between Zn-free and the Zn-substituted samples showed that the softening temperature decreases with Zn-substitution for the same doping level. For side by side comparison, in Fig. 4.25 we plotted the superfluid density obtained from the optical conductivity with the temperature dependence of the phonon mode. As can be seen in the figure, the critical temperature T_p is perfectly match with each other.

The TJP mode is gradually suppressed with Zn-substitution, therefore, we can determine the existence of this mode only for the 0.7% Zn-substituted sample. This is the down fold of this method to determine the precursor superconducting state. Once we suppress it with Zn-doping, we cannot trace it anymore, even though other methods allowed us to distinguish the precursor state, even for samples with higher Zn-content. Nonetheless, we evaluate the temperature scale from the evaluation of the TJP mode and compare it with our other calculation methods (SW analysis and $\sigma_2(\omega)$).

Up until now, we discuss the results where the lowest doping level were $p = 0.11$. To see lower doping region we prepared a sample with 15 K transition temperature that corresponds to the doping level $p \approx 0.06$. To obtain the samples in this doping region is very difficult. Samples are extremely air sensitive and during the quench process and later with the room temperature annealing process, the T_c of the samples changes very quickly in this under doped region. Moreover, it is especially difficult in our case, because the samples used in our measurements are quite big and to obtain uniform

4. RESULTS AND DISCUSSION

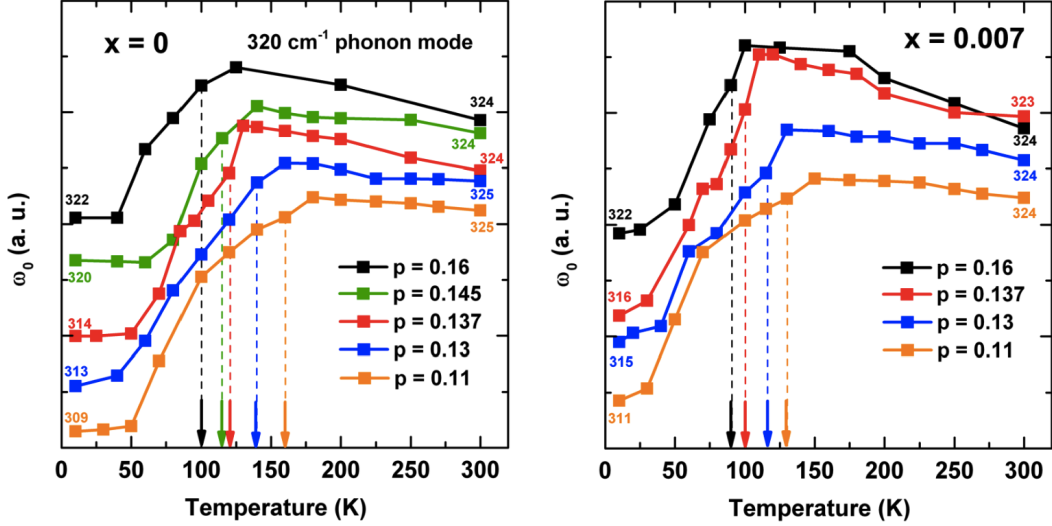


Figure 4.24: Doping and Zn-doping dependence of the oxygen bending mode - The resonance frequency of the oxygen bending mode as an indication of the TJP mode has been given for Zn-free (left panels) and Zn-substituted (right panels) samples. Arrows indicate the temperatures obtained from the optical conductivity calculations. It is shown that the observed temperature scales are match with the optical conductivity calculations for each doping levels with the dashed lines.

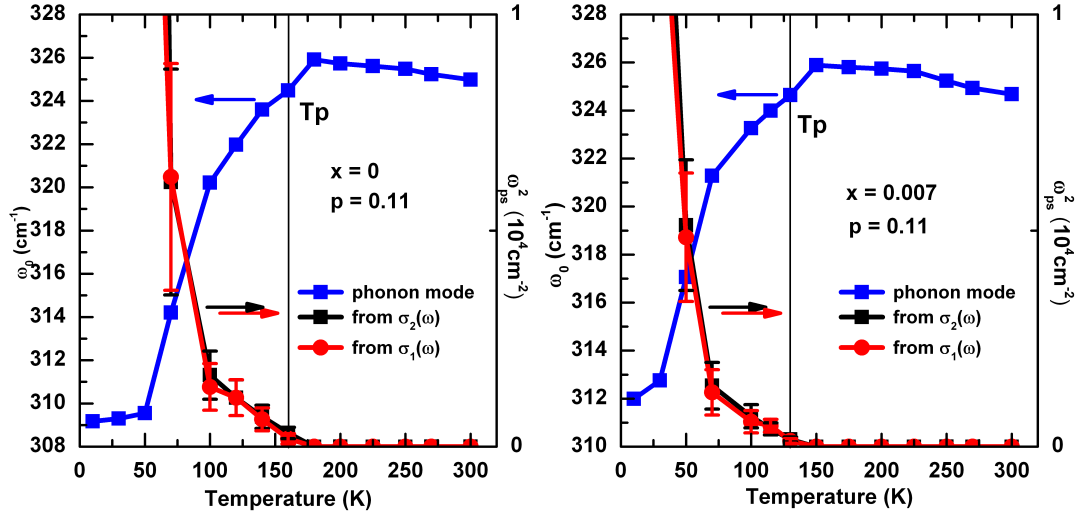


Figure 4.25: Comparison of the T_p values obtained by several methods - Superfluid density that is calculated from real and the imaginary parts of the optical conductivity (red and black curves) and the phonon mode show the same T_p scale. This consistency also observed for the 0.7% Zn-substituted sample, as well.

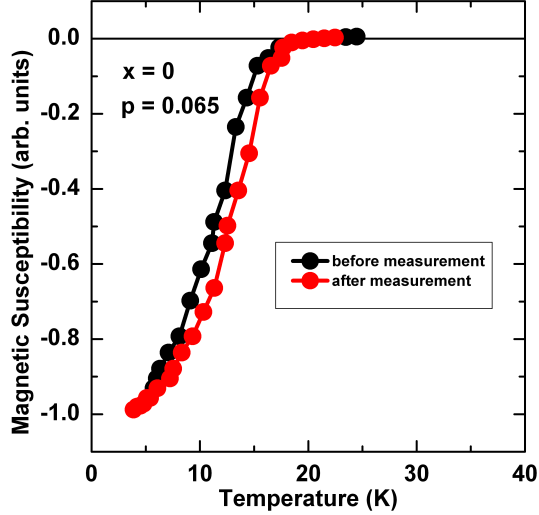


Figure 4.26: Magnetic susceptibility of the heavily underdoped sample - Magnetic susceptibility of the heavily underdoped sample before and after FTIR measurements. In this doping region, the used sample is highly sensitive to the environment. Almost similar transition temperature shows that during the measurement, the properties of the sample did not change significantly.

samples are challenging. Nevertheless, we obtained a 15 K sample with relatively sharp transition. The magnetic susceptibility curve has been given in Fig. 4.26 for before and after FTIR measurements. Despite the difficulty of sample handling, the T_c of the sample did not change significantly during our FTIR measurements.

The reflectivity and optical conductivity of this sample are shown in Fig. 4.27. The temperature dependence of the reflectivity and the optical conductivity for this sample is significantly small. Therefore, it is not possible to perform the calculations that we did on the electronic component of the optical conductivity. The features are well below the accuracy of the calculations. However, the TJP mode can be seen very clearly, with the anomaly in the oxygen bending mode. Therefore, we used this method to calculate the precursor state for this sample. For this sample, T_p has been determined to be around 160 K (temperature dependent resonance frequency of the oxygen bending mode is given in Fig. 4.28). We plotted our temperature scales on the phase diagram in Fig. 4.29. As can be seen, the T_p temperature scale does not exactly follow the pseudogap behavior, but rather shows a saturated behavior towards the low doping region. In the next part, we give a detailed explanation to all temperature scales

4. RESULTS AND DISCUSSION

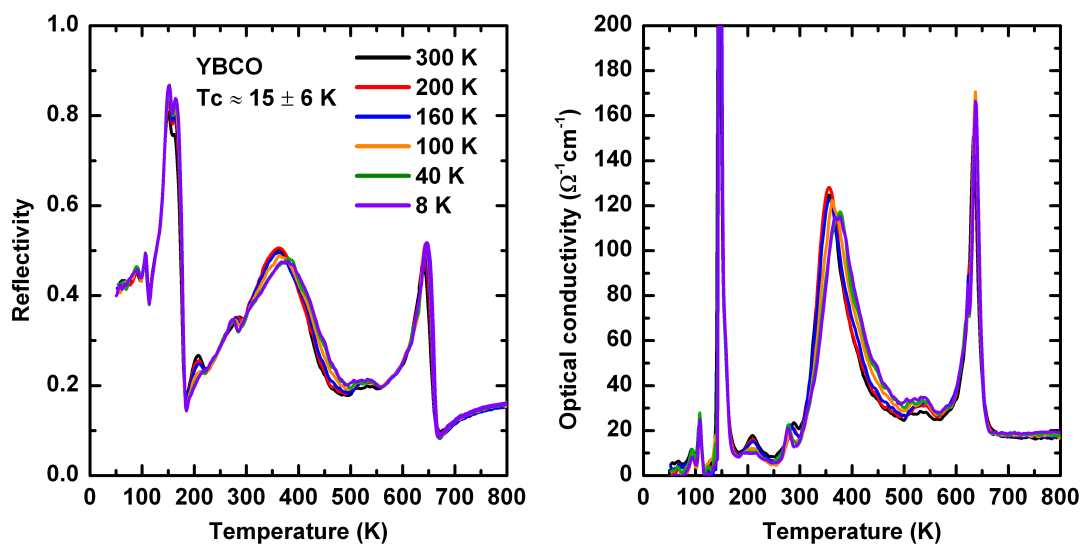


Figure 4.27: Optical spectra of the heavily underdoped sample - Optical spectra of the heavily underdoped sample that is almost temperature independent.

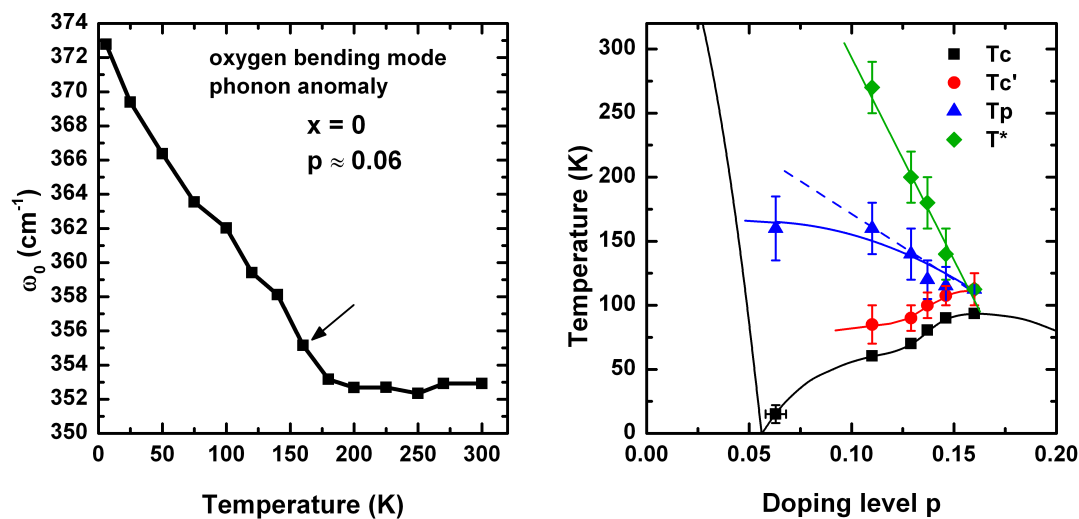


Figure 4.28: T_p temperature for the heavily underdoped sample is determined from the TJP mode.

Figure 4.29: T_p temperature scale for the heavily underdoped region.

that we observed in comparison with the other reported results.

4.3.2 Comparison of our phase diagram with the results of other probes

In Fig. 4.30 we compare our results for the Zn-free samples with the published data of $\text{YBa}_2\text{Cu}_3\text{O}_y$ determined by the other probes. Solid symbols represent our data. Our T'_c values are in good agreement with the recent results of microwave measurements on $\text{YBa}_2\text{Cu}_3\text{O}_y$ [30]. Moreover, the temperature scale of T'_c relative to T_c is also consistent with the results of THz [27, 83] and microwave measurements [84] for another cuprate system, $\text{La}_{2-x}\text{Sr}_x\text{CuO}_4$. On the other hand, neither THz nor microwave measurements detected the temperature scale T_p . This might be due to the ambiguity in determining the normal carrier component which we need to subtract in the analysis to calculate ω_{ps}^2 from $\sigma_2(\omega)$ [82].

Our T_p values are in good agreement with the temperatures observed by ellipsometry [72], the Nernst effect [85], thermal expansivity [86], and the Hall effect [87]. Although, ellipsometry provides the same information with the present study in principle, T_p was estimated only from the phonon softening related to the TJP resonance, which is not direct evidence for superconducting condensate. It may be worth noting that T_p well coincides with the spin gap temperature reported by neutron scattering [88] and the relaxation rate T_1^{-1} of NMR [16, 89].

Our results suggest that the pseudogap is not a precursor of superconductivity. Instead, we can define a precursor state at temperatures lower than T^* but much higher than T_c with an unusual doping dependence. The observation of the condensed superconducting carriers suggests that this precursor state does not only reflect the pairing state but also some sort of coherence. In the scheme of inhomogeneous superconductivity, this kind of correlation can be observed without macroscopic superconductivity [90]. The inhomogeneous superconducting state can generally be explained by the phase separation [91], or the spin-gap proximity mechanism [92], where the theories have been developed in terms of the doped Mott insulator. The doping dependence of T_p is similar to the prediction of the mean field theory of the t - J model [11]. The direct observation of the finite $\sigma_2(\omega)$ in this study indicates that some kinds of seeds of superconductivity are created at the high temperature T_p , and they develop into macroscopic superconductivity at T'_c . The fact that T_p increases with underdoping suggests the importance

4. RESULTS AND DISCUSSION

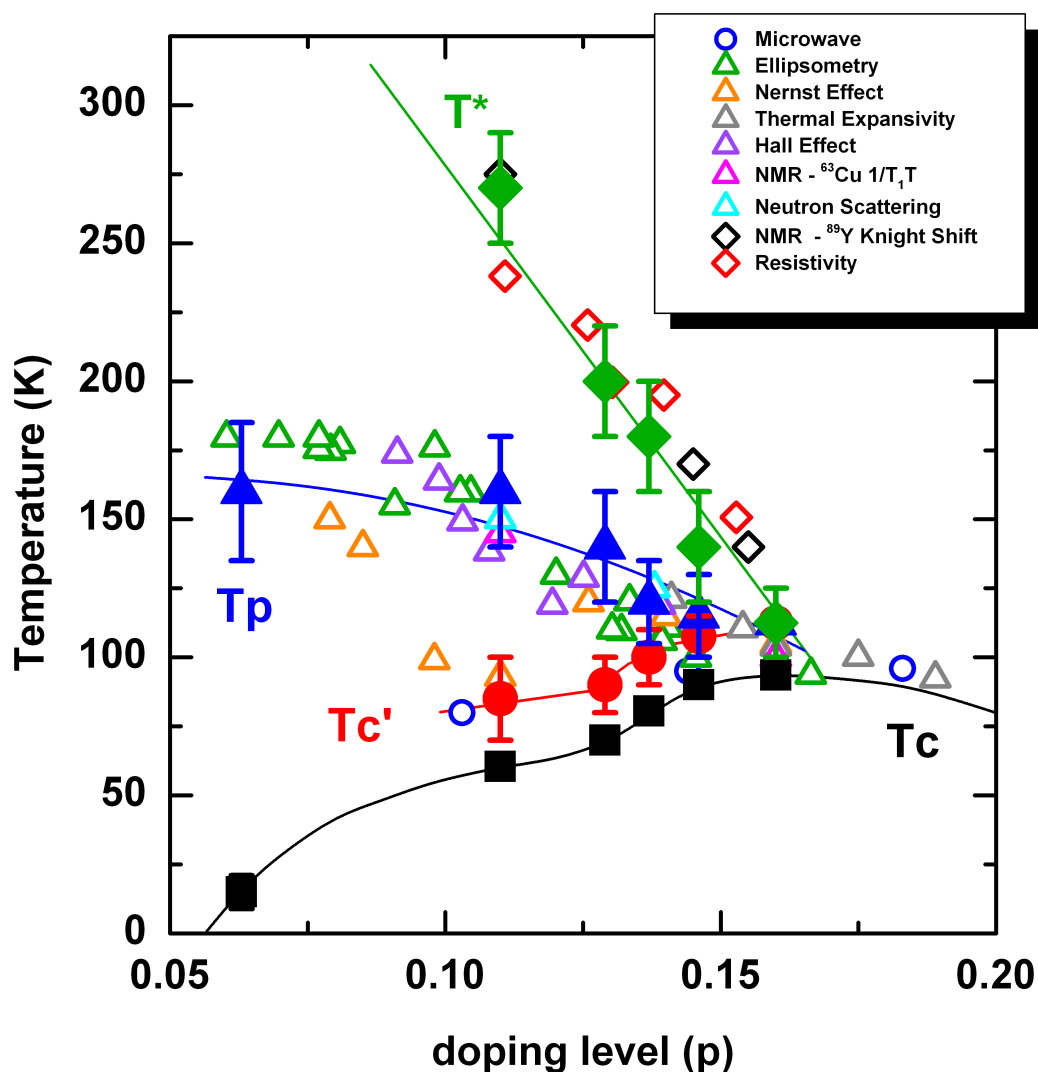


Figure 4.30: Obtained temperature scales of $\text{YBa}_2\text{Cu}_3\text{O}_y$ that are compared with other probes - Phase diagram of $\text{YBa}_2\text{Cu}_3\text{O}_y$. Solid symbols are obtained in this study. Microwave: [30], Ellipsometry: [72], Nernst effect: [85], NMR $1/T_1T$: [16, 89], Neutron scattering: [88], NMR Knight shift: [76], and Resistivity [77]

4.3 Discussion on Precursor Superconductivity

of “Mottness” in the superconductivity mechanism of the cuprates. Moreover, the Zn-dependence of the temperature scales give further evidence to the fact that the T'_c and T_p are superconductivity related features, while T^* is not.

4.3.3 Interpretation of the precursor superconducting state

The precursor of the superconductivity was discussed after observation of the first superconductors. Superconducting fluctuation scenario is proposed by Ginzburg-Landau [93], where the temperature range of the fluctuations can be given as the $t_{GL} \sim T_c/\xi$. On the other hand, the fluctuation range above T_c was predicted to be around $10^{-12} - 10^{-14} T_c$ owing to the fact that these materials have very low T_c and very long coherence length. Therefore, such a small fluctuation range could not be observed experimentally. For the high temperature cuprates, on the other hand, these superconducting fluctuations are expected to be more prominent due to the high transition temperatures and short coherence lengths of these materials. And it has been proposed that we can observe these fluctuations at the temperature range of $10^{-1} - 10^0 T_c$ of the sample. However, the observed temperature range in our measurements for T_p is significantly higher than the predicted temperature range, especially in the underdoped region. Therefore, we cannot explain the T_p temperature range within the conventional fluctuation theory that is proposed by Ginzburg-Landau.

Another explanation that was given for the precursor superconducting state was the Cooper-pairing without long-range phase coherence (incoherent Cooper pairs) [94]. This proposal was given to explain the pseudogap as the precursor of the superconductivity, initially. From the doping dependence point of view, this discussion can be attributed to the T_p temperature scale, as well. Superconductors are macroscopic quantum states that are emerged from the coherent states of the paired electrons (Cooper-pairs), where the order parameter can be described as $\Psi = |\Psi|e^{i\Phi}$. In this scheme, the components of the order parameter should be identified separately as the amplitude ($|\Psi|$) and the phase (Φ). In this case, two different temperature ranges above T_c can be identified. The first region is the regime (very small region above T_c that follows the doping dependence of the T_c), where the phase is still coherent, while the amplitude is constant. This region can be explained by the Berezinskii-Kosterlitz-Thouless theory in 2D [95, 96]. Here, I should point out that this regime coincide with the region that is defined by our T'_c temperature scale. The second region is the regime (extending to

4. RESULTS AND DISCUSSION

very high temperature region and showing pseudogap-like doping dependence), where the phase is incoherent but $|\Psi|$ is still non-zero. In this case this temperature range can be explained with the locally fluctuating Cooper-pairs. Therefore, previously pseudogap, and perhaps in this study the T_p state are defined as the fluctuating Cooper pairs without long-range phase coherence. In this case, it is not possible to observe any condensed superconducting carriers. However, in the present study we observed the real superconducting condensate, which shows evidence against the scenario of fluctuation without phase coherence.

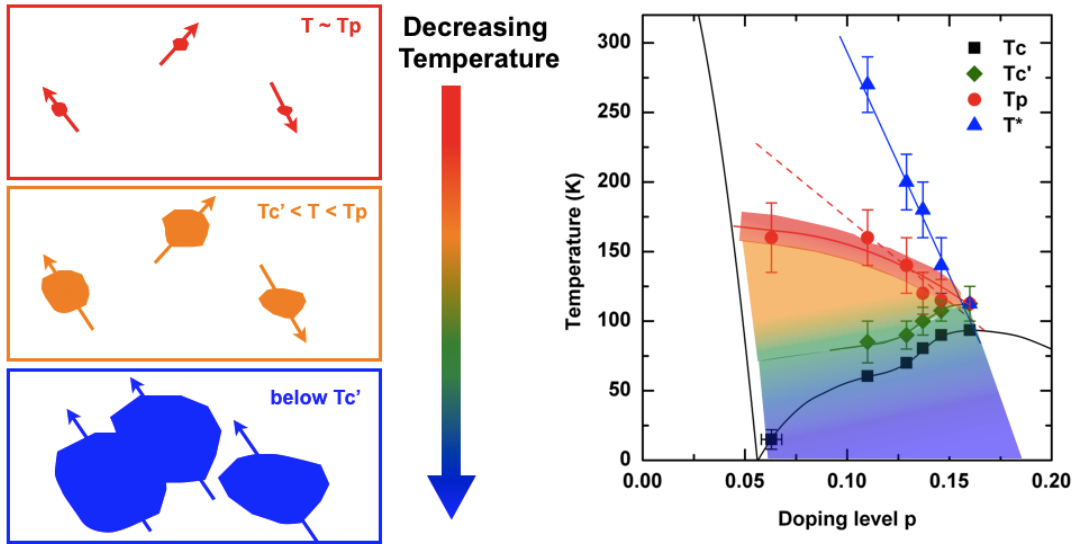


Figure 4.31: Schematic of the inhomogeneous superconducting state scenario - Schematic of the inhomogeneous superconducting state scenario. Arrows in the left panel indicate the phase coherence of superconductivity.

The inhomogeneous superconducting regime is another explanation for the precursor superconductivity [90]. Our findings in this thesis support the inhomogeneous superconductivity scenario. In Fig. 4.31, the explanation to this scenario is given. Since our study focus on the underdoped region, the figure is basically for the underdoped region. In this scenario, our observed temperature scales and other observations such as the existence of the superfluid density above T_c can be explained. With crossing T_p , superconducting regions start to appear in the system. If they are bigger than the coherence length, these superconducting regions can survive. Otherwise, these regions will be suppressed with the proximity effects. The coherence length is given as ~ 1 nm

4.3 Discussion on Precursor Superconductivity

at the optimum doping and increasing up to 3 nm for 60 K sample [97]. These regions show coherence within the superconducting region, however, their phases are not necessarily coherent (red plate). With decreasing temperature these superconducting regions start to expand (orange plate). Even though the superfluid density is increasing with this expansion, since these regions have no connection to each other, system does not show bulk superconductivity with zero resistivity. Below T'_c , the separated superconducting regions starts to see each other, and a phase coherence between these regions starts to appear, hence the system goes to the route of bulk superconductivity. Finally, with reaching T_c , we observe zero resistivity and bulk superconductivity in the system.

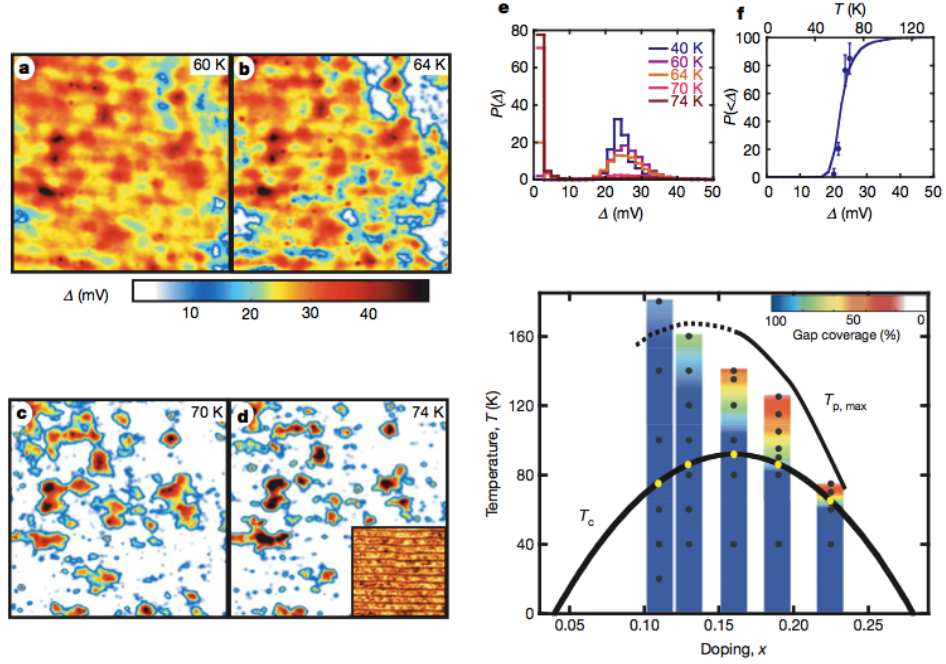


Figure 4.32: Indication of the precursor superconducting state in STM - (a-d) Gap map of the overdoped $\text{Bi}_2\text{Sr}_2\text{CaCu}_2\text{O}_{8+\delta}$ single crystals with $T_c = 65$ K. The value of the gap is extracted from local spectroscopic measurements by using the experimental criterion that the local dI/dV has a maximum at $V = +\Delta$. (e) shows the gap distribution. (f) The solid line shows the probability $P(<\Delta)$ that the gaps are less than a given Δ (lower x axis). The phase diagram demonstrates the temperature scale that the gap profile is started in the system as $T_{p,max}$ [98].

4. RESULTS AND DISCUSSION

In this kind of scenario, it is expected to see some effects in other experimental probes, as well. For instance, since we observe a superconducting condensation, it might be expected to observe a gapped state above T_c . One of the probes that can observe this state in the real space is the Scanning tunneling microscope (STM). Such kind of study has been performed for the $\text{Bi}_2\text{Sr}_2\text{CaCu}_2\text{O}_{8+\delta}$ samples in a wide doping range [98]. In the overdoped region, where the pseudogap effects cannot be observed, it has been shown that the gapped state persists at temperatures higher than T_c (Fig. 4.32). They observed that the temperature range, where the gapped state can be observed, expands with decreasing doping level. On the other hand, the results in the very underdoped region were not conclusive enough, since they could not eliminate the effects of the pseudogap.

Another probe that we may expect some differences is the in-plane resistivity. If some part of the sample becomes superconducting in the CuO_2 planes, then a decrease in resistivity will be expected, even though we cannot observe zero resistivity.

A detailed resistivity work for the in-plane polarization had been performed for the $\text{YBa}_2\text{Cu}_3\text{O}_y$ system [20]. We compared our temperature scales with these resistivity results by checking the slope change of the resistivity plot. In Fig. 4.33, the change of slope at T^* , T_p , and T'_c is demonstrated. This is a very crude estimate, for example it does not take into account the effects of the other orders, such as charge order, etc [99, 100]. Indeed such kinds of orders are discussed for cuprates. Nonetheless, the slope change of the resistivity coincides with the obtained T_p scale.

4.4 Remarks on Kinetic Energy Driven Superconductivity

Previously, we showed that ω_{ps}^2 determined from $\sigma_1(\omega)$ missing area is different from that of $\sigma_1(\omega)$. This discrepancy has been reported for many cuprate systems previously [101] and attributed to the kinetic energy reduction which the carriers experience during the superconducting transition. This difference gradually decreases with increasing doping level.

In our experiments, we also observed this discrepancy for the Zn-free samples. On the other hand, with increasing Zn-content, we observed the disappearance of the difference even for the underdoped region. In Fig. 4.34 we plotted the ratio of this dis-

4.4 Remarks on Kinetic Energy Driven Superconductivity

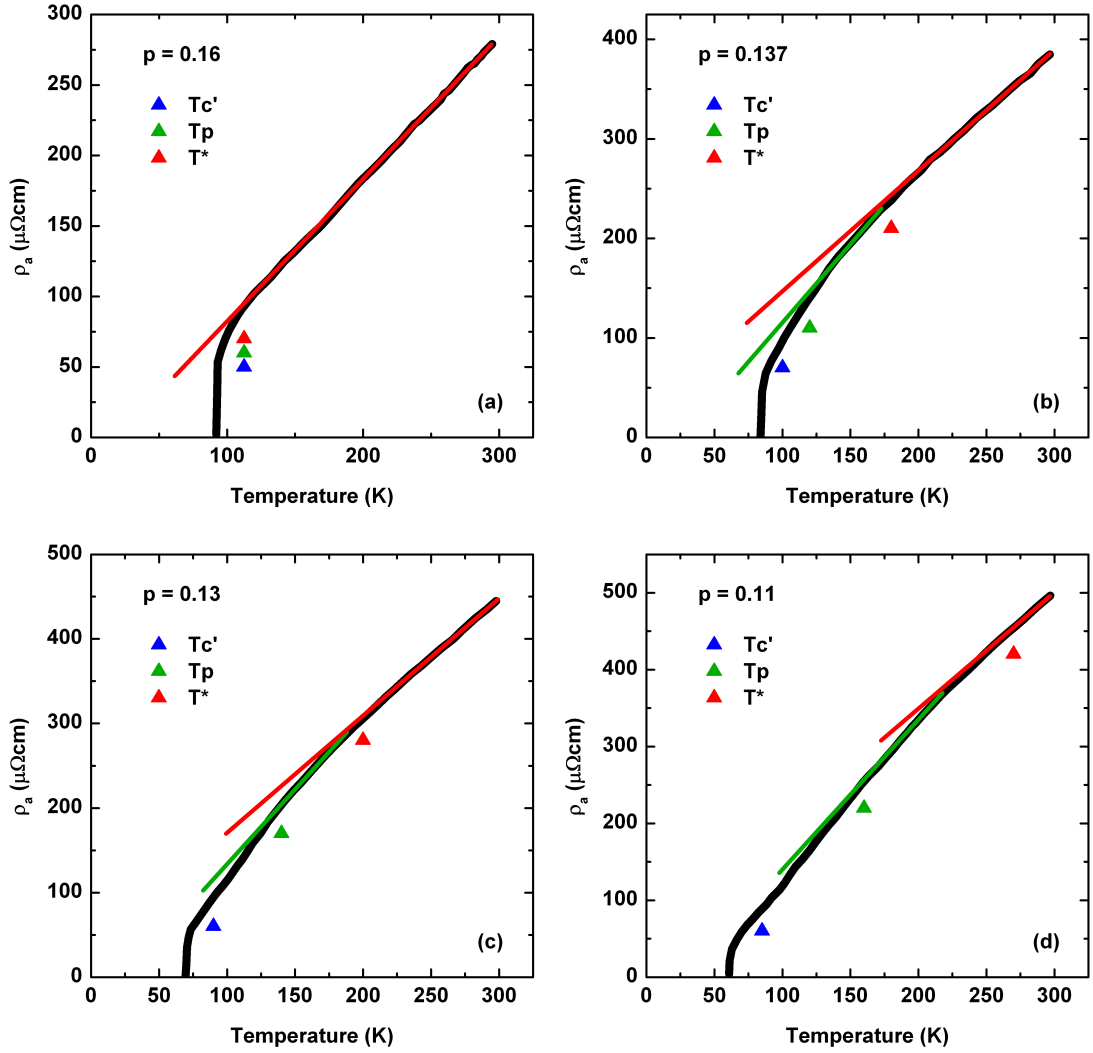


Figure 4.33: Indication of the precursor superconducting state in inplane resistivity - The slope change of the inplane resistivity curves had been traced. A decreasing trend of the resistivity (increasing slope) can be seen with the pseudogap opening, T_p , and T_c' . The resistivity curves are traced from [20]. Solid symbols are the temperature scales that are determined from our infrared measurements.

4. RESULTS AND DISCUSSION

crepancy for Zn-free and Zn-substituted samples at 10 K. Here ΔN and ρ_s are the superfluid densities calculated from $\sigma_1(\omega)$ and $\sigma_2(\omega)$, respectively.

For conventional superconductors, where the pairing and condensation are driven by the potential energy, the FGT sum rule holds. In other words, any discrepancy on superfluid density calculated from different methods should not be seen. On the other hand, J. E. Hirsch proposed that the FGT sum rule can be violated in some cases, and the cuprate superconductors are one of the systems where we can expect this violation [102]. In this case the superfluid density should be defined as in Eq. 4.3.

$$\omega_{ps}^2 = \frac{120}{\pi} \int_0^{\omega_{cut}} [\sigma_{1,n} - \sigma_{1,s}] d\omega + \Delta(KE) \quad (4.3)$$

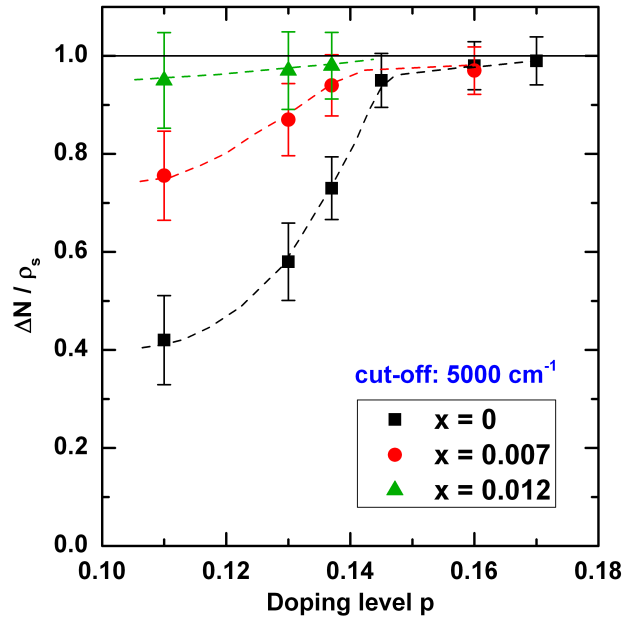


Figure 4.34: Doping and Zn-doping dependence of the observed discrepancy of superfluid density determined by two different methods - The kinetic energy component disappears with increasing Zn-content.

This violation implies that there is a finite contribution to the superfluid density from frequencies much higher than the superconducting gap, possibly near infrared or visible energy region. Indeed early studies on $\text{YBa}_2\text{Cu}_3\text{O}_y$ system showed that there is a high frequency missing area in this system [103]. However, these early results were on powder samples.

4.4 Remarks on Kinetic Energy Driven Superconductivity

Such kind of violation was observed in the c -axis optical spectra of the cuprates. On the other hand, it was shown that the observed kinetic energy change is much smaller than the condensation energy in interlayer tunneling model. Therefore, it has been thought that this difference should be compensated in the in-plane spectrum [104, 105].

So far, the kinetic energy change is only reported for the Bi2212 system by infrared spectroscopy [106] (it has been shown that the high energy contribution is around 20% for the underdoped region) and pump-probe reflectivity measurements [107]. However, it was shown that this is not the case for the $\text{YBa}_2\text{Cu}_3\text{O}_y$, and depending on the cut-off frequency the discrepancy in the in-plane spectrum disappeared [108]. As a result, even though it has been proposed by some systems it has not been observed for the others. Moreover, the condensation energy cannot be explained solely with this phenomenon. Therefore, another explanation might be necessary.

In this thesis, with the results of the Zn-substituted samples, we proposed another explanation to the observed discrepancy. In this explanation the TJP mode observed in the c -axis optical spectrum is the main reason. The broad peak that the TJP mode created in the spectrum causes an underestimation of the superfluid density, when we calculate it from the missing area. The SW of the TJP mode in addition to the zero-frequency SW (superconducting carriers condensed to zero-frequency) should be taken into account, therefore, a simple calculation gives a smaller value compare to the true estimation from the imaginary optical conductivity. Hence a difference between the calculations from real and imaginary optical conductivity is observed.

When the TJP mode is suppressed with Zn-substitution, the discrepancy also gradually decreases and finally disappears when the TJP mode is completely suppressed. Similar decrease of difference was also reported for the magneto optical measurement for the same $\text{YBa}_2\text{Cu}_3\text{O}_y$ [109]. In this case, the TJP mode was suppressed by applying magnetic field. Based on these results, at least for the $\text{YBa}_2\text{Cu}_3\text{O}_y$ system, there is no evidence of the kinetic energy contribution in the c -axis spectrum. Another reason why we think this can be a reasonable explanation is that with changing the cut-off frequency, we observed that the ratio changes depending on whether ω -range includes all TJP mode or not. The value of 5000 cm^{-1} is high enough to get all the TJP mode effect. On the other hand, 800 cm^{-1} is low and in some doping levels, we cannot include the high energy part of the TJP mode (in case of splitting). Therefore, the ratios

4. RESULTS AND DISCUSSION

obtained with 800 cm^{-1} cut-off is larger than the case for 5000 cm^{-1} cut-off. This difference due to the cut-off frequency becomes especially significant in the case that the excluded TJP mode is comparable with the overall SW. Since the conductivities at higher doping regions are high (around one order of magnitude) than the lower doping regions, the effect of TJP mode is not pronounced at the high doping level. For $p = 0.11$, all the TJP mode already shifted below 800 cm^{-1} , hence the cut-off frequency does not affect the result. In Fig. 4.35, the result of the cut-off frequency dependence is shown.

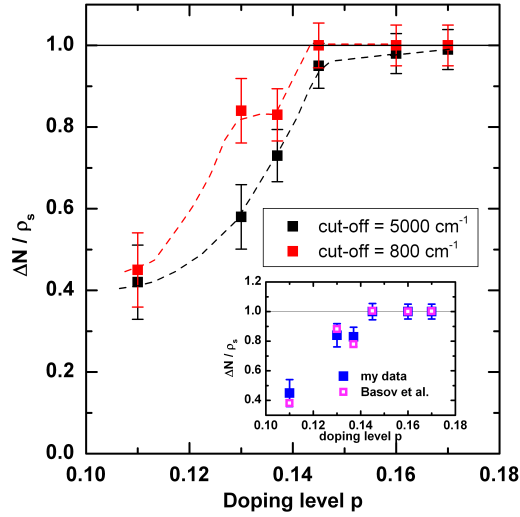


Figure 4.35: Cut-off frequency dependence of $\Delta N / \rho_s$ - With decreasing cut-off frequency, we underestimate the effect of the TJP mode. Inset: Comparison of our results with published data by Basov *et al.* [101]

5

Conclusion

In this study, the charge dynamics of the high temperature cuprate superconductor $\text{YBa}_2(\text{Cu}_{1-x}\text{Zn}_x)_3\text{O}_y$ over the electronic phase diagram have been investigated in a very wide doping range, as well as, for several Zn-contents, both in the normal and the superconducting state. The temperature dependent reflectivity measurements have been performed with Fourier transform infrared spectroscopy over a wide energy range. The optical conductivity spectra have been calculated from the reflectivity by using the Kramers-Krönig transformation.

Detailed spectral weight analysis is performed on the optical conductivity spectra, especially in the pseudogap region. Several issues regarding to the electronic phase diagram were discussed. As a result, we obtained several important conclusions. Firstly, the behavior of the pseudogap in the superconducting state, secondly, the behavior of a precursor of superconductivity, and finally, some remarks related to the kinetic energy driven superconductivity were summarized below.

5.1 Pseudogap in the Superconducting State

Pseudogap state had been discussed by many experimental studies and theoretical works, which can be classified into two basic groups: Pseudogap as a precursor of superconductivity or the pseudogap as a competing order to the superconductivity.

To investigate these points, it is necessary to search the existence of the pseudogap in the superconducting state. Basic idea is that, if the pseudogap is a precursor of superconductivity, the carriers contributing to this state should contribute to the

5. CONCLUSION

superconductivity below T_c . The SW analysis explained in this thesis showed that this is not the case. As a generic behavior to the pseudogap, the SW lost from the low energy optical conductivity with the pseudogap opening is transferred to the high energy region. When this SW is investigated, it has been shown that the this SW never comes back to the $\delta(0)$ below T_c (as an indication of the superconductivity). Moreover, the continuous increase of the high energy SW is observed below T_c in the case that we weaken the superconductivity with Zn-substitution. The behavior of the Zn-doped samples, namely the signature of the pseudogap and superconductivity, indicates that the pseudogap and the superconducting gap are two different states and the pseudogap is not the precursor of the superconductivity. Furthermore, this point has been further supported by the results of our non-superconducting sample ($x = 0.04, p = 0.13$) in the underdoped region. Even though this sample is non-superconducting, the pseudogap was observed, as well, starting at a similar temperature with the other superconducting samples.

All of these results suggest that the insulating ground state (pseudogap) coexists with the superconducting region below T_c . Pseudogap cannot be identified as a precursor of the superconductivity. It should be considered as another order.

5.2 Pseudogap in the Overdoped Region

Another topic discussed in this thesis is the behavior of the pseudogap in the overdoped region. Even though the general behavior of the pseudogap (namely T^* is decreasing with doping level) is widely accepted and has been shown by many experimental probes, the behavior of this state in the overdoped region is rather ambiguous. One approach is that the pseudogap crosses the T_c dome goes to zero at around 19% doping level. Another one is that the pseudogap merges with the superconducting dome in the overdoped region.

Our results on the relation of the pseudogap and the superconducting region suggest that the first scenario is more likely the case, since a merge might be interpreted as a precursor state. We investigate this point by using overdoped samples that are Zn-free and Zn-substituted. In the underdoped region, as mentioned before even for the non-superconducting sample, T^* does not change significantly with Zn-substitution. On the

other hand, T_c is suppressed gradually. In the overdoped region, the Zn-free sample did not show any pseudogap signature, however, when we suppress T_c with Zn-doping, we could observe the pseudogap. Since T^* is robust against the Zn-substitution, the observed T^* should be the same for the Zn-free sample which indicates that T^* for this sample is located below the T_c dome.

According to this observation, T^ does not merge with the superconducting dome in the overdoped region as supported by the competing order scenario. It crosses the T_c dome goes to zero .*

5.3 Precursor Superconducting State

The results discussed in this thesis shows that the pseudogap is not a precursor of superconductivity. On the other hand, the SW analysis also revealed that another state that can be thought as a precursor superconductivity in the pseudogap region of the phase diagram. A precursor state has also been discussed by several other experiments; however, there is no consensus about the doping dependence and the temperature range. In this study we clearly observed the existence of the superfluid density (ω_{ps}^2) at temperatures (T_p) higher than T_c . With decreasing temperature, ω_{ps}^2 gradually increases and at the temperature T'_c near T_c , the slope of the increase suddenly becomes steeper. It seems that the superconducting carriers persist up to much higher temperatures than T_c , although its fraction is very small (less than a few % of the total ω_{ps}^2 at $T = 0$).

It is interesting that the doping dependences of T'_c and T_p are different. T'_c is always 10-20 K above T_c and thus follow the T_c change, whereas T_p increases with decreasing doping levels (p) and reaches much higher temperatures than T'_c . T'_c and T_p are almost merged at the optimum doping $p = 0.16$. On the other hand, with Zn-substitution both temperature scales decrease like T_c .

The existence of the superfluid density, moreover, the Zn-dependence show that the superconducting regions start to evolve at T_p , and the system changes to be a bulk superconductor at T'_c .

5. CONCLUSION

5.4 Kinetic Energy Driven Superconductivity

There are some theories that explain the superconductivity mechanism as the kinetic energy driven superconductivity. Previously, while the c -axis optical conductivity was studied, it was observed that the superfluid density obtained by the missing area method is significantly smaller than that calculated from the imaginary optical conductivity. It has been explained that some of the carriers contributing to the condensation actually come from very high energy region (around visible region), which corresponds to the kinetic energy contribution. However, in many cases, the missing area is underestimated, since it has been calculated within the limited energy region. The calculated condensation energy for the c -axis spectra is smaller than the theoretical expectations. Therefore, in the early days it has been thought that the remaining portion might be observed in the in-plane spectra. It is necessary to point out that this is only observed for the Bi2212 system in the in-plane spectrum, and other systems does not show such kind of high ω contribution.

We have revealed that the discrepancy of the superfluid density does not come from the kinetic energy contribution, but it is due to the mistreatment of the transverse Josephson plasma (TJP) mode. We observed that in the case of suppression of the TJP mode with Zn-substitution, the superfluid density discrepancy disappears. The TJP mode creates a broad absorption peak in the spectrum, which causes the underestimation of the missing area and leads to the discrepancy of ω_{ps}^2 .

Based on these results, we conclude that there is no evidence for the kinetic energy contribution to superconductivity in the c -axis optical spectra. It can be treated as the misinterpretation of the TJP mode.

5.5 Future Work

Similar study should be performed for other cuprate families to generalize the observed behaviors for the cuprate families. However, it seems that the c -axis studies are difficult to perform for other cuprate families, since they have significantly smaller c -axis conductivity. Furthermore, the studies in the heavily underdoped region of the phase diagram also very difficult to perform due to the weak electronic response along the c -axis in this doping regime.

Therefore, the response of the precursor state in the in-plane spectrum should be distinguished and this study should be performed in in-plane spectra. Higher electronic component of in-plane response make the analysis easier in this direction. Moreover, in-plane studies will allow us to examine other cuprates, as well. Furthermore, the lower doping regime will be studied with more accuracy and the interplay with the antiferromagnetic state and the superconductivity will be discussed in more detail.

5. CONCLUSION

References

- [1] H. KAMERLINGH ONNES. *Leiden Comm.*, **120b**, **122b**, **124c**, 1911.
- [2] J. G. BEDNORZ AND K. A. MÜLLER. **Possible high T_c superconductivity in the Ba-La-Cu-O system.** *Zeitschrift für Physik B*, **64**(189), 1986.
- [3] Y. KAMIHARA, T. WATANABE, M. HIRANO, AND H. HOSONO. **Iron-based layered superconductor $\text{La}[\text{O}_{1-x}\text{F}_x]\text{FeAs}$ ($x=0.05-0.12$) with $T_c=26$ K.** *Journal of the American Chemical Society*, **130**:3296, 2008.
- [4] J. BARDEEN, L. N. COOPER, AND J. R. SCHRIEFFER. **Theory of superconductivity.** *Physical Review*, **108**:1175, 1957.
- [5] P. DAI, B. C. CHAKOUMAKOS, G. F. SUN, K. W. WONG, Y. XIN, AND D. F. LU. **Synthesis and neutron powder diffraction study of the superconductor $\text{HgBa}_2\text{Ca}_2\text{Cu}_3\text{O}_{8+\delta}$ by Tl substitution.** *Physica C*, **243**:201, 1995.
- [6] T. KAJITANI, K. HIRAGA, T. SAKURAI, M. HIRABAYASHI, S. HOSOYA, T. FUKUDA, AND K. OHISHI. **X-ray and neutron single-crystal diffraction study on $\text{La}_{1.92}\text{Sr}_{0.08}\text{CuO}_{4-y}$.** *Physica C*, **171**:491, 1990.
- [7] A. P. PAULIKAS J. D. JORGENSEN, B. W. VEAL, L. J. NOWICKI, G. B. CRABTREE, H. CLAUS, AND W. K. KWOK. **Structural properties of oxygen-deficient $\text{YBa}_2\text{Cu}_3\text{O}_{7-\delta}$.** *Physical Review B*, **41**:1863, 1990.
- [8] V. J. EMERY. **Theory of high- T_c superconductivity in oxides.** *Physical Review Letters*, **58**:2794, 1988.
- [9] C. M. VARMA, S. SCHMITT-RINK, AND ELIHU ABRAHAM. **Charge transfer excitations and superconductivity in “ionic” metals.** *Solid State Communications*, **62**:681, 1987.
- [10] F. C. ZHANG AND T. M. RICE. **Effective Hamiltonian for the superconducting Cu oxides.** *Physical Review B*, **37**:3759, 1988.
- [11] P. A. LEE, N. NAGAOSA, AND X.-G. WEN. **Doping a Mott insulator: Physics of high-temperature superconductivity.** *Reviews of Modern Physics*, **78**:17, 2006.
- [12] P. W. ANDERSON, P. A. LEE, M. RANDERIA, T. M. RICE, N. TRIVEDI, AND F. C. ZHANG. **The physics behind high-temperature superconducting cuprates: the ‘plain vanilla’ version of RVB.** *Journal of Physics: Condensed Matter*, **16**:R755, 2004.

REFERENCES

- [13] A. ABANOV, A. V. CHUBUKOV, AND J. SCHMALIAN. **Quantum-critical theory of the spin-fermion model and its application to cuprates: Normal state analysis.** *Advances in Physics*, **52**:119, 2003.
- [14] A. V. CHUBUKOV AND D. K. MORR. **Electronic structure of underdoped cuprates.** *Physics Reports*, **288**:355, 1997.
- [15] S. A. KIVELSON, I. P. BINDLOSS, E. FRADKIN, E. FRADKIN, J. M. TRANQUADA, A. KAPITULNIK, AND C. HOWALD. **How to detect fluctuating stripes in the high-temperature superconductors.** *Reviews of Modern Physics*, **75**:1201, 2003.
- [16] M. TAKIGAWA, A. P. REYES, P. C. HAMMEL, J. D. THOMPSON, R. H. HEFFNER, Z. FISK, AND K. C. OTT. **Cu and O NMR studies of the magnetic properties of $\text{YBa}_2\text{Cu}_3\text{O}_{6.63}$ ($T_c=62$ K).** *Physical Review B*, **43**:247, 1991.
- [17] H. ALLOUL, T. OHNO, AND P. MENDELS. **^{89}Y NMR evidence for a fermi liquid behavior in $\text{YBa}_2\text{Cu}_3\text{O}_{6+x}$.** *Physical Review Letters*, **63**:1700, 1989.
- [18] T. SATO, H. MATSUI, S. NISHINA, T. TAKAHASHI, T. FUJII, T. WATANABE, AND A. MATSUDA. **Low energy excitation and scaling in $\text{Bi}_2\text{Sr}_2\text{Ca}_{n-1}\text{Cu}_n\text{O}_{2n-4}$ ($n = 1-3$): Angle-resolved photoemission spectroscopy.** *Physical Review Letters*, **89**:067005, 2002.
- [19] I. M. VISHIK, W. S. LEE, R.-H. HE, M. HASHIMOTO, Z. HUSSAIN, T. P. DEVEREAUX, AND Z.-X. SHEN. **ARPES studies of cuprate Fermiology: superconductivity, pseudogap and quasiparticle dynamics.** *New Journal of Physics*, **12**:105008, 2010.
- [20] Y. ANDO, S. KOMIYA, K. SEGAWA, S. ONO, AND Y. KURITA. **Electronic phase diagram of high- T_c cuprate superconductors from a mapping of the in-plane resistivity curvature.** *Physical Review Letters*, **93**:267001, 2004.
- [21] S.H. NAQIB, M. BORHAN UDDIN, AND J.R. COLE. **Modeling of the out-of-plane resistivity of cuprate superconductors.** *Physica C*, **471**:1598, 2011.
- [22] Y. WANG, L. LI, AND N. P. ONG. **Nernst effect in high- T_c superconductors.** *Physical Review B*, **73**:024510, 2006.
- [23] T. KONDO, Y. HAMAYA, A. D. PALCZEWSKI, T. TAKEUCHI, J. S. WEN, Z. J. XU, G. GU, J. SCHMALIAN, AND A. KAMINSKI. **Disentangling Cooper-pair formation above the transition temperature from the pseudogap state in the cuprates.** *Nature Physics*, **7**:21, 2010.
- [24] I. MARTIN AND C. PANAGOPOULOS. **Nernst effect and diamagnetic response in a stripe model of superconducting cuprates.** *Europhysics Letters*, **91**:67001, 2010.
- [25] L. B. IOFFE AND A. J. MILLIS. **Big fast vortices in the d -wave resonating valence bond theory of high-temperature superconductivity.** *Physical Review B*, **66**:094513, 2002.
- [26] P. A. LEE. **Orbital currents and cheap vortices in underdoped cuprates.** *Physica C*, **388**:7, 2003.

REFERENCES

- [27] L. S. BILBRO, R. VALDÉS AGUILAR, G. LOGVENOV, O. PELLEG, I. BOŽOVIĆ, AND N. P. ARMITAGE. **Temporal correlations of superconductivity above the transition temperature in $\text{La}_{2-x}\text{Sr}_x\text{CuO}_4$ probed by terahertz spectroscopy.** *Nature Physics*, **7**:298, 2011.
- [28] A. LARKIN AND A. VARLAMOV. *Theory of Fluctuations in Superconductors*. Oxford Science Publications, 2005.
- [29] L. LI, Y. WANG, S. KOMIYA, S. ONO, Y. ANDO, G. D. GU, AND N. P. ONG. **Diamagnetism and Cooper pairing above T_c in cuprates.** *Physical Review B*, **81**:054510, 2010.
- [30] M. S. GRBIĆ, M. POŽEK, D. PAAR, V. HINKOV, M. RAICHLE, D. HAUG, B. KEIMER, N. BARIŠIĆ, AND A. DULČIĆ. **Temperature range of superconducting fluctuations above T_c in $\text{YBa}_2\text{Cu}_3\text{O}_{7-\delta}$ single crystals.** *Physical Review B*, **83**:144508, 2011.
- [31] K. SEGAWA AND YOICHI ANDO. **Transport properties of untwinned $\text{YBa}_2\text{Cu}_3\text{O}_y$ single crystals and the origin of the 60-K plateau.** *Journal of Low Temperature Physics*, **131**:821, 2003.
- [32] S. TAJIMA, J. SCHÜTZMANN, S. MIYAMOTO, I. TERASAKI, Y. SATO, AND R. HAUFF. **Optical study of c -axis charge dynamics in $\text{YBa}_2\text{Cu}_3\text{O}_y$: Carrier self-confinement in the normal and the superconducting states.** *Physical Review B*, **55**:6051, 1997.
- [33] S. UCHIDA, K. TAMASAKU, AND S. TAJIMA. **c -axis optical spectra and charge dynamics in $\text{La}_{2-x}\text{Sr}_x\text{CuO}_4$.** *Physical Review B*, **53**:14558, 1996.
- [34] C. C. HOMES, T. TIMUSK, D. A. BONN, R. LIANG, AND W. N. HARDY. **Optical properties along the c -axis of $\text{YBa}_2\text{Cu}_3\text{O}_{6+x}$, for $x = 0.50$ to 0.95 Evolution of the pseudogap.** *Physica C*, **254**:265, 1995.
- [35] A.V. BORIS, D. MUNZAR, N. N. KOVALEVA, B. LIANG, C. T. LIN, A. DUBROKA, A.V. PIMENOV, T. HOLDEN, B. KEIMER, Y. L. MATHIS, AND C. BERNHARD. **Josephson plasma resonance and phonon anomalies in trilayer $\text{Bi}_2\text{Sr}_2\text{Ca}_2\text{Cu}_3\text{O}_{10}$.** *Physical Review Letters*, **89**:277001, 2002.
- [36] T. TIMUSK AND B. STATT. **The pseudogap in high-temperature superconductors: an experimental survey.** *Reports on Progress in Physics*, **62**:61, 1996.
- [37] L. B. IOFFE AND A. J. MILLIS. **Superconductivity and the c -axis spectral weight of high- T_c superconductors.** *Science*, **285**:1241, 1999.
- [38] S. CHAKRAVARTY, A. SUDBO, P. W. ANDERSON, AND S. STRONG. **Interlayer tunneling and gap anisotropy in high-temperature superconductors.** *Science*, **261**:337, 1993.
- [39] A. V. PUCHKOV, D. N. BASOV, AND T. TIMUSK. **The pseudogap state in high- T_c superconductors: an infrared study.** *Journal of Physics: Condensed Matter*, **8**:10049, 1996.
- [40] C. C. HOMES, T. TIMUSK, R. LIANG, D. A. BONN, AND W. N. HARDY. **Optical conductivity of c -axis oriented $\text{YBa}_2\text{Cu}_3\text{O}_{6.70}$: Evidence for a pseudogap.** *Physical Review Letters*, **71**:1645, 1993.

REFERENCES

- [41] A. DUBROKA, L. YU, D. MUNZAR, K. W. KIM, M. ROSSLE, V. K. MALIK, C. T. LIN, B. KEIMER, TH. WOLF, AND C. BERNHARD. **Pseudogap and precursor superconductivity Pseudogap and precursor superconductivity in underdoped cuprate high temperature superconductors: A far-infrared ellipsometry study.** *Eur. Phys. J. Special Topics*, **188**:73, 2010.
- [42] S. V. DORDEVIC, S. KOMIYA, Y. ANDO, Y. J. WANG, AND D. N. BASOV. **Josephson vortex state across the phase diagram of $\text{La}_{2-x}\text{Sr}_x\text{CuO}_4$: A magneto-optics study.** *Physical Review B*, **71**:054503, 2005.
- [43] D. N. BASOV, T. TIMUSK, B. DABROWSKI, AND J. D. JORGENSEN. **c -axis response of $\text{YBa}_2\text{Cu}_4\text{O}_8$: A pseudogap and possibility of Josephson coupling of CuO_2 planes.** *Physical Review B*, **50**:3511, 1994.
- [44] T. SHIBAUCHI, H. KITANO, K. UCHINOKURA, A. MAEDA, T. KIMURA, AND K. KISHIO. **Anisotropic penetration depth in $\text{La}_{2-x}\text{Sr}_x\text{CuO}_4$.** *Physical Review Letters*, **72**:2263, 1994.
- [45] P. J. HIRSCHFELD, S. M. QUINLAN, AND D. J. SCALAPINO. **c -axis infrared conductivity of a $d_{x^2-y^2}$ -wave superconductor with impurity and spin-fluctuation scattering.** *Physical Review B*, **55**:12742, 1997.
- [46] S. CHAKRAVARTY, H.-Y. KEE, AND E. ABRAHAMS. **Frustrated kinetic energy, the optical sum rule, and the mechanism of superconductivity.** *Physical Review Letters*, **82**:2366, 1999.
- [47] W. KIM AND J. P. CARBOTTE. **Conductivity sum rule: Comparison of coherent and incoherent c -axis coupling.** *Physical Review B*, **61**:11886(R), 2000.
- [48] Y. OHASHI. **Theory of Basov correlation between penetration depth and conductivity along the c -axis in high- T_c cuprate superconductors.** *Journal of the Physical Society of Japan*, **69**:659, 2000.
- [49] D. N. BASOV AND T. TIMUSK. **Electrodynamics of high- T_c superconductors.** *Reviews of Modern Physics*, **77**:721, 2005.
- [50] D. VAN DER MAREL AND A. A. TSVETKOV. **Transverse optical plasmons in layered superconductors.** *Czech. Journal of Physics*, **46**:3165, 1996.
- [51] H. SHIBATA AND T. YAMADA. **Double Josephson plasma resonance in T^* phase $\text{SmLa}_{1-x}\text{Sr}_x\text{CuO}_{4-\delta}$.** *Physical Review Letters*, **81**(3519), 1998.
- [52] C. BERNHARD, D. MUNZAR, A. GOLNIK, C. T. LIN, A. WITTLIN, J. HUMLÍČEK, AND M. CARDONA. **Anomaly of oxygen bond-bending mode at 320 cm^{-1} and additional absorption peak in the c -axis infrared conductivity of underdoped $\text{YBa}_2\text{Cu}_3\text{O}_{7-\delta}$ single crystals revisited with ellipsometric measurements.** *Physical Review B*, **61**:618, 2000.
- [53] M. GRÜNINGER, D. VAN DER MAREL, A. A. TSVETKOV, AND A. ERB. **Observation of out-of-phase bilayer plasmons in $\text{YBa}_2\text{Cu}_3\text{O}_{7-\delta}$.** *Physical Review Letters*, **84**(1575), 2000.

- [54] D. MUNZAR, T. HOLDEN, AND C. BERNHARD. **Approximate tight-binding sum rule for the superconductivity-related change of c -axis kinetic energy in multilayer cuprate superconductors.** *Physical Review B*, **67**:020501(R), 2003.
- [55] A. DUBROKA AND D. MUNZAR. **Phonon anomalies in trilayer high- T_c cuprate superconductors.** *Physica C*, **405**:133, 2004.
- [56] Y. FUKUZUMI, K. MIZUHASHI, AND S. UCHIDA. **Zn-doping effect on the c -axis charge dynamics of underdoped high- T_c cuprates.** *Physical Review B*, **61**:627, 2000.
- [57] R. HAUFF, S. TAJIMA, W.-J. JANG, AND A. I. RYKOV. **Optical study on phonon anomalies and spin gap in $\text{YBa}_2(\text{Cu}_{1-x}\text{Zn}_x)_3\text{O}_{6.6}$.** *Physical Review Letters*, **77**:4620, 1996.
- [58] J. SCHÜTZMANN, S. TAJIMA, S. MIYAMOTO, Y. SATO, AND I. TERASAKI. **Origin of low-temperature residual absorption in $\text{YBa}_2\text{Cu}_3\text{O}_y$.** *Solid State Communications*, **94**:293, 1995.
- [59] C. BERNHARD, R. HENN, A. WITTLIN, M. KLÄSER, TH. WOLF, G. MÜLLER-VOGT, C. T. LIN, AND M. CARDONA. **Electronic c -axis response of $\text{Y}_{1-x}\text{Ca}_x\text{Ba}_2\text{Cu}_3\text{O}_{7-\delta}$ crystals studied by far-infrared ellipsometry.** *Physical Review Letters*, **80**:1762, 1998.
- [60] S. TAJIMA, Y. FUDAMOTO, T. KAKESHITA, B. GORSHUNOV, V. ŽELEZNÝ, K. M. KOJIMA, M. DRESSEL, AND S. UCHIDA. **In-plane optical conductivity of $\text{La}_{2-x}\text{Sr}_x\text{CuO}_4$: Reduced superconducting condensate and residual Drude-like response.** *Physical Review B*, **71**:094508, 2005.
- [61] Y. C. MA AND N. L. WANG. **Infrared scattering rate of overdoped $\text{Tl}_2\text{Ba}_2\text{CuO}_{6+\delta}$.** *Physical Review B*, **73**:144503, 2006.
- [62] E. UYKUR, K. TANAKA, T. MASUI, S. MIYASAKA, AND S. TAJIMA. **In-plane optical spectra of $\text{Y}_{1-x}\text{Ca}_x\text{Ba}_2\text{Cu}_3\text{O}_{7-\delta}$: Overdoping and disorder effects on residual conductivity.** *Physical Review B*, **84**:184527, 2011.
- [63] Y. YAMADA AND Y. SHIOHARA. **Continuous crystal growth of $\text{YBa}_2\text{Cu}_3\text{O}_{7-x}$ the modified top-seeded crystal pulling method.** *Physica C*, **217**:182, 1993.
- [64] J. D. JORGENSEN, M. A. BENO, D. G. HINKS, L. SODERHOLM, K. J. VOLIN, R. L. HITTRMAN, J. D. GRACE, I. K. SCHULLER, C. U. SEGRE, K. ZHANG, AND M. S. KLEEFISCH. **Oxygen ordering and the orthorhombic-to-tetragonal phase transition in $\text{YBa}_2\text{Cu}_3\text{O}_{7-x}$.** *Physical Review B*, **36**:3608, 1987.
- [65] R. LIANG, D. A. BONN, AND W. N. HARDY. **Evaluation of CuO_2 plane hole doping in $\text{YBa}_2\text{Cu}_3\text{O}_{6+x}$ single crystals.** *Physical Review B*, **73**:180505(R), 2006.
- [66] T. MASUI, Y. TAKANO, K. YOSHIDA, K. KAJITA, AND S. TAJIMA. **The effect of Zn-substitution and carrier doping on vortex pinning in $\text{YBa}_2\text{Cu}_3\text{O}_{7-\delta}$ single crystals.** *Physica C*, **412**:414, 2004.
- [67] MARTIN DRESSEL AND GEORGE GRÜNER. *Electrodynamics of Solids*. Cambridge University Press, 2002.

REFERENCES

- [68] R. DE L. KRONIG. **On the Theory of Dispersion of X-Rays.** *Journal of the Optical Society of America and Review of Scientific Instruments*, **12**:547, 1926.
- [69] A. B. KUZMENKO. **Kramers–Kronig constrained variational analysis of optical spectra.** *Review of Scientific Instruments*, **76**:083108, 2005.
- [70] T. MASUI, Y. URAIKE, K. NAGASAO, AND S. TAJIMA. **The change of anisotropy by Zn or Ca substitution in YBCO single crystals.** *Journal of Physics: Conference Series*, **150**:052152, 2009.
- [71] J. SCHÜTZMANN, S. TAJIMA, S. MIYAMOTO, Y. SATO, AND R. HAUFF. **Doping and temperature dependence of c -axis optical phonons in $\text{YBa}_2\text{Cu}_3\text{O}_y$ single crystals.** *Physical Review B*, **52**:13665, 1995.
- [72] A. DUBROKA, M. RÖSSLE, K. W. KIM, V. K. MALIK, D. MUNZAR, D. N. BASOV, A. A. SCHAFGANS, S. J. MOON, C. T. LIN, D. HAUG, V. HINKOV, B. KEIMER, TH. WOLF, J. G. STOREY, J. L. TALLON, , AND C. BERNHARD. **Evidence of a precursor superconducting phase at temperatures as high as 180 K in $\text{RBa}_2\text{Cu}_3\text{O}_{7-\delta}$ ($\text{R}=\text{Y,Gd,Eu}$) superconducting crystals from infrared spectroscopy.** *Physical Review Letters*, **106**:047006, 2011.
- [73] M. FERRERO, O. PARCOLLET, A. GEORGES, G. KOTLIAR, AND D. N. BASOV. **Interplane charge dynamics in a valence-bond dynamical mean-field theory of cuprate superconductors.** *Physical Review B*, **82**:054502, 2010.
- [74] N. LIN, E. GULL, AND A. J. MILLIS. **Physics of the pseudogap in eight-site cluster dynamical mean-field theory: Photoemission, Raman scattering, and in-plane and c -axis conductivity.** *Physical Review B*, **82**:045104, 2010.
- [75] O. K. ANDERSEN, A. I. LIECHTENSTEIN, O. JEPSEN, AND F. PAULSEN. **LDA energy bands, low energy hamiltonians, t , t' , $t_{\perp}(\mathbf{k})$, and \mathbf{J}_{\perp} .** *Journal of Physics and Chemistry of Solids*, **56**:1573, 1995.
- [76] H. ALLOUL. **From Friedel oscillations and Kondo effect to the pseudogap in cuprates.** *Journal of Superconductivity and Novel Magnetism*, **25**:585, 2012.
- [77] R. DAOU, J. CHANG, D. LEBOEUF, O. CYR-CHOINIÉRE, F. LALIBERTÉ, N. DOIRON-LEYRAUD, B. J. RAMSHAW, R. LIANG, D. A. BONN, W. N. HARDY, AND L. TAILLEFER. **Broken rotational symmetry in the pseudogap phase of a high- T_c superconductor.** *Nature*, page 519, 463.
- [78] N. MIYAKAWA, P. GUPTASARMA, J. F. ZASADZINSKI, D. G. HINKS, AND K. E. GRAY. **Strong dependence of the superconducting gap on oxygen doping from tunneling measurements on $\text{Bi}_2\text{Sr}_2\text{CaCu}_2\text{O}_{8-\delta}$.** *Physical Review Letters*, page 157, 1998.
- [79] J. L. TALLON, J. W. LORAM, G. V. M. WILLIAMS, J. R. COOPER, I. R. FISHER, J. D. JOHNSON, M. P. STAINES, AND C. BERNHARD. **Critical doping in overdoped high- T_c superconductors: A quantum critical point?** *Physicica Status Solidi (b)*, **215**:531, 1999.

-
- [80] G. GRÜNER. **The dynamics of charge-density waves.** *Reviews of Modern Physics*, **60**:1129, 1988.
- [81] G. GRÜNER. **The dynamics of spin-density waves.** *Reviews of Modern Physics*, **66**:1, 1994.
- [82] S. V. DORDEVIC, E. J. SINGLEY, D. N. BASOV, S. KOMIYA, Y. ANDO, E. BUCHER, C. C. HOMES, AND M. STRONGIN. **Global trends in the interplane penetration depth of layered superconductors.** *Physical Review B*, **65**:134511, 2002.
- [83] D. NAKAMURA, Y. IMAI, A. MAEDA, AND I. TSUKADA. **Superconducting fluctuation investigated by THz conductivity of $\text{La}_{2-x}\text{Sr}_x\text{CuO}_4$ thin films.** *Journal of the Physical Society of Japan*, **81**:044709, 2012.
- [84] T. OHASHI, H. KITANO, I. TSUKADA, AND A. MAEDA. **Critical charge dynamics of superconducting $\text{La}_{2x}\text{Sr}_x\text{CuO}_4$ thin films probed by complex microwave spectroscopy: Anomalous changes of the universality class by hole doping.** *Physical Review B*, **79**:184507, 2009.
- [85] N. P. ONG, Y. WANG, S. ONO, YOICHI ANDO, AND S. UCHIDA. **Vorticity and the Nernst effect in cuprate superconductors.** *Annalen der Physik (Leipzig)*, **13**:9, 2003.
- [86] V. PASLER, P. SCHWEISS, C. MEINGAST, B. OBST, H. WÜHL, A. I. RYKOV, AND S. TAJIMA. **3D-XY critical fluctuations of the thermal expansivity in detwinned $\text{YBa}_2\text{Cu}_3\text{O}_{7-\delta}$ single crystals near optimal doping.** *Physical Review Letters*, **81**:1094, 1998.
- [87] D. LEBOEUF, N. DOIRON-LEYRAUD, B. VIGNOLLE, M. SUTHERLAND, B. J. RAMSHAW, J. LEV-ALLOIS, R. DAOU, F. LALIBERTÉ, O. CYR-CHOINIÈRE, J. CHANG, Y. J. JO, L. BALICAS, R. LIANG, D. A. BONN, W. N. HARDY, C. PROUST, AND L. TAILLEFER. **Lifshitz critical point in the cuprate superconductor $\text{YBa}_2\text{Cu}_3\text{O}_y$ from high-field Hall effect measurements.** *Physical Review B*, **83**:054506, 2011.
- [88] P. DAI, H. A. MOOK, S. M. HAYDEN, G. AEPPLI, T. G. PERRING, R. D. HUNT, AND F. DOĞAN. **The magnetic excitation spectrum and thermodynamics of high- T_c superconductors.** *Science*, **284**:1344, 1999.
- [89] G. Q. ZHENG, T. ODAGUCHI, Y. KITAOKA, K. ASAYAMA, Y. KODAMA, K. MIZUHASHI, AND S. UCHIDA. **Zn and Ni doping effects on T_c and spin gap behavior in $\text{YBa}_2\text{Cu}_4\text{O}_8$ and $\text{YBa}_2\text{Cu}_3\text{O}_{6.6}$.** *Physica C*, **263**:367, 1996.
- [90] V. Z. KRESIN, Y. N. OVCHINNIKOV, AND S. A. WOLF. **Inhomogeneous superconductivity and the “pseudogap” state of novel superconductors.** *Physics Reports*, **431**:231, 2006.
- [91] V. J. EMERY AND S. A. KIVELSON. **Importance of phase fluctuations in superconductors with small superfluid density.** *Nature*, **374**:434, 1995.
- [92] V. J. EMERY, S. A. KIVELSON, AND O. ZACHAR. **Spin-gap proximity effect mechanism of high-temperature superconductivity.** *Physical Review B*, **56**:6120, 1997.
- [93] A. LARKIN AND A. VARLAMOV. *Theory of fluctuations in superconductors.* Oxford University Press, 2009.

REFERENCES

- [94] J. LEE, K. FUJITA, A. R. SCHMIDT, CHUNG KOO KIM, H. EISAKI, S. UCHIDA, AND J. C. DAVIS. **Spectroscopic fingerprint of phase-incoherent superconductivity in the underdoped $\text{Bi}_2\text{Sr}_2\text{CaCu}_2\text{O}_{8+\delta}$.** *Science*, **325**:1099, 2009.
- [95] V. L. BEREZINSKIĬ. **Destruction of long-range order in one-dimensional and two-dimensional systems a continuous symmetry group I. classical systems.** *Soviet Physics JETP*, **32**:493, 1971.
- [96] J. M. KOSTERLITZ AND D. J. THOULESS. **Ordering, metastability and phase transitions in two-dimensional systems.** *Journal of Physics C: Solid State Physics*, **6**:1181, 1973.
- [97] Y. ANDO AND K. SEGAWA. **Magnetoresistance of untwinned $\text{YBa}_2\text{Cu}_3\text{O}_y$ single crystals in a wide range of doping: Anomalous hole-doping dependence of the coherence length.** *Physical Review Letters*, **88**:167005, 2002.
- [98] K. K. GOMES, A. N. PASUPATHY, A. PUSHP, S. ONO, Y. ANDO, AND A. YAZDANI. **Visualizing pair formation on the atomic scale in the high- T_c superconductor $\text{Bi}_2\text{Sr}_2\text{CaCu}_2\text{O}_{8-\delta}$.** *Nature Letters*, **447**:569, 2007.
- [99] G. GHIRINGHELLI, M. LE TACON, M. MINOLA, S. BLANCO-CANOSA, C. MAZZOLI, N. B. BROOKES, G. M. DE LUCA, A. FRANO, D. G. HAWTHORN, F. HE, T. LOEW, M. MORETTI SALA, D. C. PEETS, M. SALLUZZO, E. SCHIERLE, R. SUTARTO, G. A. SAWATZKY, E. WESCHKE, B. KEIMER, AND L. BRAICOVICH. **Long-range incommensurate charge fluctuations in $(\text{Y,Nd})\text{Ba}_2\text{Cu}_3\text{O}_{6+x}$.** *Science*, **337**:821, 2012.
- [100] J. CHANG, E. BLACKBURN, A. T. HOLMES, N. B. CHRISTENSEN, J. LARSEN, J. MESOT, R. LIANG, D. A. BONN, W. N. HARDY, A. WATENPHUL, M. V. ZIMMERMANN, E. M. FORGAN, AND S. M. HAYDEN. **Direct observation of competition between superconductivity and charge density wave order in $\text{YBa}_2\text{Cu}_3\text{O}_{6.67}$.** *Nature Physics*, page 871, 2012.
- [101] D. N. BASOV, C. C. HOMES, E. J. SINGLEY, M. STRONGIN, T. TIMUSK, G. BLUMBERG, AND D. VAN DER MAREL. **Unconventional energetics of the pseudogap state and superconducting state in high- T_c cuprates.** *Physical Review B*, **63**:134514, 2001.
- [102] J. E. HIRSCH. **Apparent violation of the conductivity sum rule in certain superconductors.** *Physica C*, **199**:305, 1992.
- [103] H. L. DEWING AND E. K. H. SALJE. **The effect of the superconducting phase transition on the near-infrared absorption of $\text{YBa}_2\text{Cu}_3\text{O}_{7-\delta}$.** *Superconductor Science and Technology*, **5**:50, 1991.
- [104] P. W. ANDERSON. **Interlayer tunneling mechanism for high- T_c superconductivity: Comparison with c -axis infrared experiments.** *Science*, **268**:1154, 1995.
- [105] D. VAN DER MAREL, A. TSVETKOV, M. GRUENINGER, D. DULIC, AND H. J. A. MOLEGRAAF. **c -axis optical properties of high T_c cuprates.** *Physica C*, **341**:1531, 2000.
- [106] J. HWANG, T. TIMUSK, AND G. D. GU. **Doping dependent optical properties of $\text{Bi}_2\text{Sr}_2\text{CaCu}_2\text{O}_{8+d}$.** *Journal of Physics: Condensed Matter*, **19**:125208, 2007.

REFERENCES

- [107] C. GIANNETTI, F. CILENTO, S. DAL CONTE, G. COSLOVICH, G. FERRINI, H. MOLEGRAAF, M. RAICHLE, R. LIANG, H. EISAKI, M. GREVEN, A. DAMASCELLI, D. VAN DER MAREL, AND F. PARMIGIANI. **Revealing the high-energy electronic excitations underlying the onset of high-temperature superconductivity in cuprates.** *Nature Communications*, **2**:353, 2011.
- [108] C. C. HOMES, S. V. DORDEVIC, D. A. BONN, R. LIANG, AND W. N. HARDY. **Sum rules and energy scales in the high-temperature superconductor $\text{YBa}_2\text{Cu}_3\text{O}_{6+x}$.** *Physical Review B*, **69**:024514, 2004.
- [109] A. D. LAFORGE, W. J. PADILLA, K. S. BURCH, Z. Q. LI, A. A. SCHAFGANS, K. SEGAWA, Y. ANDO, AND D. N. BASOV. **Magnetic field induced modification of superfluid density and interplane spectral weight in $\text{YBa}_2\text{Cu}_3\text{O}_y$.** *Physical Review B*, **79**:104516, 2009.

REFERENCES

List of Publication

- [1] **E. UYKUR, K. TANAKA, T. MASUI, S. MIYASAKA, and S. TAJIMA. Persistence of superconducting condensate far above T_c in high temperature cuprate superconductors: Optical study of Zn- and carrier-doping dependences.** *Submitted to Physical Review Letters, 2013.*
- [2] **E. UYKUR, K. TANAKA, T. MASUI, S. MIYASAKA, and S. TAJIMA. Coexistence of the pseudogap and the superconducting gap revealed by the c -Axis optical study of $\text{YBa}_2(\text{Cu}_{1-x}\text{Zn}_x)_3\text{O}_{7-\delta}$.** *Journal of Physical Society of Japan, 83: 033701, (2013).*
- [3] **E. UYKUR, K. TANAKA, T. MASUI, S. MIYASAKA, and S. TAJIMA. Precursor superconductivity and superconducting fluctuation regime revealed by the c -axis optical spectra of $\text{YBa}_2(\text{Cu}_{1-x}\text{Zn}_x)_3\text{O}_y$.** *Physics Procedia, 45: 45, (2013).*
- [4] **E. UYKUR, K. TANAKA, T. MASUI, S. MIYASAKA, and S. TAJIMA. Pseudogap study using c -axis optical Spectra of underdoped $\text{YBa}_2\text{Cu}_3\text{O}_{7-\delta}$.** *Journal of Physical Society of Japan, 81: SB035, (2012).*
- [5] **E. UYKUR, K. TANAKA, T. MASUI, S. MIYASAKA, and S. TAJIMA. In-plane optical spectra of $\text{Y}_{1-x}\text{Ca}_x\text{Ba}_2\text{Cu}_3\text{O}_{7-\delta}$: Overdoping and disorder effects on residual conductivity.** *Physical Review B, 84: 184527, (2011).*
- [6] **E. UYKUR, K. TANAKA, T. MASUI, S. MIYASAKA, and S. TAJIMA. Intrinsic gapless superconductivity in overdoped $(\text{Y,Ca})\text{Ba}_2\text{Cu}_3\text{O}_y$: Study of in-plane optical spectra.** *Physica C, 471: 701, (2011).*

REFERENCES

List of Conferences

- [1] **E. UYKUR**, K. TANAKA, T. MASUI, S. MIYASAKA, and S. TAJIMA.
“Pseudogap behavior in the overdoped region of the cuprate superconductor $\text{YBa}_2(\text{Cu,Zn})_3\text{O}_y$ revealed by the $E//c$ -axis optical study.”, 26aKQ-7, Oral Presentation
JPS, September 2013, Tokushima University, Japan
- [2] **E. UYKUR**, K. TANAKA, T. MASUI, S. MIYASAKA, and S. TAJIMA.
“Evidence of the existence of superconducting carriers above T_c : c -axis optical study of $\text{YBa}_2(\text{Cu}_{1-x}\text{Zn}_x)_3\text{O}_y$.”, 27pXJ-8, Oral Presentation
JPS, March 2013, Hiroshima University, Japan
- [3] **E. UYKUR**, K. TANAKA, T. MASUI, S. MIYASAKA, and S. TAJIMA.
“Precursor superconductivity and superconducting fluctuation regime revealed by the c -axis optical spectra of $\text{YBa}_2(\text{Cu}_{1-x}\text{Zn}_x)_3\text{O}_y$.”, PC-29, Oral Presentation
International Symposium on Superconductivity, December 2012, Tokyo, Japan
- [4] **E. UYKUR**, K. TANAKA, T. MASUI, S. MIYASAKA, and S. TAJIMA.
“Coexistence of the pseudogap and the superconducting gap below T_c revealed by the c -axis optical study of $\text{YBa}_2(\text{Cu,Zn})_3\text{O}_y$.”, 21aGB-1, Oral Presentation
JPS, September 2012, Yokohama University, Japan
- [5] **E. UYKUR**, K. TANAKA, T. MASUI, S. MIYASAKA, and S. TAJIMA.
“Optical Study of the Pseudogap State in $\text{YBa}_2(\text{Cu,Zn})_3\text{O}_y$.”, Poster Presentation
Low Energy Electrodynamics in Solids, July 2012, Napa, USA

REFERENCES

- [6] **E. UYKUR**, K. TANAKA, T. MASUI, S. MIYASAKA, and S. TAJIMA.
“Pseudogap studied by optical conductivity spectra of Zn-substituted $\text{YBa}_2\text{Cu}_3\text{O}_y$.”,
Oral Presentation
APS, March 2012, Boston, USA
- [7] **E. UYKUR**, K. TANAKA, T. MASUI, S. MIYASAKA, and S. TAJIMA.
“Pseudogap study using c -axis optical spectra of underdoped $\text{YBa}_2\text{Cu}_3\text{O}_y$.”, 24P-39,
Poster Presentation
International Workshop on Heavy Fermions, November 2011, Osaka university, JAPAN
- [8] **E. UYKUR**, K. TANAKA, T. MASUI, S. MIYASAKA, and S. TAJIMA.
“Intrinsic gapless superconductivity in overdoped $(\text{Y,Ca})\text{Ba}_2\text{Cu}_3\text{O}_y$: Study of in-plane optical spectra.”, PC-18, Oral Presentation
International Symposium on Superconductivity, November 2010, Tsukuba, Japan
- [9] **E. UYKUR**, K. TANAKA, T. MASUI, S. MIYASAKA, and S. TAJIMA.
“Residual conductivity in heavily overdoped $(\text{Y,Ca})\text{Ba}_2\text{Cu}_3\text{O}_y$.”, PS II-82, Poster Presentation
International Conference on Core Research and Engineering Science of Advanced Materials, May 2010, Osaka University, Japan